Solidification Theory and Optimization of Chromium Carbide Overlays

by

Nairn Barnes

A thesis submitted in partial fulfillment of the requirements for the degree of

Doctor of Philosophy

in

Materials Engineering

Department of Chemical and Materials Engineering
University of Alberta

Abstract

A growth model for the primary M_7C_3 carbides and an investigation of microstructural features in chromium carbide weld overlays are presented. The overall goal of this work is to increase the level of understanding concerning the development of microstructure, enabling a scientific method of predicting carbide morphology, microstructural features, and overlay properties. Existing knowledge of how various features in chromium carbide overlays stems from research developed concerning white and grey cast irons. The knowledge from cast irons cannot be applied to overlays in a meaningful way due to the rapid cooling associated with welding. Industrially, chromium carbide overlays are not currently adaptable for different wear environments and often alloying is used to alter carbide morphology to improve wear life, which carries a large cost. This work will increase the level of understanding surrounding chromium carbide weld overlays, enabling tailored microstructure based on a deeper level of understanding.

Several microstructural features of chromium carbide weld overlays have been investigated. Previous work is inconsistent in identifying the morphology of the primary M_7C_3 carbides and certain studies had identified two distinct microstructures for the carbides: blades and rods. A 3D microstructural reconstruction completed showed that the apparently distinct morphologies are in fact hexagonal prismatic carbide rods that appear different based on varying sectioning planes. Large anomalous features in the microstructure of chromium carbide overlays were investigated for the first time. Through microhardness testing, Auger electron spectroscopy, electron backscatter diffraction, and energy dispersive x-ray spectroscopy the features were identified as unmelted powder granules that survived the thermal cycle. Lower heat inputs were found to result in higher volume fractions of the unmelted powder granules. The powder granules were shown to be a distinct composition of the same orthorhombic M_7C_3 phase as the primary

carbides. These powder granules serve as the main source of chromium and carbon necessary for primary carbide solidification and although they have a high hardness, large volume fraction of these unmelted granules will deplete the overlay of chromium and carbon and lower the volume fraction of primary carbides significantly.

The diffusion-controlled longitudinal growth of the primary M_7C_3 needles was quantified by direct observation for the first time and a growth model considering the carbide tip as a mass point sink was generated. The developed model predicts an rapid initial transient period followed by steady state growth. The transient portion of growth is assumed to occur below the surface of the melt. The developed model was found to match closely to in-situ observations performed on a high-temperature confocal scanning laser microscope. Deviation from the proposed growth model coincides with the observation of soft impingement from other carbides growing within the melt. The carbides locally deplete the solute ahead of the advancing interface causing an abrupt arrest in growth. The transverse growth of the carbides was found to be slow (two orders of magnitude lower than the longitudinal growth) suggesting interface controlled growth and negligible mass flux affecting the local solute concentration. The longitudinal growth was found to be highly dependant on the carbide radius. A study was performed using a thermal-control substrate to determine the effect of cooling rate on carbide size and showed that carbide size decreases with increased cooling rates. Combining the knowledge of the effect of cooling rate with the growth model enables understanding and prediction of carbide morphology. Additionally, the growth model should be applicable to other carbides with similar features.

The results of this work serve to bring a deeper understanding to chromium carbide overlays. In particular, the development and affirmation of a growth model describing the diffusion-controlled growth of faceted primary carbide needles enables a greater control over the final microstructure and properties of the overlay.

Preface

The material presented in this thesis comprises the author's research project under supervision of Dr. Patricio Mendez. This work has been funded by Natural Sciences and Engineering Research Council (NSERC) of Canada (CRD Grant ID CRDPJ/470231-14) in partnership with industrial sponsor Wilkinson Steel and Metals, a division of Samuel, Son & Co. Funding was also received from the AWS Foundation (UA2203790).

Chapter 1, the introduction of this work, is based on two sources written by the author of this thesis. The first is a section of the review paper published as Mendez, P.F., Barnes, N., Bell, K., Borle, S., Gajapathi, S., Guest, S.D., Izadi, H., Kamyabi, A., Wood, G., 2013. "Weld Processes for Wear Resistant Overlays", *Journal of Manufacturing Processes*. The section on chromium-carbide overlays was co-written by Nairn Barnes and Steven Borle. Nairn Barnes was responsible for creating the section on PTAW. The second is a special issue article requested by *Science and Technology of Welding and Joining* to provide a comprehensive review of welding in the heavy automotive industry and was published as Barnes, N., Joseph, T., Mendez, P.F., 2015, "Issues associated with welding and surfacing of large mobile mining equipment for use in oil sands applications" *Science and Technology of Welding and Joining*. Nairn Barnes was responsible for gathering information from various sources, compiling all data, and composition of the paper. Dr. Tim Joseph served as a technical consultant on the paper. Dr. Patricio Mendez was the supervisory author in both cases.

Chapter 2 of this work is published as Barnes, N., Andreiuk, J., Borle, S., Dewar, M., Mendez, P.F., 2014 "3D Microstructure Reconstruction of Chrome Carbide Weld Overlays", *Science and Technology of Welding and Joining*. Nairn Barnes was responsible for conduction of analysis and composition of the paper. John Andreiuk and Steven Borle helped prepare samples and take measurements. Matthew Dewar was responsible

for coding the image analysis program to extract the carbides from the original images. Dr. Patricio Mendez was the supervisory author.

Chapter 3 of this work is published as Barnes, N., Borle, S., Mendez, P.F., 2017 "Large Anomalous Features in the Microstructure of Chromium Carbide Weld Overlays", *Science and Technology of Welding and Joining*. Nairn Barnes was responsible for preparation of microscopy samples, conduction of analysis, and composition of the paper. Steven Borle's role was to generate relevant samples as well as performing hardness measurements. He is a co-author of the paper for his contributions. Dr. Patricio Mendez was the supervisory author.

Chapter 4 of this work is submitted for publication as Barnes, N., Clark, S., Seetharaman, S., Mendez, P.F., 2017 "Growth Mechanism of Chromium Carbide Needles during Solidification", *Acta Materiala*. Nairn Barnes was responsible for preparation of samples, conduction of analysis, and composition of the paper. Samuel Clark's role was to perform the in-situ visualization experiments at the University of Warwick, England, under the supervision of his professor Dr. Sridhar Seetharaman. Dr. Seetharaman, from Colorado School of Mines, also provided advice throughout the writing process and both are listed as co-authors for their contributions. Dr. Patricio Mendez was the supervisory author. Appendix 4.2 and Appendix 4.3 were not included in the submitted version of the paper, but are included here for completeness.

Chapter 5 of this work is to be submitted for publication as Barnes, N., Mendez, P.F., 2017, "Effect of Cooling Rate on Chromium Carbide Weld Overlays", *Science and Technology of Welding and Joining*. Nairn Barnes was responsible for preparation and conduction of experiments, analysis, and composition of the paper. Dr. Patricio Mendez was the supervisory author. The paper submitted is a slightly altered version of this chapter. Appendix 5.1 was not included in the submitted manuscript.

As the supervisory author on all the papers presented in this thesis, Dr. Patricio

Mendez provided advice for conducting all experiments and for the resulting analysis and interpretation. Dr. Patricio Mendez also revised all publications prior to submission. The format of this thesis is paper-based.

To Rianna, my family, and Ellie, for your love and support.

Acknowledgements

I would like to start by thanking Dr. Patricio Mendez for giving me the opportunity to be a part of the Canadian Centre for Welding and Joining (CCWJ). Stepping into the lab for the first time and meeting Patricio and Stuart forever changed the course of my career and life and I could not be more grateful. Over the six years that I have known Patricio and been involved in the group, we have had been through a lot and I have learned so much about myself and engineering through his mentorship. I believe that it is rare in life to have had a supervisor that has simultaneously been so instrumental in guiding me through my degree and at the same time been someone that I can truly count as a friend. Hopefully he will give me a free signed copy of his textbook solving all welding problems.

To the members of the lab from various generations of graduate students, thank you for everything. To Steven Borle and Stuart Guest, thank you for all the mentorship and many life lessons that you passed on to me. We have certainly had many good nights together and I hope to have more. To my fellow graduate students in no particular order: Cory McIntosh, Vivek Sengupta, Jordan Tsui, Mitchell Grams, Dmytro Havrylov, Rebekah Bannister, Matthew Dewar, Matthew Bell, Kurtis Bell, Ying Wang, Jason Wang, Yi Lu, Satya Gajapathi, and Ata Kamyabi, thank you for all that you did for me, I'm sure I owe many favours and will have many fond memories of all of you. To Goetz Dapp, your constant willingness to help and your friendship have been invaluable to me in getting through my degree and I would like to formally volunteer to read your welding related screenplay. I would like to take the opportunity to make special thanks to Gentry Wood for his friendship and mentorship throughout our long stay in the lab together; if you hadn't walked into my class to pitch the welding lab I don't know what my career would have looked like. I know I can't out-bench you, but I will have to take solace in

my better looks. To everyone I worked with including the undergraduates and anyone I forgot, thank you and I would like to think that I left the lab a happier place with my humour although I likely owe Gentry many apologies for my jokes.

To my closest friends, Mike and Jenna, Justin Lockhart, Scott, Ty, Nathan, Ben and Vy, Adam and Lana, Ben and Brittany, Tomi and Brianne, and Justin Antflick, you have made maintaining happiness and motivation throughout my degree very easy, and I value my relationship with each and every one of you. You have supported me in many different ways and helped me keep perspective on my life and studies.

To my family, thank you so much for everything that you provided me with. Mom and Dad, you gave me a wonderful childhood and all the opportunities that I could hope for in life. I cannot thank the two of you enough for your support and words of guidance in getting me to this point and making every effort to remove obstacles as I pursue my goals. To my siblings, Owen and Michelle (family included), you may not know the extent that your friendship and belief in me has helped throughout my life and in my degree, but I would like you to know how much it has meant to me.

Lastly, and most importantly, I would like to express my thanks and extreme gratitude to my future wife Rianna van Egmond. Your love and support has been of immeasurable help to me throughout my degree and our entire relationship. Luckily, I have the rest of our lives to make it up to you, so no pressure there. I truly value all the sacrifices you have made in allowing me to pursue my goals and you have always been there for me when I needed support. I love you and am lucky I get to spend the rest of my life with my best friend.

To all the institutions and organizations that provided funding, were project sponsors, and supported my endeavours, thank you for enabling me to get through my degree and with any luck your contributions might result in me actually contributing to society.

Table of Contents

List of Tables

List of Figures

Chapter 1

Introduction

1.1 Introduction

The quality and lifetime of wear resistant products is a central issue faced by resource extraction industries in Canada such as mining, oil sands extraction, and large equipment manufacturing. Wear costs for these industries have been estimated at $2.5 billion per year [1]. In intense wear environments without protective coatings, components will fail and halt production. will inevitably fail prematurely and likely interrupt production processes. In the northern Alberta oil sands industry, operational down time carries an estimated cost of $3-6M/day [2]. With such an enormous financial consequence of unplanned shut downs, significant measures must be taken to ensure critical component service life.

Overlays for wear and corrosion protection are a cost effective alternative to manufacturing large scale components entirely of these high performance materials. High hardness materials are excellent in abrasive environments. Ceramic materials are often preferable to metals in extremely aggressive abrasive conditions; however, ceramic particles tend to have poor fracture properties under impact loading and are difficult to process into complex geometries [3]. Metal matrix composites, consisting of ceramic particles dispersed throughout a metal matrix, combine the ductility and process capabilities

of metals with the wear performance of high hardness carbide particles.

Chromium carbide overlays (CCOs) have played a major role where component lifetime jeopardizes production reliability. CCOs represent a majority of the wear protection overlays used in Alberta. Although other systems (Ni-WC) produce lower wear rates, the cost associated with them often limits their application to specific applications and not large surface protection. CCOs are typically deposited using high efficiency welding processes such as submerged arc welding (SAW) [1] and flux-core arc welding (FCAW) for their productivity. The desirable overlay microstructure comes from careful control over the chemistry of the input powders to nucleate primary carbides upon solidification.

CCOs products are often employed on heavy equipment that is operating in erosive environments. CCOs are employed on machine components, where the wear is directly imparted from the abrasive sub-angular quartz sand and heavy minerals in the oil sand. An example of CCO plates in service are those used for Caterpillar D11-R dozer blades, where the plates are formed to the shape on the shovel and welded onto the blade face to provide increased wear resistance (Figure 1.1). CCO plates are also commonly used as liners for heavy hauler bodies, where wear comes not only from the ore being loading directly in the truck bed, but also from direct impacts of the buckets of rope shovels on the heavy hauler beds.

The basis for the CCO materials system is similar to that white cast irons, the largest differences being the extreme cooling rate from welding as well as some compositional variations. The CCO system is based in the Fe-Cr-C ternary system with minor alloying elements added to affect the solidification of the overlay. These alloying elements are not a main focus of research, but include: boron, manganese, molybdenum, nickel, phosphorus, silicon, titanium, and vanadium [5]. The iron-rich portion of the liquidus projection for the ternary system that is relevant to the compositions used to produce CCOs is shown in Figure 1.2. The area of interest in this diagram is the eutectic boundary between the

Figure 1.1: Caterpillar D11 heavy dozer in service [4].

austenite (γ) phase and the M_7C_3 phase indicated by the "Region of Interest" in the figure. The region of interest for the full range of CCO compositions can be considered as 8-35% Cr and 2-9% C [6–9]. The single arrows along the lines shown in Figure 1.2 represent eutectic reactions, whereas the double arrows along lines represent peritectic reactions.

From the composition region of interest in the liquidus projection, there are three possible solidification paths: (1) hypoeutectic, (2) eutectic, and (3) hypereutectic. To the left of the eutectic boundary is the hypoeutectic region. Here, primary austenite solidifies first from the liquid. The remaining liquid cools following the example solidification path 1 (shown in green) indicated in the figure. The result is a eutectic combination of austenite and M_7C_3 carbide formed around the large islands of primary austenite dendrites [11, 12].

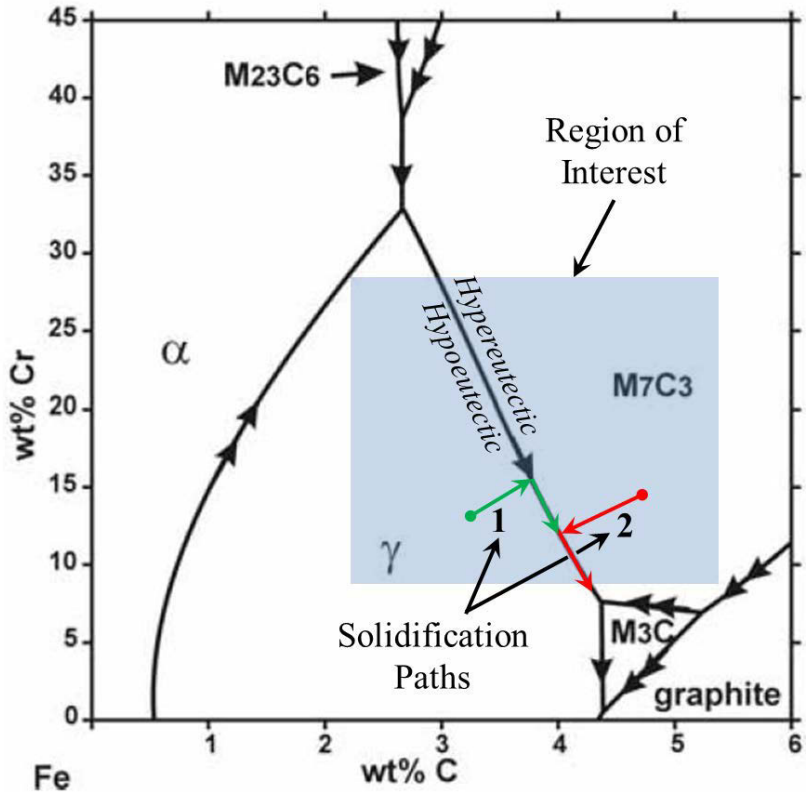

Figure 1.2: Iron-rich portion of liquidus projection for Fe-Cr-C ternary system (modified from [10]).

The eutectic composition gives solidification from the liquid directly on the eutectic phase boundary to eutectic M_7C_3 and austenite. The size and distribution of the eutectic microstructure is strongly dependent on the cooling rate and therefore the heat input from welding [13]. With the cooling rates typical of welding, the peritectic reaction following eutectic solidification is unlikely to occur, meaning that the appearance of M_3C in the solidified structure is highly unlikely [14]. Given the right alloying and slow enough cooling rate, it is possible to reach the peritectic point [12]. The monovariant ternary eutectic reaction predicted is:

$$L \longrightarrow M_7C_3 + \gamma + M_3C \tag{1.1}$$

On the hypereutectic side of the eutectic boundary, primary M_7C_3 carbides solidify first from the liquid, followed by the remaining liquid solidifying at the eutectic composition similarly to the hypoeutectic case. Solidification path 2 in Figure 1.2 (shown in red) shows an example of the hypereutectic sequence. The primary carbides typically solidify as a single crystal, while the eutectic carbides formed are multi-crystalline [15]. As with the purely eutectic composition, there is a possibility of the peritectic reaction occurring, but it is unlikely [16]. The hypereutectic microstructure of CCOs is represented in Figure 1.3. The large hexagonal white particles are the primary carbides, with the surrounding eutectic matrix.

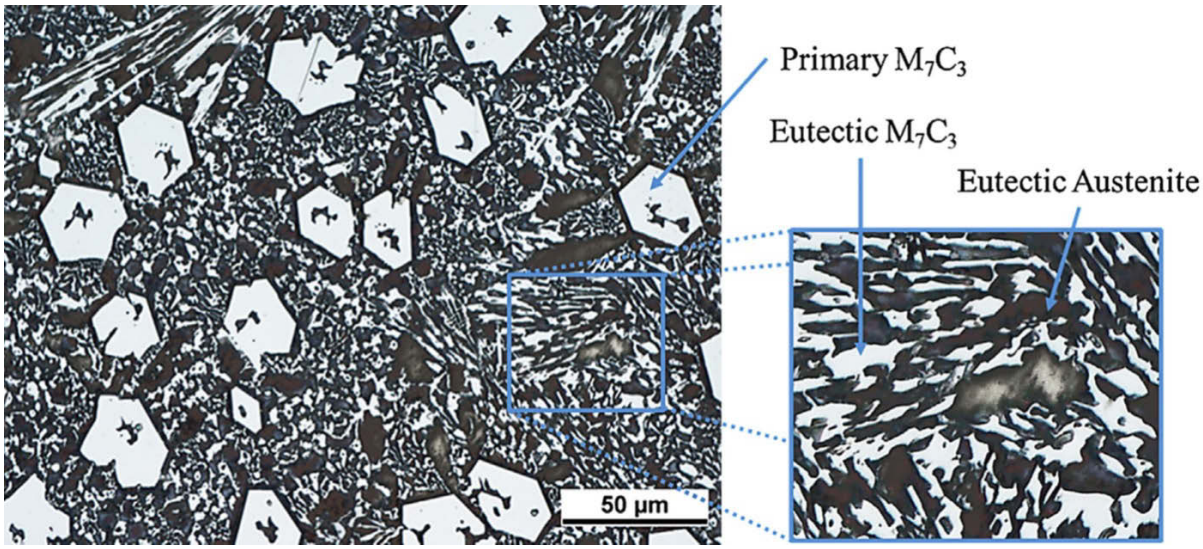

Figure 1.3: Typical CCO microstructure with hypereutectic composition [3].

The main constituents in these overlays that provide wear resistance are the primary M_7C_3 chromium carbides, where M is a combination of Cr and Fe which has a high solubility in the M_7C_3 phase [14]. The M_7C_3 carbides have an orthorhombic (Pnma or oP40) crystal structure [11, 15, 17–23] and a higher hardness than the surrounding eutectic. [22] The hypoeutectic form of the CCOs is considered undesirable for wear resistance applications, as no primary carbides are present following solidification. The

focus of the thesis is therefore solely focused on the hypereutectic compositions from the liquidus projection.

The relevant wear and matrix properties of the primary M_7C_3 carbides as compared to other hard carbide phases that are used in coatings can be seen in Table 1.1.

Table 1.1: Properties of reinforcement carbides affecting wear resistance [24].

Carbide	**Hardness (HV)**	**Density (kg/m^3)**	**Melting Point (^{o}C)**
B_4C	3670	2500	2450
TiC	3000	4900	3100
W_2C	3100	17200	2785
VC	2900	5700	2700
NbC	2000	7800	3600
WC	1630	5700	2870
Cr_7C_3	**1630**	**6900**	**1755**
Cr_3C_2	1400	6700	1800
Fe_3C	1020	7500	1252

The wear resistance of CCOs is directly tied to the available amount of primary carbide surface area for a given cross section. Therefore to obtain better wear results, the volume fraction of the primary carbides should be maximized. The key to achieving good wear resistance for CCOs is to ensure that the inter-particle spacing is smaller than the abrasive particles. The compromise of having a high volume fraction of primary carbides, is that the ductility of the overlays is negatively affected.

A significant issue associated with CCOs is the microstructural variation through the thickness or "banding" within the cross section of the overlay, which can be seen in Figure 1.4. The banded microstructure means that once the wear resistant layer of the overlay is lost to wear, the remaining portion will be susceptible to rapid wear and will lead to decreased component lifetime. Due to the high heat inputs associated with the application of CCOs, the amount of dilution (mixing of overlay material and base metal) is high, up to 40-50% in the SAW process [5]. The high dilution of the carbon steel base

plate, combined with rapid cooling rate of the weld, leads to a higher concentration of wear resistant carbides at the top of the weld, where the balance of Cr to Fe remains closer to the hypereutectic composition. CCO lifetime is very difficult to predict with the presence of the banded microstructure and as such, requires early replacement which greatly increases the cost.

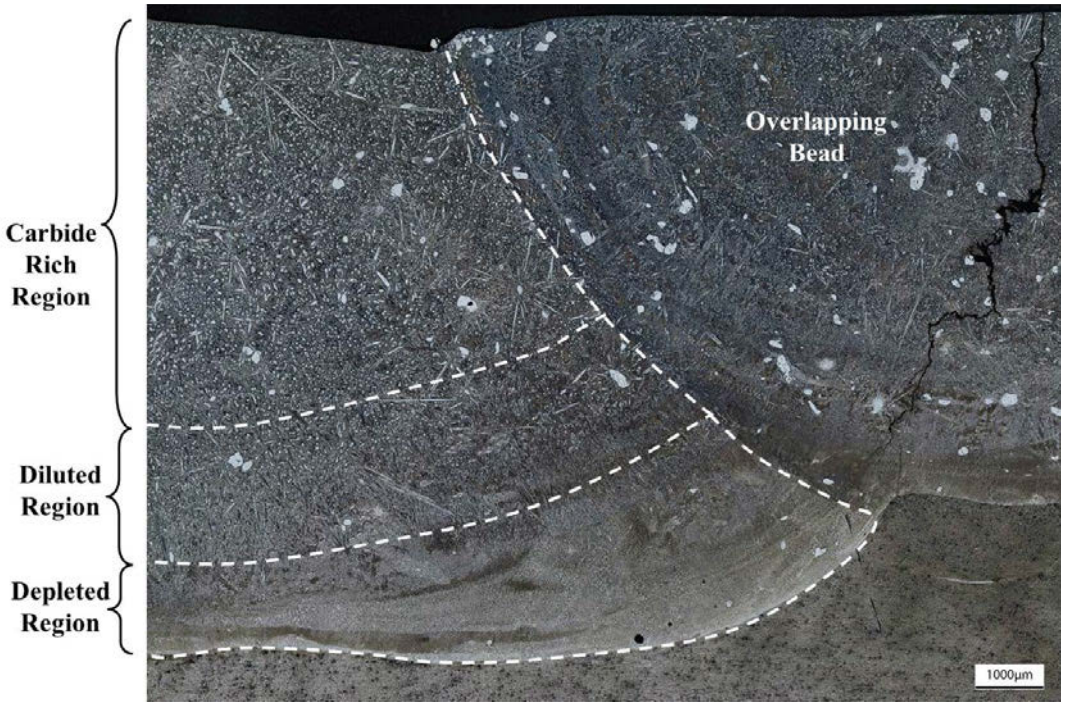

Figure 1.4: Example of banded microstructure present in CCOs.

Developing an in-depth understanding of the formation mechanisms of the microstructure is important. By determining how the relevant features form during solidification based on fundamentals, more control (i.e. composition and cooling rate) can be applied to increasing the fraction of wear resistant particles.

The research work completed aims to improve understanding of the microstructural development of this class of hardfacing alloys and provide increased control to practitioners. The approach to achieving these goals involves applying a fundamental understanding of solidification in combination with experimental trials to build the foundation

of knowledge. The final result provides industrial CCO manufacturers with the tools to implement a more scientific approach.

1.2 Objectives

The main objective of this research project is to provide a detailed understanding of various phenomena present in CCOs and to suggest a growth mechanism for the primary M_7C_3 carbides that will allow manufacturers a deeper understanding of the overlay microstructure, as a path to predicting microstructure of the welds. In order to achieve these goals, the following objectives have been established:

- Perform an analysis of the primary carbides that provides a definite answer to the inconsistency regarding carbide morphology in literature.
- Analyse the large anomalous features present in CCOs to determine their origin and their effect on the microstructure and performance of the overlays.
- Develop a model to describing the growth of the primary carbide needles and compare the theory to the results of quantitative in-situ visualisation experiments.
- Quantitatively evaluate the effect of cooling rate on the microstructure of CCOs.

These objectives are specifically geared towards improving the understanding of CCOs, but can be extended in theory to other carbide needles and metal-matrix composites.

1.3 Thesis Outline

This thesis consists of 5 chapters (not including the introduction) focusing on achieving the above objectives. An brief outline of each chapter is included below.

- Chapter (2) presents a analysis of the primary M_7C_3 morphology. A 3D microstructure reconstruction was completed and analysed to show that the distinct carbide morphologies described in literature are in reality one morphology at different sectioning planes.

- Chapter (3) outlines a the investigation into the origin and effect of large anomalous features observed in the microstructure of CCOs.

- Chapter (4) is the keystone publication of the thesis, which presents the model describing the diffusion-controlled growth of the faceted primary carbide needles. The growth model is then compared to in-situ observations of CCOs solidifying.

- Chapter (5) presents a study performed to quantitatively determine the effect of cooling rate on the microstructure. The results, in conjunction with the growth model proposed in Chapter (4), provide insight to understand and predict primary carbide morphology and thereby overlay properties.

- Chapter (6) summarizes the major findings of the thesis and the main conclusions. An accompanying future work section is included to discuss issues worthy of further investigation and expanding upon the results of the thesis.

Chapter 2

3D Microstructure Reconstruction of Chrome Carbide Weld Overlays

2.1 Introduction

Overlays for wear and corrosion protection are a cost effective alternative to manufacturing large scale components entirely of these high performance materials. Chrome based weld overlays have played a major role in oil-sands, mining, and processing applications, particularly where component lifetime jeopardizes production reliability. CCOs are typically deposited using the high heat input weld processes such as submerged arc welding (SAW) [1] to completely melt the overlay feed material and a small amount of the base material. The desirable carbide structure comes from careful controlled chemistry to nucleate primary carbides upon solidification.

CCOs are based on the Fe-Cr-C ternary system, with high mass fractions of chromium and carbon in the weld overlay to form primary carbides. The common overall composition of CCOs falls in the hypereutectic range. The primary M_7C_3 carbides are the main constituent providing wear resistance in CCOs and white irons. The M_7C_3 carbides precipitate first during solidification, with the eutectic combination of austenite and carbide forming last [25]. These primary carbide particles have a higher hardness than the sur-

rounding eutectic colonies and to obtain better wear results, the volume fraction of the primary carbides relative to the surrounding matrix should be maximized. The morphology and orientation of carbides also play an important role in wear resistance [26].

Literature on CCOs is inconsistent in identifying the structures seen under a microscope. Two M_7C_3 carbide morphologies have been observed in CCOs [16, 27–30] and are illustrated in Figure 2.1. One of the morphologies consists of hexagonally shaped smaller carbides, known as rods, and the other morphology consists of elongated carbide particles, referred to as blades. The continued use of the "rod" and "blade" labels has been a source of confusion in the field. It has been hypothesised that these two morphologies are really the same hexagonal rods which appear to be distinct due to the orientation of the section being examined [31]. Conclusive evidence proving or disproving this hypothesis has not existed until now.

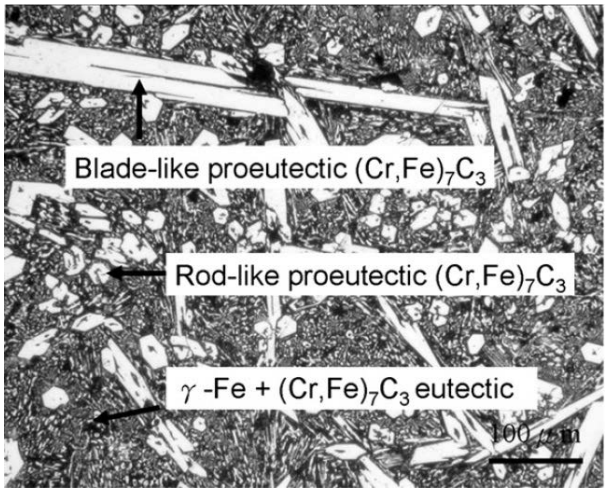

Figure 2.1: CCO microstructure from work done by Chang et al. illustrating the two types of carbide particles [27].

Among the work in which rods and blades are considered different features are the research by Chang et al. [27] and Liu et al. [28]. In work done by Chang et al. [27] carbides were classified into the two distinct morphologies, despite measuring comparable compositions for both structures. They discussed that previous research showed a transi-

tion from the formation of blade like to rod like carbides that was directly related to the amount of carbon in the weld. It was hypothesised that increasing carbon content would increase the fraction of aligned rods in the overlay. A relatively high carbon content of 5.21 $wt\%$ in the overlay increased the presence of rod-like carbides in the cross section, which they theorized was due to an increase in the number of available nucleation sites during solidification. With a lower carbon mass fraction of 3.61 $wt\%$, they observed fewer carbide particles overall which were more randomly oriented and a mix of blades and rods. Again, this was attributed to fewer nucleation sites, which caused the carbide growth direction to be more random. The conclusion drawn from the study was that compositional effects on solidification behaviour governed the morphology and alignment of the primary carbides divided into blade and rod types [27].

Liu et al. found that by applying an electromagnetic field to the molten pool during solidification, they were able to align the carbides particles to obtain a sectioned microstructure that consisted entirely of rod like carbides [28]. Here the use of the rod and blade titles for these carbides imply different carbide morphologies rather than the same.

On the other side of this debate there are several research groups that have discussed the rods and blades as being the same features. Wang et al. showed that the blade-like carbides were oriented in the vertical and transverse directions and that the rod-like carbides existed along longitudinal direction [26]. Their findings suggested that the two distinct carbide morphologies are the same feature, with an image dependent on the orientation of the cut. In their work, the wear properties were far more favourable with the rod like carbides oriented parallel to the direction of wear, so that the particles impacted the rod faces and not the side of the rods. This result suggested that directionality had a direct effect on wear performance [26].

Commercial literature [32] has suggested rods and blades are the same, as illustrated in Figure 2.2. If the cut is perpendicular to the length of the carbides, the appearance

is rod-like, but the closer the cut is to parallel along the length direction, the more the carbide will appear to have a blade-like morphology.

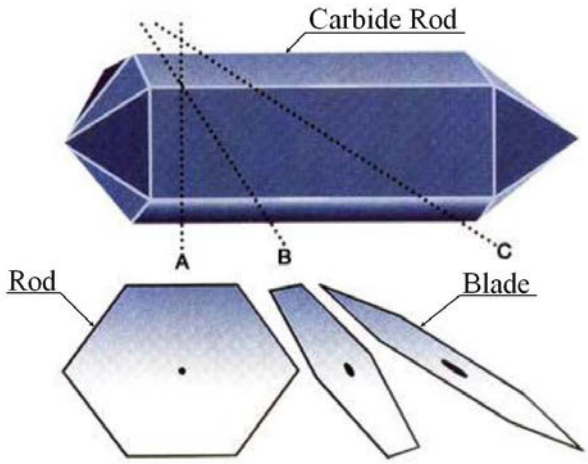

Figure 2.2: An M_7C_3 carbide rod showing how the morphology of rods and blades can originate from the cutting angle (adapted from Triten material. [32])

Despite the high likelihood of rods and blades being the same and the amount of work where they were assumed to be the same, the misconception of considering two different primary carbide morphologies has persisted. The conflicting views on carbide morphology can be settled by generating a 3D reconstruction of the microstructure, which was the focus of this paper. The following sections review the techniques available for the 3D reconstruction and describes in detail the experimental approach taken and its justification.

2.2 Production of Overlays

The overlays reconstructed in 3D were produced using the SAW process with a Power-Wave Lincoln ACDC 1000 SD power supply. The sample used for the 3D image reconstruction, was a 6.4 mm thick overlay on 6.4 mm thick substrate. The 3 mm x 7 mm sample was removed from the overlay sample. The welding consumables utilized were

low carbon steel Lincoln L-61 3.2 mm diameter welding wire, OK Flux 10.71 flux, and proprietary CCO powder blend. The weld parameters are shown in Table 2.1.

Table 2.1: Parameters used for welding the 6.4 mm on 6.4 mm overlay reconstructed in 3D.

CTWD[1]	Voltage	Travel Speed	Oscillation Speed	WFS[2]	Powder:Wire
31.75 mm	33 V	245 mm/min	3.175 m/min	1.63 m/min	1.75

2.3 Serial Sectioning and 3D Reconstruction of Metallurgical Samples

The technique chosen in this work was based on serial sectioning of the microstructure, followed by computer reconstruction. Other techniques such as X-ray tomography [33] were insufficient for the size of the analysis volume needed in the CCO material which has a high opacity and a low contrast.

The serial sectioning of CCOs brings the challenge of removal of a hard material specifically designed for wear protection. The high resistance to wear makes it unsuitable for equipment involving CNC milling operations [34–36]. Instead using a polishing approach such as used for the characterization of SiC composites in an aluminium matrix as in work done by Ganesh et al. [37] was more applicable.

Accounting for the depth of each sectioning step is a challenge. When implementing a polishing approach, external measures, such as callipers or micrometers are unsuitable, and it is necessary to use a fiduciary marking technique.

A common technique to fiduciary marking in serial sectioning is to use hardness indentation [37]. In CCOs, with a typical hardness of 1500 HV and above, the depth of

[1]Contact Tip to Workpiece Distance
[2]Wire Feed Speed

a 50 kg indentation would be 63 μm or less, which is much shallower than the intended 300 μm necessary to capture the whole shape of carbides. In this research, the depth of removal at each step was calibrated on the sample based on the time of polishing.

The procedure chosen for serial sectioning prior to 3D reconstruction was as follows: mounting the specimen and three ball bearings in epoxy, repeated polishing and etching stages, depth calibration to polishing time, and 2D image capture of each section using optical microscopy. Figure 2.3 illustrates the mounted specimen surrounded by two 4.76 mm ball bearings and one 7.93 mm. The purpose of the ball bearings was to gain an accurate method of determining the depth difference between sections. The CCO sample measured 3 mm x 7 mm and was removed from the larger sample described in the following section.

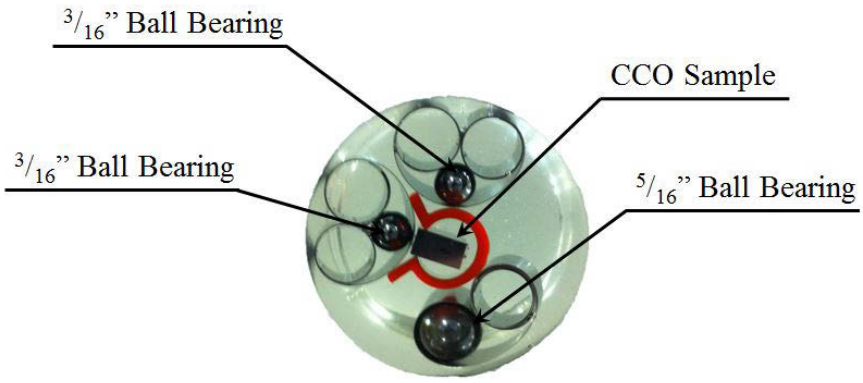

Figure 2.3: CCO sample mounted in epoxy, surrounded by three ball bearings for depth measurement between sections.

Etching was conducted after each polishing step to clearly define the carbide phase from the austenitic phase. The etchant chosen coloured the carbide white and preferential corroded the austenite phase, which maintained a grey colour, making phase identification using computer software less complex and significantly more accurate. The etchant used was a mixture consisting of 10 ml of hydrochloric acid, 20 ml of nitric acid, 5 g of iron chloride powder, and 40 ml of water. Due to the powerful nature of the etchant, the

etching time was short, approximately ten seconds.

The calibration to maintain constant depth increase between polishing steps is shown in Figure 2.4 and was achieved through trigonometric evaluation of the ball bearings mounted around the sample. Following each polishing step the ball bearings are worn away to expose the circular cross section which can then be measured. The cross section of the ball bearing is represented schematically in Figure 2.5. Equation (2.1) allows for calculation of the depth, h, based on the measured a value and the constant radius, r.

$$h = 0.5r(-2 - \sqrt{4 - 4(a^2 r^{-2})}) \tag{2.1}$$

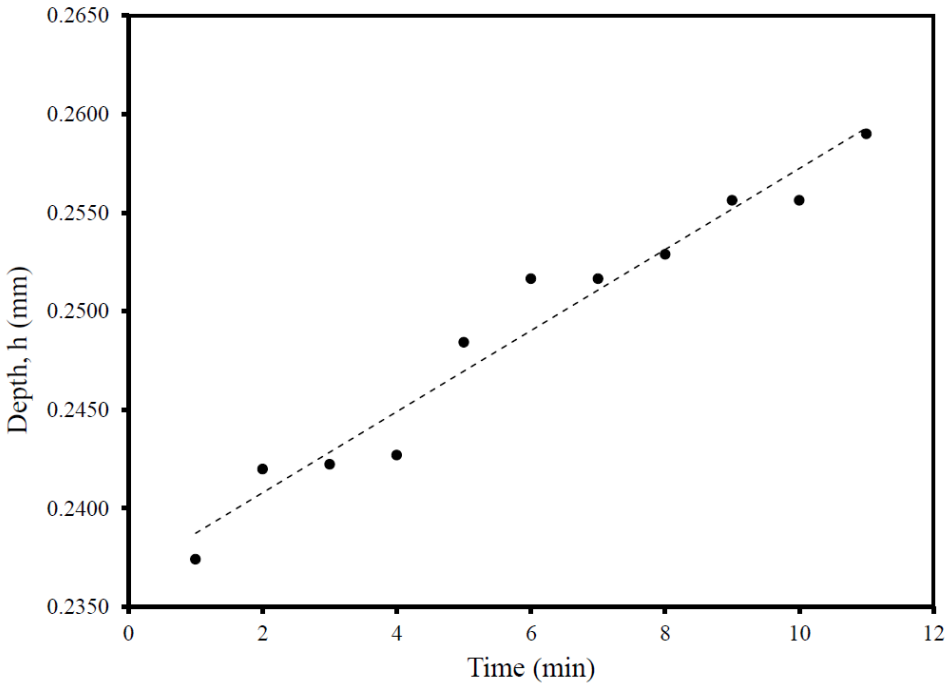

Figure 2.4: Plot of polishing time vs. resulting depth to determine appropriate procedure for 5 μm sectioning schedule.

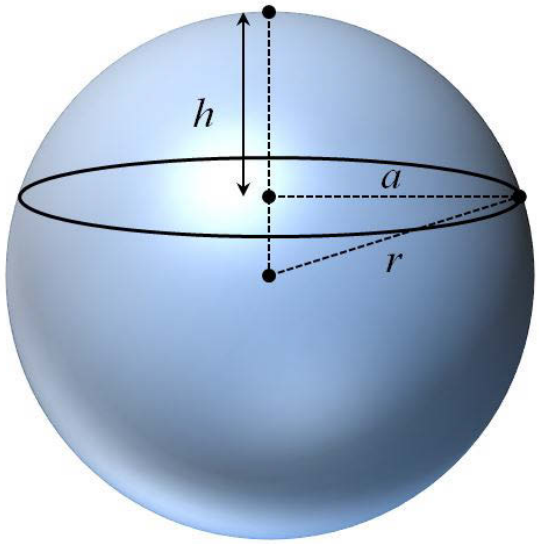

Figure 2.5: Representation of the cross section of the polished ball bearings.

The process of serial sectioning was carried out using a series of sixty images taken after each polishing step of 143 seconds. The steps correspond to 5 μm depth intervals, which is half the average rod diameter of 10 μm. Polishing time between each depth change was found based on the trend-line shown in Figure 2.4. The depth increase of 2.1 μm/min $\pm$1.4 μm/min is based on the slope of the trend-line. The error band of $\pm$1.4 μm/min on the slope relates to a 95% certainty level and a coefficient of determination, R^2, of 0.9573. The sixty images were then compiled using specifically coded software.

2.4 Computational Processing

The images were processed in several steps through the creation of a C++ program which functions in the manner described below. Firstly the image is flattened into a grayscale format, which is defined by a pixel range between 0 and 255 pixels. A sub- range of the total grayscale pixel range is selected, and any pixels not falling within this sub-range are then discarded from the image. A Gaussian blur operation [38] is then performed to

accommodate issues encountered from deep scratches and blend these artifacts into the image. The blurring operation does not cause noticeable distortion to the other features in the image, or remove the cored microstructure present in the primary carbides. The effect of Gaussian blurring can be seen by comparing Figure 2.6*a* to Figure 2.6*b*. Once the image has undergone grayscale thresholding, two morphological operations are performed to allow for removal of the eutectic matrix surrounding the primary M_7C_3 carbides. The first of these operations is known as "Opening" [39], which refers to a 3×3 paint kernel being traced around each connected component in the image. The 3×3 paint kernel is then subtracted and the same traced kernel is then added back to the image to minimize the image degradation. The Opening operation breaks apart components in the image connected by very few pixels and is repeatable as necessary. The resulting image from the Opening operation is then broken apart through the second morphological operation known as "Erosion" [39]. The Erosion operation involved using a 2×2 paint kernel to ensure that all of the eutectic microstructure has sufficiently low size to be removable using an area thresholding step, which discarded all components below a specified size.

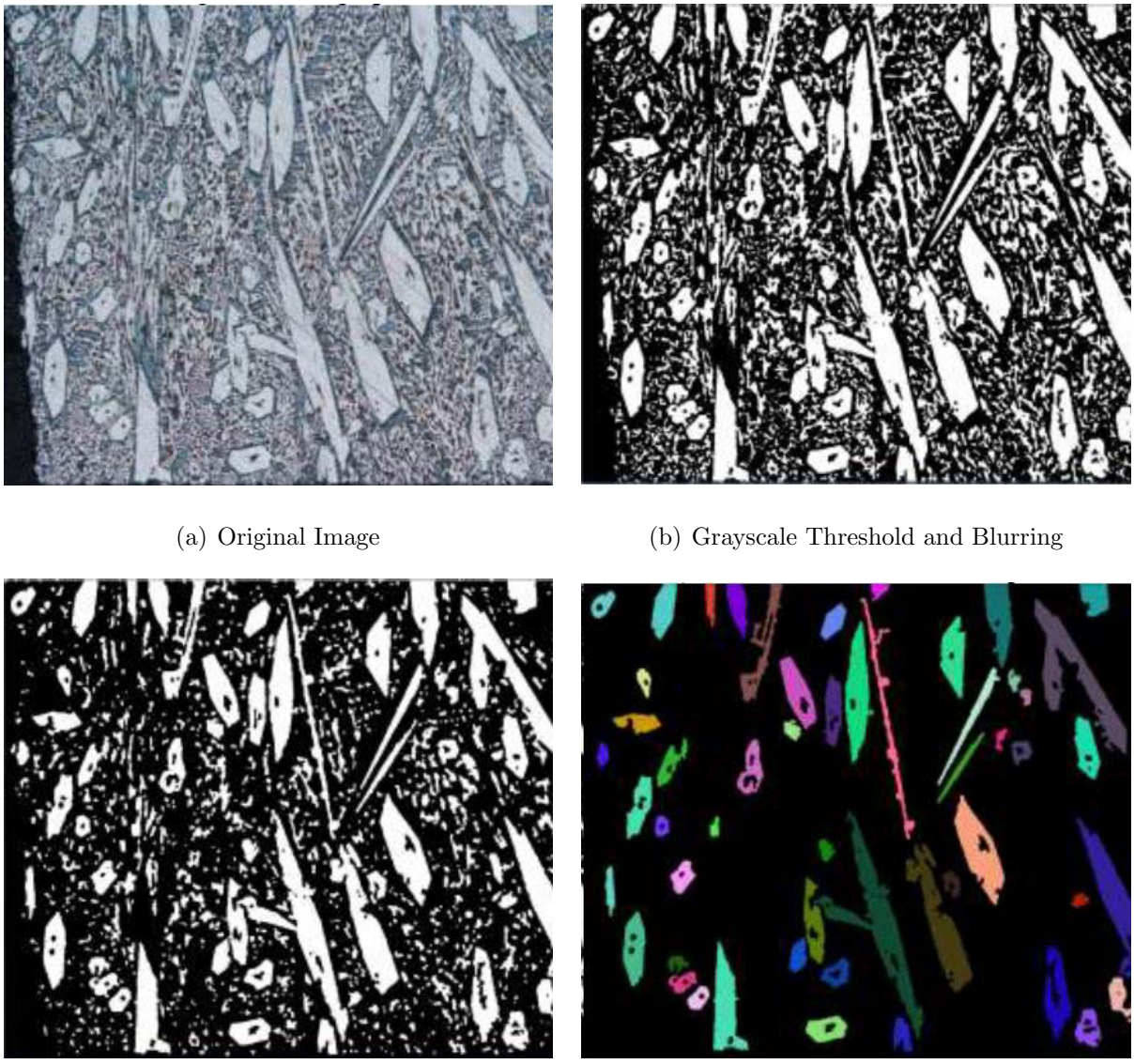

(a) Original Image

(b) Grayscale Threshold and Blurring

(c) Morphological Operations

(d) Area Threshold and Coloring

Figure 2.6: Semi-automated image analysis procedure for 3D stacking visualization showing: a) the original image, b) grayscale thresholding and Gaussian blurring operations to eliminate polishing artifacts, c) opening and erosion operations to break apart the eutectic structure, and d) area thresholding operation and primary carbides colouring.

Once the eutectic matrix had been removed, the primary carbides were then individually coloured with their own distinct colour to allow for tracking throughout all the sections. To ensure proper tracking of each of the carbides particles through the depth

of the volume, a simple method was developed. The tracking involved logging the location of the centroids following the random colouring of the first image, then the program would sort through the centroid locations from the previous image and determine the carbides whose centroid had the closest proximity in the following image. The individual primary carbides were then coloured the same as they had been in the previous image. The tracking process assumed that there were never two carbides in the current image equidistant to a centroid to avoid colouring them the same. The procedure was effective in identifying and properly colouring the primary carbides. When two carbides began to overlap, manual recolouring was needed to prevent them being considered as a single component, which was rare. After the colouring processes, the images were then stacked together in 3D. Since each carbide was individually coloured, it was easy to separate individual carbides from the 3D section and observe changes throughout the depth of the sample.

2.5 Results

Based on the serial sectioning images, a 3D volume was constructed showing the structure of the carbide particles. The full dimensions of the volume reconstructed were 300 μm deep and 600 μm by 600 μm along the square cross section. This volume with the colour coded primary carbides is shown in Figure 2.7.

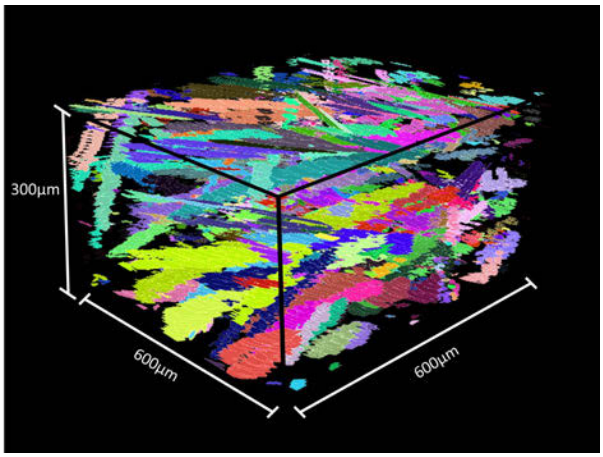

Figure 2.7: Rendered 3D reconstruction of CCO volume element.

Figure 2.8 shows a top view of the 3D reconstruction in which the colour coding was given a small amount of transparency for better visualization. From the image, the primary carbides described as rods are oriented lengthwise in the depth direction of the volume and do not vary in position throughout the sections. The other carbides that are non-aligned in the depth direction of the volume are the "blades".

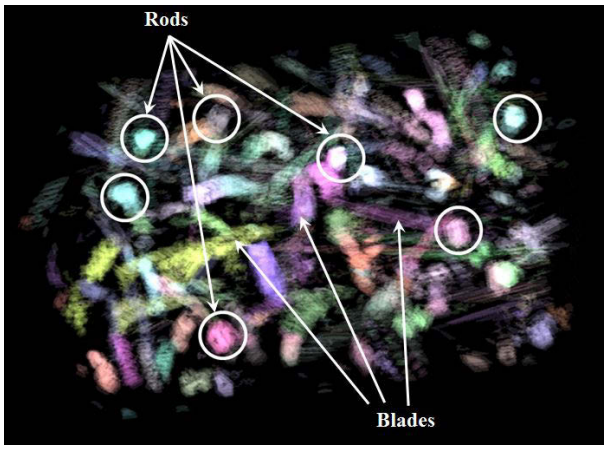

Figure 2.8: Top view of 3D reconstruction indicating the rod (circled in white) and blade appearance.

The morphology of blade-like carbides can be extrapolated by viewing the variation of the carbides' shape and position from one image to the next. The apparent differences in

between the rods and blades are illustrated in the micrographs shown in Figure 2.9, which represents a series of six section taken successively with 5 μm depth spacings between each one. The "blades" are primary carbides oriented almost parallel to the cross section plane instead of perpendicularly, in the depth direction of the 3D visualization.

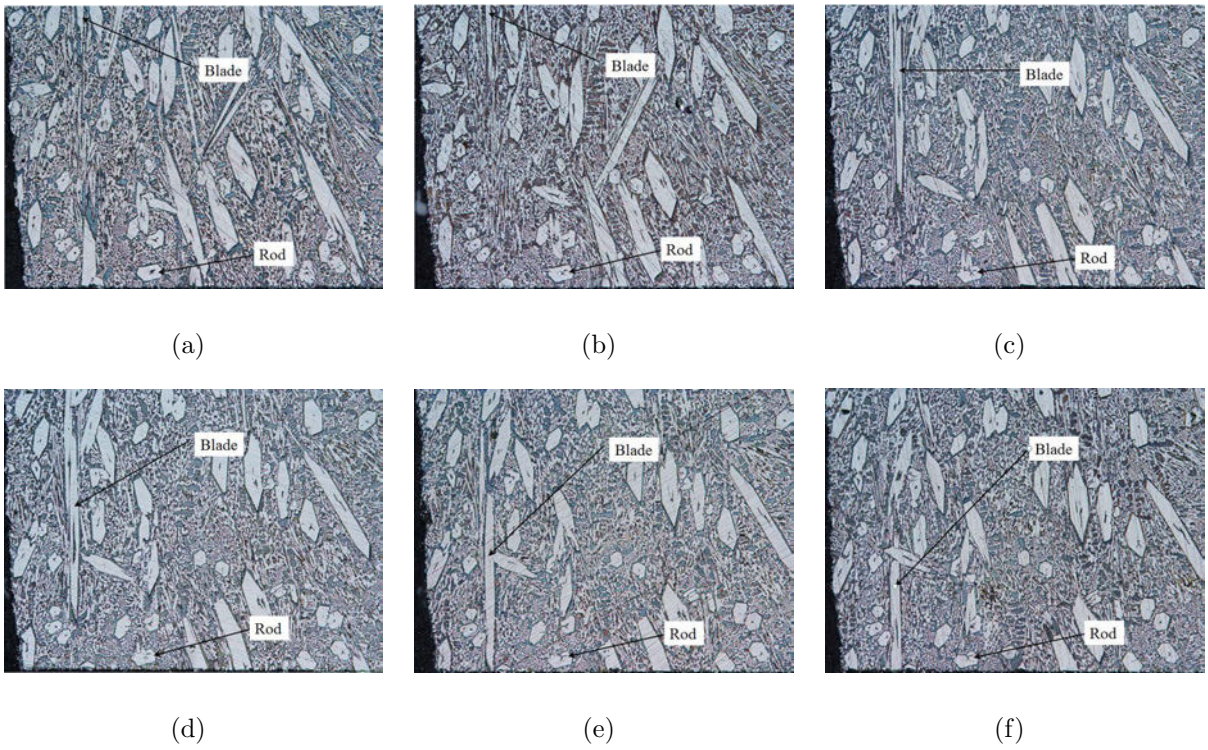

Figure 2.9: Microstructural sections taken in order from (a) through (f) illustrating the particles shifting between sections.

The top view of the 3D volume reconstruction illustrated in Figure 2.10 shows isolated primary carbides, where the morphologies appear very similar in shape and diameter. The similarity between the two carbide classifications can be verified by examining Figure 2.11. From the two carbides shown, it can be seen that the blade-like carbides have the same diameter as the rods, showing that the morphologies are the same. The observation of the similarity between the diameters of the blades and rods confirms the hypothesis that they are the same morphology, which appear different due to the orientation of the cross

section viewed.

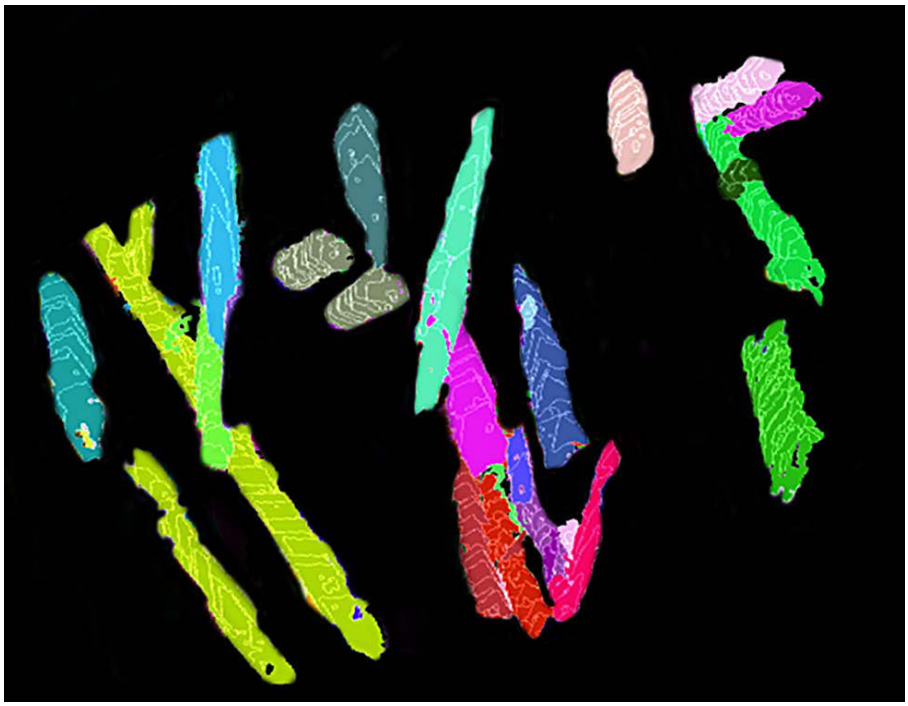

Figure 2.10: Top view of the rendered 3D reconstruction with isolated primary carbides.

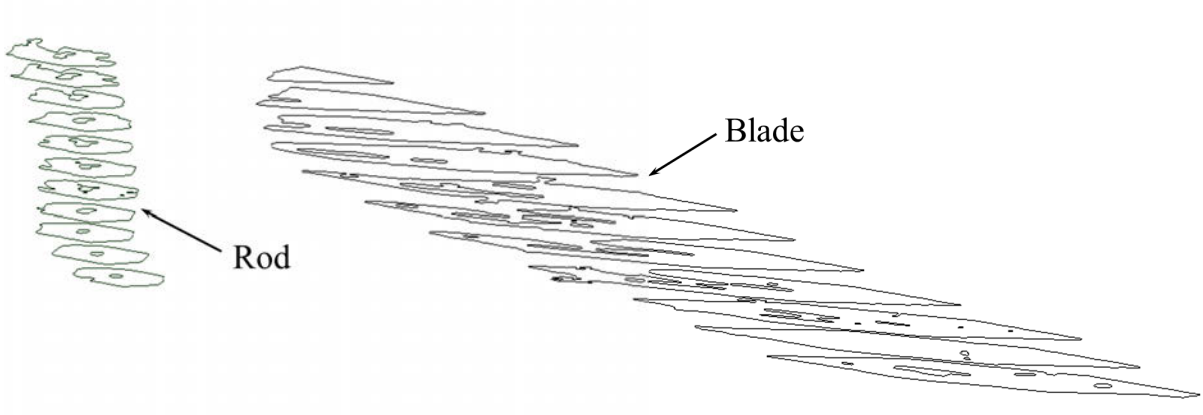

(a)

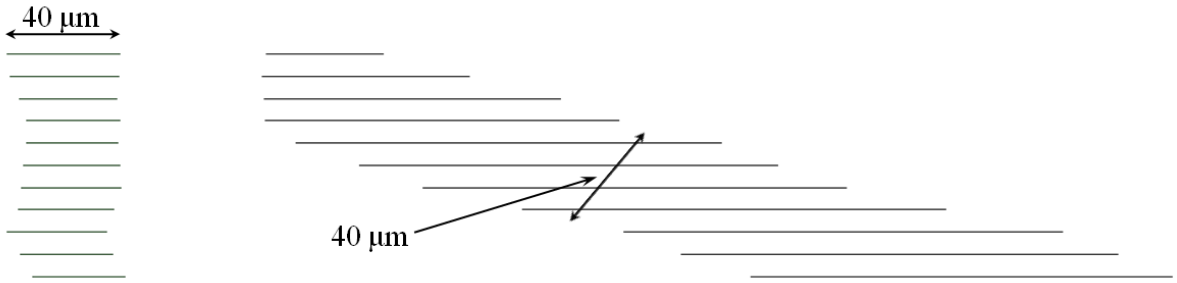

(b)

Figure 2.11: Isolated and sectioned rod-like and blade-like carbides shown from: a) 3D view and b) side view of the two carbides.

The observation that the primary carbides previously separated into two distinct categories have the same morphology is novel. The 3D visualization of the microstructure was an essential tool in enabling the conclusion provided by this work.

2.6 Discussion

The expected result that rod and blade-like carbides are the same primary carbide morphology with different orientations was confirmed. The depth between sections for serial sectioning was correlated to the cross section diameter changes between polishing steps

by using ball bearings of known diameter. The developed procedure for sectioning allowed for an efficient routine to be implemented. Although the ball bearings were not examined after each polishing step, the oblique primary carbide rods appeared to be straight which is consistent with uniform polishing steps.

The error in calibration was 1.4 μm/min, which seems significant, but in reality corresponds to a R^2 of 0.9573 which is an indication of a high quality regression. The use of equal polishing time intervals was also beneficial to avoid the noise of direct measurements of the ball bearings at each step.

Figure 2.7 shows what appears to be branching in some carbides. Detailed inspection of the micrographs suggests that this phenomenon is likely two primary carbides in close contact that the software was unable to properly resolve.

The carbide branching observed in Figure 2.10 was determined to be carbide overlap and not a primary carbide growth phenomenon. The carbides observed were typical in shape and size, which indicated that this result would be representative for all typical CCO samples. The approach was successful in dealing with a hard material with large features in a way that had previously never been attempted.

2.7 Conclusions

The 3D characterization of CCOs was completed for the first time through the combined use of serial sectioning, image analysis software and computer software for 3D reconstruction. A novel way of tracking the depth of polishing using the sectioning of ball bearings proved to be successful.

Based upon the 3D reconstruction and characterization, the primary carbides particles previously separated into two distinct categories, rods and blades, were confirmed to be the same feature observed from different directions. The blade-like carbide particles

observed in 2D sections of CCOs are in fact rods with the longitudinal axis parallel to the section cut.

2.8 Acknowledgements

The authors would like to thank Gentry Wood for his help in this project, Wilkinson Steel and Metal for sharing their technical expertise, and Lincoln Electric for the welding equipment and consumables. This grant was partially funded by the NSERC Discovery program.

Chapter 3

Large Anomalous Features in the Microstructure of Chromium Carbide Weld Overlays

3.1 Introduction

Wear and corrosion resistant overlays are used to prolong the lifetime of large scale components. By providing a wear resistant surface for a tough base material, overlays can help achieve an excellent balance of properties. Chromium carbide weld overlays (CCOs) play a major role in oil-sands, mining, agriculture, and processing applications, particularly where production reliability is important. [3,40] CCOs are typically deposited with welding processes such as submerged arc welding (SAW) and flux-core arc welding (FCAW) due to their high productivity. [1, 3]

CCOs are weld-deposited overlays based on the Fe-Cr-C ternary system, with high overall fractions of chromium (typically 8-35 wt%) and carbon (2-9 wt%). The most wear resistant CCOs solidify with a primary M_7C_3 carbide solidification path. Higher volume fractions of primary carbides typically result in better wear resistance. [15, 28] The primary carbides have the nominal stoichiometric composition of M_7C_3, where M is mostly Cr, with smaller amounts of Fe and other alloying elements. The composition of

CCO overlays is achieved by mixing powders rich in iron, chromium, carbon (e.g. "ferro-chrome"), and containing other alloying elements. The primary M_7C_3 carbides are the first microstructural feature to solidify, and they have the morphology of a rod with a hexagonal cross section, often with a thin austenite core running along the centre of the rods. [41–43] The primary carbide rods are surrounded by a eutectic combination of austenite and M_7C_3 carbide forming from the remaining liquid. [25] The M_7C_3 carbides have an orthorhombic (Pnma or oP40) crystal structure [17–21] and a higher hardness than the surrounding eutectic. [22]

Large anomalous features (colloquially called "rice crispies" by practitioners) have been observed in the microstructure of industrially made CCOs. Figure 3.1 shows these features distinguished from the surrounding primary carbides and eutectic matrix by their rounded morphology and large size (approximately 100 μm or larger in diameter). From previous work, it is known that the light coloured elongated features are primary M_7C_3 carbides. [5, 7, 25, 44] Typical CCOs contain less than 1 vol% of LAFs. Although the features are common and well known to practitioners, they have not previously been discussed in literature and no information was available to assess their origin and possible implications on overlay performance and quality.

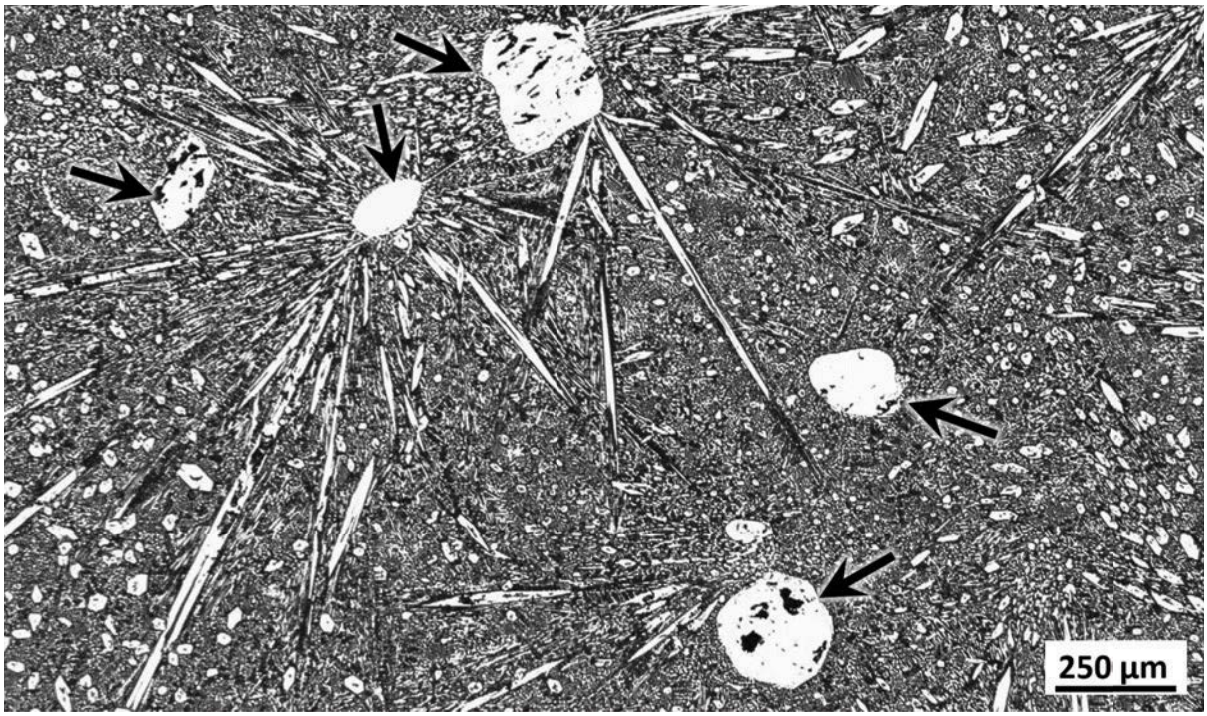

Figure 3.1: Large anomalous features,indicated by arrows, surrounded by primary carbides in the eutectic matrix. [5]

Until the work presented here, the origin and effects on performance of the LAFs has been unknown. Explanations so far have not had a solid foundation, and fall in two mutually exclusive categories: that LAFs are large primary carbides, or that LAFs are unmelted input powder. These opposing theories imply very different consequences for the overlay; for example, if the LAFs are primary carbides, hotter welds could result in coarsening and more LAFs, while if the LAFs are unmelted powders, hotter welds would result in fewer LAFs. The goal of this paper is to determine the origin of LAFs to assist on the interpretation of CCO microstructures.

Welding trials were preformed to explore the link between welding energy and the presence of LAFs. Experimental CCOs deposited by SAW using three different polarity modes were completed: 100% electrode positive (EP), 75% EP and 25% electrode negative (EN), and a 50% balance of EP and EN. The motivation behind these experiments

was that with more EN polarity, the energy balance of welding shifts from the bead towards the electrode, resulting in a colder bead.

The welds were completed using a Lincoln AC/DC 1000 welding machine with identical parameters and variations in the balance of the AC cycle. The welding parameters were a voltage of 33V and a travel speed of 4.18 mm/s. Table 3.1 summarizes the results of the welding trials. The results indicate that lower heat inputs have resulted in higher amount of LAFs. [5, 45]

Table 3.1: Welding parameters for AC SAW trials and variation of volume fraction of LAFs.

Balance	**Heat Input (kJ/mm)**	**Current (A)**	**Vol. Frac. LAF**
100% EP	4.5	568.3	0.6
75% EP	4.0	503.0	1.0
50% EP	3.6	459.6	5.4

The welding trials using SAW provide evidence that reducing the energy into the base plate and powders results in higher amount of LAFs in a microstructure. These results support the theory that the LAFs are unmelted powders.

3.2 Experimental Procedure

Four characterization techniques were carried out to confirm the results of the welding trials. The methods used were micro-hardness indentations, Auger electron spectroscopy (AES), energy dispersive x-ray spectroscopy (EDS), and electron backscatter diffraction (EBSD).

Hardness testing was chosen to compare the LAFs' hardness to that of the primary M_7C_3 carbides. A Tukon 2500 Automated Vickers Hardness Tester with an indenter load

of 100 g force was used to avoid possible cracking around indents, which is common due to the brittle nature of the LAFs. Two LAFs were selected from a polished CCO sample to be representative of the whole population, and five Vickers indentations were made on each one to get an average hardness.

AES was chosen to provide a precise compositional analysis of the LAFs with the ability to detect carbon. AES analysis was completed using a JAMP 9500F setup. The characterization parameters used were an accelerating voltage of 2 kV, an emission current of 8 nA, with a working distance of 24 mm, and a sputtering rate of 15 nm/min. Elements selected for quantification were Fe, Cr, C, and O. The measurement error reported was 0.006 at% for all elements.

EDS compositional analysis of the LAFs and the feed powders was completed to compare the Cr and Fe values. All measures were taken on a Zeiss Sigma 300 VP-FESEM setup with an accelerating voltage of 20 kV and a working distance of 8.0 mm. Compared to AES, EDS can provide a reasonable quantification of elements heavier than carbon, but has the disadvantage that it cannot properly detect carbon. [46, 47] Conversely, it has the advantage of not needing a flat surface, allowing analysis of the feed powder.

EBSD phase analysis was performed to compare between the primary carbide phase and the LAFs. Using a Zeiss Sigma FESEM with an Oxford AZtec EBSD detector, two areas were selected for mapping, one focusing on a LAF and the other focusing on several primary carbides. Both maps were analysed using an accelerating voltage of 20 kV and a specimen tilt of 70^o. For the map of the LAF, a step size of 1.338 μm were used to analyse the 100 μm x 80 μm area. For the map of the primary carbides, a step size of 0.4864 μm to analyse the 45 μm x 25 μm area.

3.3 Results of LAF Characterization

3.3.1 Hardness Testing

Vickers hardness testing was performed on 10 points across two LAFs. Five hardness indentations were made in each of the two LAFs selected, yielding average hardness values of 1908±51 HV and 1839±45 HV (variation in standard deviation). The average hardness obtained for the LAFs is comparable to that of primary carbides, which range between approximately 1200 HV to 1800 HV. [3,24,48] From the values obtained, hardness testing alone cannot prove or disprove either proposed LAF formation theory.

3.3.2 AES Analysis

AES characterization was used to determine C, Cr, and Fe content in three LAFs, five primary carbides, and six points in the austenitic matrix. Only Cr, Fe, and C were quantified to develop an understanding of how the main ternary elements involved in CCOs vary between phases; all other alloying elements amount to less than 1 at%. Oxygen content was also measured for all sampling points to ensure no contamination was present. For comparison purposes between phases, the alloying elements present in CCOs were considered negligible. The chosen peaks analysed were the C KLL peak (272 eV), the Cr LMM peak (529 eV), and the Fe LMM peak (651 eV). It should be noted that the error associated with AES measurements for quantitative analysis is only considered relevant on measurement peaks below 200 eV, which the analysed peaks are above. [49, 50]

For reference, the Cr:Fe:C ratios obtained where compared with the overall composition of the CCO, measured using ICP from a 2 g sample, and with the predicted primary carbide composition calculated using Thermo-Calc-3.0.1 with the TCFE6 database [51]. For the Thermo-Calc calculation, a Scheil solidification mode was considered in which

the metallic elements were considered slow diffusers (no diffusivity in the solid, but fast diffusivity in the liquid), and the carbon was considered a fast diffuser (C is assumed to be in thermodynamic equilibrium in the solid and the liquid at each stage of solidification). The results of AES analysis, ICP analysis, and Thermocalc calculation are summarized in Table 3.2. For the mass ratio, only a small error is induced if the particles are assumed to contain only Cr, Fe, and C.

The atomic stoichiometric ratio of metal to carbon in M_7C_3 is (Cr+Fe):C = 2.33:1, and measurements of Table 3.2 correspond to (Cr+Fe):C = 2.38:1 for the LAF and (Cr+Fe):C =2.34:1 for the primary carbide; therefore, both the LAF and the primary carbide have stoichiometries fitting the M_7C_3 composition. The Cr:Fe atomic ratio however, is significantly different between the LAF and the primary carbide: Cr:Fe=3.33 for the LAF, and 1.79 for the primary carbide. The Thermo-Calc calculation suggests an atomic ratio of Cr:Fe=1.24, similar to the composition of the primary carbide, supporting the argument that the LAFs are not primary carbides. The inconsistency between the measured AES composition ratios for austenite and the Thermo-Calc predictions is likely due to oxygen contamination on the austenite in the matrix. AES indicated 8 wt% oxygen at this site, while all other AES sampling points showed negligible oxygen contamination.

Table 3.2: Composition ratios of microstructural constituents. Only Cr, Fe and C were present in high enough amounts to be quantified. Error propagation of elemental ratios based on AES measurement error yield an error of 0.0026 for Cr:C, 0.0078 for Fe:C, 0.0006 for Cr:Fe, and 0.0102 for (Cr+Fe):C. Error propagation calculation is shown in Appendix 3.1.

Sample Point	**Cr:C**		**Fe:C**		**(Cr+Fe):C**		**Cr:Fe**	
	at.	**mass**	**at.**	**mass**	**at.**	**mass**	**at.**	**mass**
LAF (AES)	1.83	7.92	0.55	2.58	2.39	10.50	3.30	3.07
Primary M_7C_3 (AES)	1.50	6.48	0.84	3.89	2.33	10.37	1.79	1.67
Eutectic γ (AES)	4.94	21.28	16.75	77.39	21.69	98.67	0.30	0.27
Primary M_7C_3 (ThermoCalc)	1.29	5.60	1.04	4.84	2.33	10.43	1.24	1.16
Eutectic γ (ThermoCalc)	1.20	5.21	21.37	99.34	22.57	104.56	0.06	0.05
Bulk composition (ICP)	1.81	7.84	4.95	23.00	6.76	30.84	0.37	0.34

3.3.3 EDS Analysis

EDS was used to compare the composition of the powder feed used in the making of CCOs to that of the LAFS. Five representative LAFs were selected from a CCO sample as well as five powders particles from the powder feed. The criteria to select the powder particles or the LAFs consisted on being representative of the population in size and shape under microscopic inspection.

The measured Cr and Fe concentrations are shown in Table 3.3. Based on the measurements from Table 3.3, the null hypothesis "the powders and the LAFs belong to different populations" can be rejected with a 95% confidence. Similarly, the null hypothesis "the powders and the LAFs belong to the same population" can be accepted with a 95% confidence (p=0.28). The Cr:Fe ratio measured with EDS is higher than that measured with AES. The differences between the ratios of the characterization techniques is likely related to the presence of high carbon fractions skewing results in EDS. These observations are consistent with the theory that LAFs are unmelted powders and not

primary carbides.

Table 3.3: EDS Cr and Fe content in wt% of CCO powders and LAFs selected. Average Cr:Fe ratio is 4.44 for the powders and 4.28 for the LAFs.

Sample Point	**Powders**		**LAFs**	
	Cr	**Fe**	**Cr**	**Fe**
Point 1	74.1	17.5	77.2	14.0
Point 2	71.5	20.1	72.3	17.0
Point 3	77.0	14.9	75.9	16.7
Point 4	74.0	17.7	73.6	13.8
Point 5	74.3	17.6	65.4	25.4
Average	**74.22**	**17.55**	**72.88**	**17.39**

3.3.4 EBSD Analysis

EBSD was used to compare the M_7C_3 phase of the primary carbides to the phase of the LAFs. Figure 3.2 shows graphical representations of the EBSD results for the area map selected to analyse a LAF. On the top left (a) is the band contrast map which is similar to a backscattered electron (BSE) SEM image, but also shows contrast based on defects and grain orientation. The phase boundary map shown in the top right (b) shows the superimposed phase boundaries in red on the band contrast image. Due to the chosen step size, some of the smaller phase boundaries were not able to be identified. The step size of 1.338 μm was selected to allow for phase identification and was not chosen to allow for clear grain boundary or phase boundary identification. The phase identification map shown in the lower left (c) identifies the LAF as the orthorhombic M_7C_3 phase (red) and the surrounding matrix as austenite (green) with very small amounts of the $M_{23}C_6$ (yellow) and ferrite (blue) phases. The darker red and greens lines apparent on the phase

identification map represent grain boundaries within the individual phases. The presence of ferrite and $M_{23}C_6$ in negligible amounts warrants further investigation with a smaller step size for confirmation, but it is possible that the ferrite identified here is martensite which has been observed in CCOs [5]. The inverse pole figure in the bottom right (d) shows the distinct orientation directions of each grain with respect to the flat surface of the sample. The phase of interest here is the M_7C_3 phase and the legend corresponds specifically to this phase. The inverse pole figure shows that a large portion of the LAF is the one large grain shown in blue, but the remaining portion of the same LAF is made up of smaller sections above the large blue grain and each has a distinct crystal orientation.

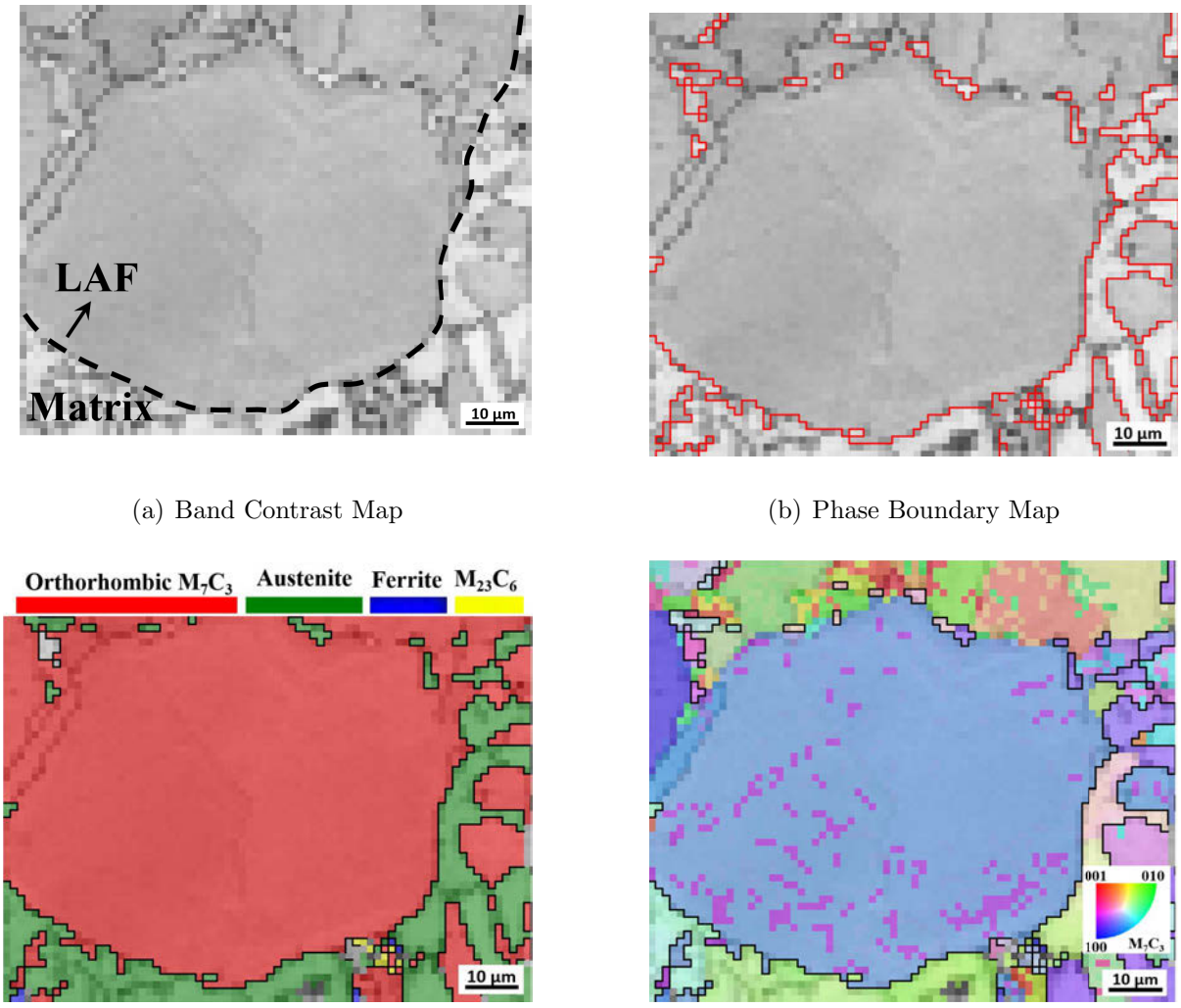

(a) Band Contrast Map

(b) Phase Boundary Map

(c) Phase Identification Map

(d) Inverse Pole Figure

Figure 3.2: EBSD analysis maps of the chosen LAF showing: (a) band contrast, (b) identified phase boundaries, (c) identified phases, and (d) grain orientations.

The characterization maps for the second location analysing primary M_7C_3 carbides are shown in Figure 3.3. The dark phase in the EBSD map is M_7C_3 with the surrounding light matrix being eutectic austenite. Similarly to the EBSD mapping for the LAF, the phase boundaries are indicated in the top right (b) where they are superimposed on the band contrast map (a). The phase map shown in the bottom left (c) shows that the primary carbides here are the orthorhombic M_7C_3 phase (red), and the matrix is made

up of the austenite phase (green) as well as trace amounts of $M_{23}C_6$ (yellow), and ferrite (blue). In the bottom right (d) is the inverse pole figure with the associated legend, which indicates the planar directions for the M_7C_3 phase. The main primary carbide seen in (d) does not have a clear planar direction which could be the result of the sectioning plane seen here being in between two different planes causing the distribution shown here.

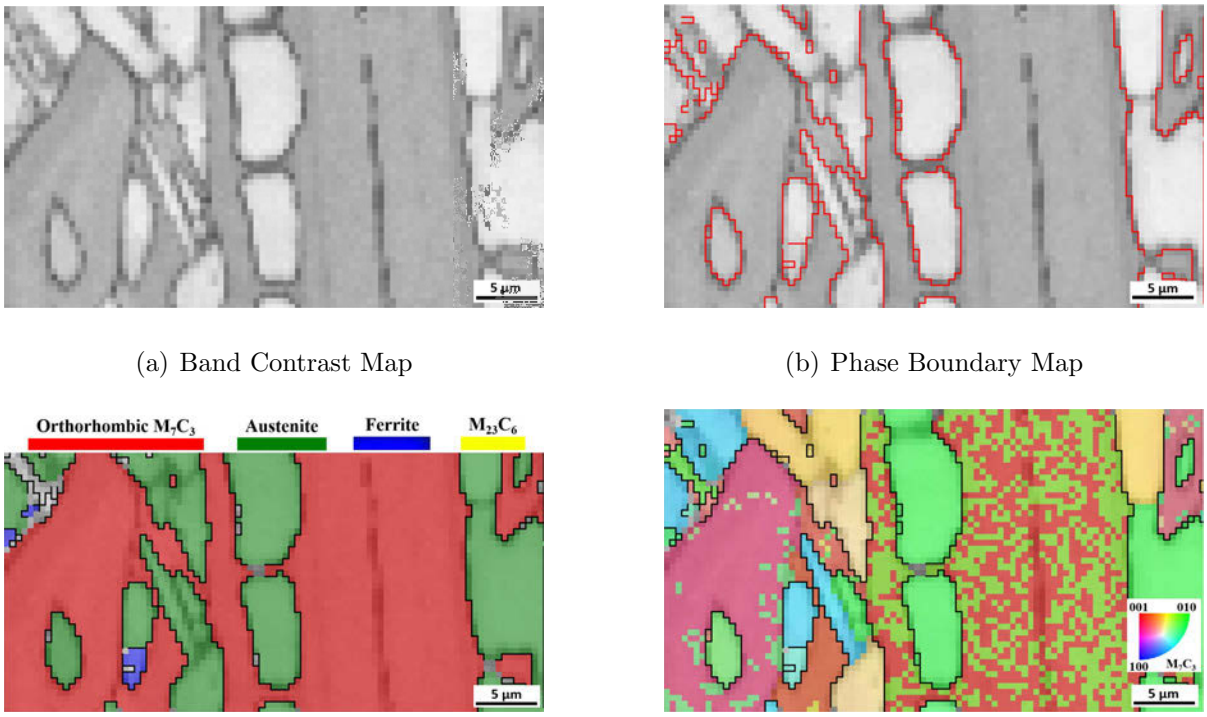

(a) Band Contrast Map

(b) Phase Boundary Map

(c) Phase Identification Map

(d) Inverse Pole Figure

Figure 3.3: EBSD analysis maps of a primary M_7C_3 carbide showing: (a) band contrast, (b) identified phase boundaries, (c) identified phases, and (d) grain orientations.

The results of the EBSD analysis corroborate the AES data showing that the LAFs are made up of the M_7C_3 phase. Although both are the same phase, based on the AES results, they are distinct compositions of the M_7C_3 phase. These observations are not in direct support of the theory that the LAFs are not primary carbides.

3.4 Discussion

The high Cr and C content of the LAFs means that their presence depletes the surrounding melt from these alloying elements. The consequence of this alloy depletion is that there will be fewer primary carbides and decreased wear resistance. This analysis raises the question of whether the amounts of LAF observed are expected to have a significant effect on the remaining microstructure. Computational thermodynamics analysis was carried out in Thermo-Calc using the TCFE6 database and considering a ternary Fe-25 wt%Cr 4.5 wt %C system where the Cr and Fe are slow diffusers and the C is a fast diffuser. The results indicate that a 1 vol% of LAFs would result in a decrease in the amount of primary carbides from 23.92 vol% to 23.45 vol%, and a 5.4 vol% of LAFs (maximum observed in Table 1) would result in a decrease in the amount of primary carbides from 23.92 vol% to 17.79 vol%. The decrease in primary carbides is significant with 5.4 vol% of LAFs and is equivalent to an overall loss of 0.25 wt% of C. The in depth calculation is shown in Appendix 3.2. Lower energy during welding will increase the number of LAFs and decrease the volume fraction of primary carbide.

The effect of undissolved powders in the surrounding alloy can also be observed in Figure 3.4. In this figure, radially oriented primary carbides surround the undissolved powders. This morphology is consistent with directional solidification under a radial compositional gradient. This interpretation is the object of current research outside the scope of this paper.

Figure 3.4: Large anomalous feature surrounded by radially oriented primary carbides.

The increase in amount of LAFs with the EN polarity deserves further research, as it might unintentionally affect the quality of CCOs when manipulated for other purposes; for example, when AC waveform balance is shifted towards EN to decrease dilution.

3.5 Conclusion

The large anomalous features present in CCOs were analysed systematically for the first time through hardness testing, AES analysis, EDS analysis, and EBSD analysis. The characterization performed yields the following conclusions:

- The large anomalous features observed in the CCOs analysed are unmelted ferrochromium powders.
- Vickers indentations showed that the LAFs have a hardness within the range of typical values for primary carbides.

- The results of AES analysis showed that the (Cr+Fe):C for both the LAFs and primary carbides matched the predicted ratio from thermodynamics. The significant difference in the Cr:Fe ratio between the LAFs and primary carbides indicates that while they are both the M_7C_3 phase, they are distinct compositions.

- EDS characterization showed that the Cr:Fe ratios for the LAFs and unmelted ferro-chromium powders are not statistically different.

- EBSD analysis confirmed that the LAFs are polycrystalline, and the same orthorhombic M_7C_3 phase as the carbides.

- The number of LAFs present in the overlay increased with the amount of EN in the waveform balance in SAW, which is consistent with an increase of unmelted powders when the welding energy is less focused on the weld pool.

- The LAFs are often surrounded by radially oriented carbides in a morphology consistent with radial composition gradients during dissolution of the LAF.

3.6 Acknowledgements

The authors would like to thank Wilkinson Steel and Metal for providing funding, samples, and their technical expertise, Yiyu Wang for EBSD analysis and Lincoln Electric for the welding equipment and consumables. This research was funded in part by NSERC and the AWS Foundation.

3.7 Appendix 3.1: AES Uncertainty Analysis

The resolution uncertainty in AES composition measurements is 0.006 at% [52] and the uncertainty in the Cr:C composition ratios were calculated using the error propagation method shown in Equations 3.1 and 3.2. The uncertainty in the Fe:C was calculated in the same way.

$$U_{Cr:C} = \sqrt{\left[\left(\frac{\partial f}{\partial C_{Cr}}\right)U_{C_{Cr}}\right]^2 + \left[\left(\frac{\partial f}{\partial C_C}\right)U_{C_C}\right]^2} \tag{3.1}$$

$$U_{Cr:C} = \sqrt{\left[\left(\frac{1}{C_C}\right)U_{C_{Cr}}\right]^2 + \left[\left(\frac{-C_{Cr}}{C_C^2}\right)U_{C_C}\right]^2} \tag{3.2}$$

Where $U_{Cr:C}$ is the uncertainty in the Cr:C ratio, f is the composition ratio, C_C is the carbon composition, C_{Cr} is the chromium composition, and $U_{C_{Cr}}$ and U_{C_C} are the resolution uncertainty in the composition of Cr and C respectively.

The uncertainty for the (Cr+Fe):C composition ratios is shown in Equations 3.3 and 3.4.

$$U_{(Cr+Fe):C} = \sqrt{\left[\left(\frac{\partial f}{\partial C_{Cr}}\right)U_{C_{Cr}}\right]^2 + \left[\left(\frac{\partial f}{\partial C_{Fe}}\right)U_{C_{Fe}}\right]^2 + \left[\left(\frac{\partial f}{\partial C_C}\right)U_{C_C}\right]^2} \tag{3.3}$$

$$U_{(Cr+Fe):C} = \sqrt{\left[\left(\frac{1}{C_C}\right)U_{C_{Cr}}\right]^2 + \left[\left(\frac{1}{C_C}\right)U_{C_{Fe}}\right]^2 + \left[-\left(\frac{C_{Cr}+C_{Fe}}{C_C^2}\right)U_{C_C}\right]^2} \tag{3.4}$$

Where $U_{Cr+Fe:C}$ is the uncertainty in the (Cr+Fe):C ratio, C_{Fe} is the iron composition, $U_{C_{Cr}}$ is the resolution uncertainty in the Fe composition.

3.8 Appendix 3.2: Weight Fraction Calculation

The overall loss of carbon due to the presence of 5.4 vol% of LAFs was calculated by the method shown in Equations 3.5, 3.6, 3.7, and 3.8.

$$W_{C,adj} = W_{C,CCO} - 0.054(W_{C,LAF}) \tag{3.5}$$

Where $W_{C,CCO}$ is the weight fraction of C in CCOs, $W_{C,LAF}$ is the weight fraction of C in LAFs, and $W_{C,adj}$ is the adjusted weight fraction of C. The 0.054 factor here represents the fraction of LAFs present in the overlay.

The total new adjusted composition is calculated in Equation 3.6.

$$W_{TOT} = W_{C,adj} + W_{Fe,adj} + W_{Cr,adj} \tag{3.6}$$

Where W_{TOT} is the overall adjusted weight fraction found through the addition of the adjusted weight fractions of C, Fe, and Cr. $W_{Fe,adj}$ and $W_{Cr,adj}$ are the adjusted weight fractions of Fe and Cr respectively and were calculated in a manner similar to $W_{C,adj}$.

The final weight fraction calculation after normalization is shown in Equation 3.7.

$$W_{C,f} = \frac{W_{C,adj}}{W_{TOT}} * 100 \tag{3.7}$$

Where $W_{C,f}$ is the normalized weight fraction of C. The normalized weight fractions of Fe and Cr can be calculated in a similar manner.

The effective C weight fraction loss is calculated in Equation 3.8.

$$W_{C,loss} = W_{C,CCO} - W_{C,f} \tag{3.8}$$

Where $W_{C,loss}$ is the total C loss based on the amount of LAFs in the overlay.

Chapter 4

Growth Mechanism of Primary Chromium Carbide Needles during Solidification

4.1 Introduction

The Fe-Cr-C system with primary carbide solidification is the foundation of one of the most widely used wear-protection technologies: the chromium carbide overlays (CCOs). This technology is employed in mining, construction equipment, agriculture, and in oil-sands processing applications [1, 3]. Despite its ubiquitousness and current relevance in industry, this material system has received relatively little attention from the scientific community until recently, with only the crystallography of carbides [17–21] understood at a fundamental level. One of the important gaps in knowledge is the understanding of nucleation and growth mechanisms of primary carbide needles, since they determine the final microstructure and performance of the material. This paper addresses on the growth aspect.

The stages of growth of chromium carbide needles have been discussed by previous researchers [53–56], including recent work using confocal scanning laser microscopy (CSLM) [57]. The observations indicate that the facets and the tip of the needle have

different mechanisms of growth, with the tip growing fast, likely controlled by diffusion and the sides growing slowly in a faceted manner, likely controlled by interfacial kinetics.

The growth mechanism of carbide needles is not captured in existing models of needle growth such as those by Ivantsov [58], Horvay and Cahn [59], Trivedi [60], and Castillo *et al.* [61]. These models aimed at capturing dendritic solidification, and consider needles that grow by diffusion over their whole surface, not just the tip. The resulting needle shape in these models is that of a paraboloid of revolution, which is representative of dendrite tips, but not representative of needles of chromium carbide and other similar material systems.

The original theory of steady state diffusion-controlled needle growth proposed by Zener [62] considered the general diffusion equation describing diffusion-controlled lengthening of a needle without committing to an exact diffusion profile surrounding the needle, and most subsequent theories of lengthening are refinements over this concept. Hillert [63] found Zener's model to be inaccurate for high supersaturations and developed a modified model referred to in literature as the Zener-Hillert model [64–67]. Hillert also created a model specifically describing needle growth by solving the two-dimensional diffusion equation in cylindrical coordinates and considers diffusion-controlled growth across all needle surfaces. The Hillert model for needle growth in cylindrical coordinates, as well as his extension of Zener's analysis are derived based on a two dimensional diffusion field, where the boundary conditions are not compatible with a steady state solution. Ivantsov's needle growth model represents a natural extension of Hillert's needle growth analysis in a cylindrical coordinate frame.

The specific case of growth of faceted needles was investigated by Amar *et al.* [68]. Their investigation was focused on NH_4Br crystals growing in water. The crystals exhibited dendritic shape at high growth velocities (0.43 μm/s) and became faceted needles at slow growth velocities (0.015 μm/s). They applied Ivantsov's diffusion-limited growth

theory with an additional factor to account for the shape of the facet based on the interface temperature, but keeping the assumption of diffusion-dominated growth over all the needle surface. A general analysis of faceted growth mechanisms is provided by West *et al.* [69], who discuss general mechanisms that rely on specific knowledge of the facet's crystallographic direction for inferring surface energy. The growth rate of a specific facet can then be calculated based the specific surface energy, the free energy, and the molar volume. The growth of faceted needles is not directly addressed in this work.

Debierre *et al.* [70] developed a phase-field solidification simulation for faceted structures. Their model is based on the assumption that diffusivity in the solid is the same as in the liquid, and the shape of the needle is parabolic; these hypotheses are not well suited to the Fe-Cr-C system, where the diffusivity in the solid is negligible, while the shape of the needles is not parabolic.

The work described here is the first attempt at predicting the rate of growth of primary carbide needles in the Fe-Cr-C alloy accounting for mixed growth mechanisms and faceted geometry. In addition to the theory, the growth of carbides was observed in-situ using CLSM. Nucleation aspects are outside the scope of this work.

4.2 Materials System

The material system considered (CCOs) consists of weld-deposited overlays based on the Fe-Cr-C ternary system, with high overall fractions of chromium (typically 8-35 wt%) and carbon (2-9 wt%). Their composition is typically achieved by mixing powders rich in iron, chromium, carbon (e.g. "ferro-chrome"), and other alloying elements.

The focus of this work is hypereutectic CCOs, which are the most wear resistant and are widely used in industry. The liquidus surface of the pure Fe-Cr-C ternary system is illustrated in Figure 4.1. In this figure C_0 indicates a typical hypereutectic composition.

The monovariant eutectic reaction predicted here is not commonly observed in CCOs in practice. Hypereutectic CCOs solidify with primary carbide needles, which are harder than the surrounding eutectic [22]; therefore higher fraction of needles typically resulting in better wear performance [15, 28].

The primary needles have the stoichiometric composition of M_7C_3, where M is mostly Cr, with smaller amounts of Fe and other alloying elements. These primary needles typically have an hexagonal cross section with a thin austenite core running along the centre of the rods [41–43]. The eutectic surrounding the needles is a combination of austenite and M_7C_3 carbide formed from the remaining liquid [25].

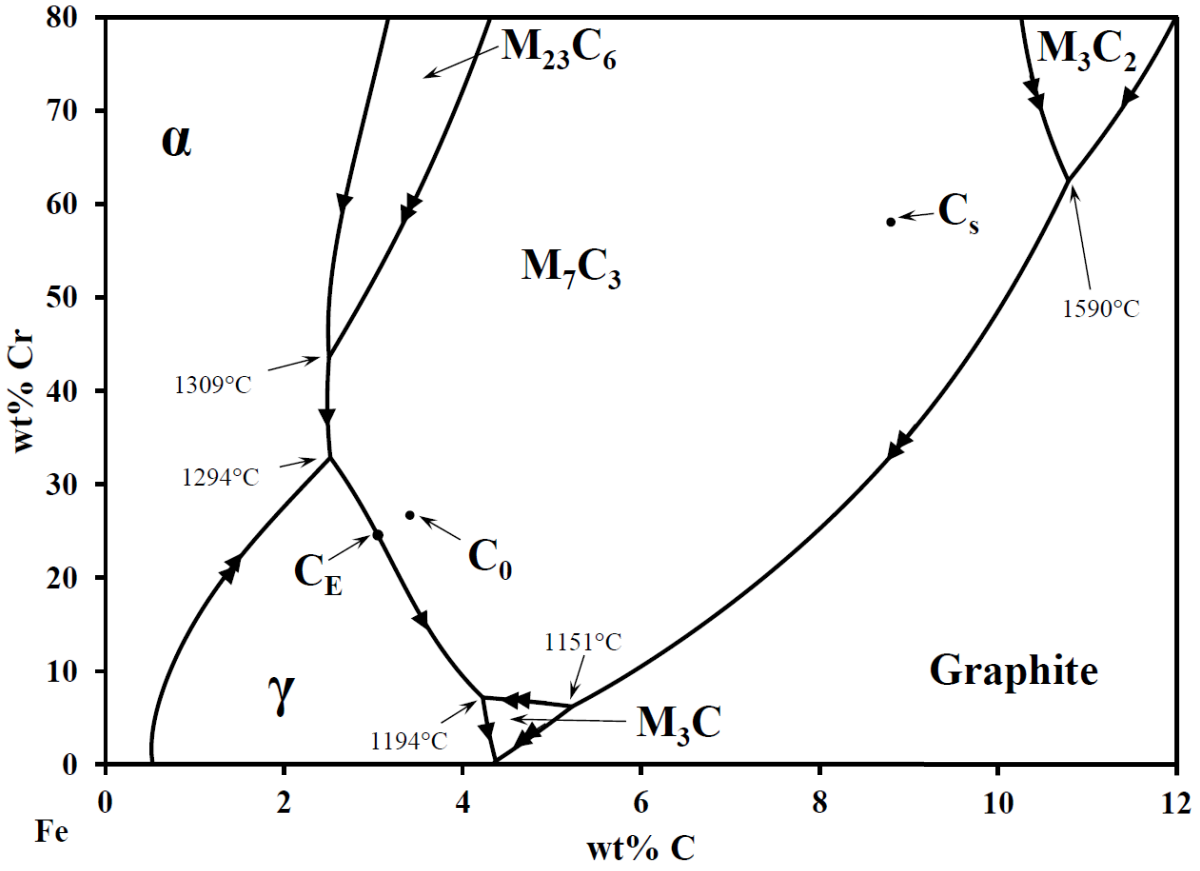

Figure 4.1: Liquidus projection of Fe-Cr-C ternary phase diagram in the region of relevance to CCOs. [51]

4.3 Analysis of Needle Growth

4.3.1 Longitudinal Growth

The analysis of diffusion-controlled growth will be treated in a general way based on the diffusion of the slowest component, with the understanding that the focus of this paper is on chromium carbide M_7C_3 needles, in which chromium is the rate-limiting component. This analysis should be applicable to other systems fulfilling the same basic principles.

As a model system, consider an alloy of original composition C_0, which has a solidification mode of primary needles of constant stoichiometric composition C_s, which are in equilibrium with a liquid of composition $C_E < C_0 << C_s$, as considered by previous models [62, 63, 65].

For CCOs, the outer needle faces are typically faceted, suggesting an interface controlled growth. The experiments performed indicated that the thickening of needles by facet growth is much slower (of the order of two orders of magnitude) than the growth of the needle tip, supporting the hypothesis of interface controlled growth. Regardless the mechanism of facet growth, the model developed here is valid for all cases in which the tip grows by diffusion and the thickening of needles is much slower than longitudinal growth, thus decoupling the two growth mechanisms.

Figure 4.2 illustrates the tip of a carbide needle and its surrounding diffusion field. In this figure, r_0 is the radius of the needle, x is the coordinate in the direction of growth of the needle, y and z are the other orthogonal space coordinates, $r' = \sqrt{y^2 + z^2}$ is a radius in cylindrical coordinates, and $r = \sqrt{x^2 + y^2 + z^2}$ is the radial coordinate in spherical coordinates. Coordinates x, y, and z constitute an Eulerian coordinate frame fixed to the advancing tip of the needle at velocity, U, similar to previous models that affixed the coordinate frame to the needle tip [62, 63, 71]. The magnitude r_d is the characteristic length of the diffusion field.

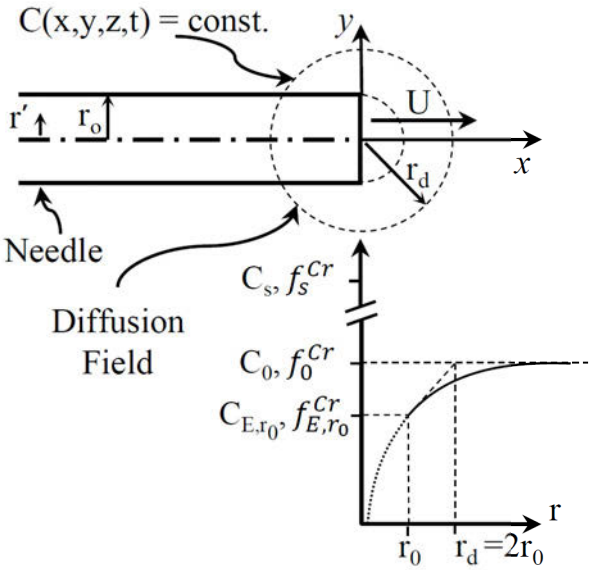

Figure 4.2: Diffusion field for the growth of a needle with negligible thickening.

For the case of chromium carbide needles, the rate controlling step for diffusion growth is the diffusion of Cr; C has a much higher diffusivity [72], and concentration of C will be considered uniform during the needle growth process. The diffusion field at the needle-tip is governed by:

$$\frac{\partial C}{\partial t} = \nabla(D\nabla C) + U\frac{\partial C}{\partial x} \tag{4.1}$$

where C is the concentration of Cr (in kg/m^3). This equation allows for variable properties in space and time. For simplicity, the needle will be approximated by a thin cylinder with symmetry of revolution. The boundary conditions for this equation are:

$$x = 0, r' < r_0 \qquad C = C_E \qquad \text{needle tip} \tag{4.2}$$

$$r' = r_0, x < 0 \qquad \frac{\partial C}{\partial r'} = \frac{J}{D} \qquad \text{needle side} \tag{4.3}$$

$$r' \to \infty \qquad C = C_0 \qquad \text{melt far from needle} \tag{4.4}$$

where Equation 4.2 embodies the consideration that at the needle tip, interface kinetics at

the tip are much faster than diffusion in the melt, thus the interface is in local equilibrium. Other realistic approximations are applicable. The faceted sides of the needle exhibit a very slow growth, such that the small mass flux J, along the facets of the needles can be neglected, resulting in the condition $\partial C/\partial r' = 0$. The issue of incompatible boundary conditions encountered by Hillert's in his analysis [65] is not an obstacle in the present model.

The experiments performed show that advection is secondary. The Peclet number is a dimensionless group that captures the relevance of advection relative to diffusion, and for typical values of growth velocity U=5 μm/s, a diffusion radius of r_d=10 μm, and a diffusivity D=1.7 10^{-9} m^2/s at 1548 K, Pe= $Ur_d/(2D)$ =0.15<1, indicating that the effect of advection is small and the advective term can be neglected as a reasonable approximation in Equation 4.1. When diffusivity is constant in space, and the needle is thin with no advection, the solution to Equations 4.1-4.4 is [73–75]:

$$C(r,t) = C_0 - \frac{\dot{m}}{4\pi D r}\mathrm{erfc}\left(\frac{r}{\sqrt{4Dt}}\right) \tag{4.5}$$

where $\dot{m}$ is the mass flow rate of solute (Cr) in the melt towards the tip of the needle.

Equation 4.5 describes the growth of needles as a continuous point sink in which solute flows towards the tip. This equation predicts a rapid initial transient period followed by growth at a steady state. As is the case with the Zener model [62], the needle radius is assumed as constant throughout the growth. In the present model, the needle radius is assumed to be smaller than the size of the diffusion field ($r_o \ll r$) so the needle tip can be approximated as a point sink for solute.

Equation 4.5 does not account for the finite size of the carbide after nucleation and very early growth stage where the cross section of the needle is established. Accounting for this initial time by using $t+t_0$ instead of just t also prevents the unrealistic asymptotic

behavior of Equation 4.5 at early times. Analysis of stages of nucleation and early growth (to be published separately), suggests the needle starts to grow longitudinally after a time of the order of the time constant for diffusion to reach a distance r_0:

$$t_0 \approx \frac{r_0^2}{D} \tag{4.6}$$

All the variables from Equation 4.5 except mass flow rate of solute are known from thermodynamics and tabulated data. The mass flow rate of solute is the rate at which the solute is adsorbed onto the tip, resulting in growth of the needle. Mass flow rate can be related to the growth velocity through a mass balance, obtaining:

$$\dot{m} = UA_c\rho_s\left(f_s^{Cr} - \frac{f_s^{Fe}}{f_{E,r_0}^{Fe}} f_{E,r_0}^{Cr}\right) \tag{4.7}$$

where ρ_s is the density of the solid, f_s^{Cr} and f_{E,r_0}^{Cr} are the mass fraction of solute in the solid and the mass fraction of solute in the liquid in equilibrium with the solid, f_s^{Fe} and f_{E,r_0}^{Fe} (f_{E,r_0}^{Fe}=f_E^{Fe}) are the mass fraction of the primary matrix alloy (Fe for the case of CCOs) in the solid and liquid in equilibrium with the solid, and A_c is the cross sectional area of the carbide needles. Equation 4.7 also accounts for the change in molar volume between the liquid and solid; this effect is relatively small, and was neglected in the original Zener model [62] and subsequent Zener-Hillert model [63].

The effect of carbide thickness affects the thermodynamics at the interface, such that thinner carbides experience a decreased driving force for growth (Gibbs-Thomson effect). This effect can be captured by considering a critical carbide radius (r_c), for which the size effect matches the thermodynamic driving force, stalling growth [65]. The critical

carbide radius is defined as:

$$r_c = \frac{2\sigma V_{m,s}}{RT} \frac{f^{Cr}_{E,r_0}}{(f^{Cr}_0 - f^{Cr}_{E,r_0})} \tag{4.8}$$

where f^{Cr}_0 is the nominal mass fraction of solute in the melt, σ is the interfacial energy in J/m^2, $V_{m,s}$ is the molar volume of the needle, R is the ideal gas constant and T in this case is the equilibrium liquid temperature. In the experiments performed, r_c is of the order of 10 nm, much smaller than the needle radius ($r_0 \approx$5 μm), thus the effect of surface curvature is small.

Replacing mass flow rate of Equation 4.7 in Equation 4.5, accounting for the time t_0 involved in the nucleation and early growth stage, incorporating the Gibbs-Thomson effect as done by Zener [62], and approximating the carbide tip as hemispherical ($f^{Cr}(r_0)$=f^{Cr}_{E,r_0}), Equation 4.5 can be rewritten as:

$$U = \frac{4D\rho_l}{r_0\rho_s}\left(1 - \frac{r_c}{r_0}\right)\frac{\Delta f^*}{\mathrm{erfc}\left(\frac{r_o}{\sqrt{4D(t+t_0)}}\right)} \tag{4.9}$$

where ρ_l is the density of the liquid and Δf^* is defined as:

$$\Delta f^* = \frac{f^{Cr}_0 - f^{Cr}_{E,r_0}}{\left(f^{Cr}_s - \frac{f^{Fe}_s}{f^{Fe}_E} f^{Cr}_{E,r_0}\right)} \tag{4.10}$$

The term Δf^* is a dimensionless term describing the solute needed from the liquid to form the solid (comparable to supersaturation in Zener's model [62] with the added consideration of molar volume change). For comparison with experiments, only a half-space should be considered, since only needles at the surface of the melt are visible. For needles at the surface, the numerator on the right hand side of Equation 4.9 should be 2

instead of 4.

Equation 4.9 can also be expressed using the notation of Christian and others, where $\mathrm{Pe} = (U r_0) \,/\, (2D)$:

$$\mathrm{Pe} = \frac{2\rho_l}{\rho_s}\left(1 - \frac{r_c}{r_0}\right)\frac{\Delta f^*}{\mathrm{erfc}\left(\dfrac{r_0}{\sqrt{4D(t+t_0)}}\right)} \tag{4.11}$$

Equations 4.9 and 4.11 reach a steady state growth velocity at long enough times (the erfc function tends to 1). This steady-state solution has similar features to the Zener model [62], which expressed in the notation of this work corresponds to:

$$\mathrm{Pe} = \frac{1}{2\alpha}\left(1 - \frac{r_c}{r_0}\right)\frac{(f_0^{Cr} - f_{E,r_0}^{Cr})}{(f_s^{Cr} - f_{E,r_0}^{Cr})} \tag{4.12}$$

In Zener's analysis, the parameter α is an unspecified constant of the order of 1 (assumed as equal to 1 in Figure 4.5). The steady-state growth from Equation 4.11 can also be compared with the Zener-Hillert model:

$$\mathrm{Pe} = \frac{1}{4}\left(1 - \frac{r_c}{r_0}\right)\frac{(f_0^{Cr} - f_{E,r_0}^{Cr})}{(f_s^{Cr} - f_0^{Cr})} \tag{4.13}$$

It can be observed that in steady-state, the Zener-Hillert model gives predictions approximately 8 times smaller than the model presented here, reflecting the different mechanism of thickening of needles between the two models. The growth described by Equation 4.9 can slow down abruptly due to the soft impingement with other needles solidifying in the melt.

4.3.2 Soft Impingement

As the primary needles grow, and the volume fraction of needles increases, the probability that the diffusion field ahead at the tip of the needle impinges on another needle also

increases. The interference of the diffusion field depletes the solute ahead of the growing needle, slowing its growth. The interaction range for soft impingement is given by the characteristic length associated with diffusion. The final distance between needles at the end of solidification might be shorter, as the fraction of carbides increases during solidification, with the final fraction of needles governed by thermodynamics.

Soft impingement is noticeable when the tip of a growing needle becomes closer than the diffusion length [65, 76], of the order of r_d. The critical value of r_d is determined by the intercept of the tangent shown in Figure 4.2, corresponding to Equation 4.5. The size of the diffusion field predicted by the proposed growth model reaches a steady state value as $t \to \infty$. In steady state, the diffusion field has the following size:

$$r_d = r_0 + \frac{\Delta C}{\left.\frac{\partial \Delta C}{\partial r}\right|_{r_0}} = 2r_0 \tag{4.14}$$

where ΔC=$C_0 - C(r_0)$.

4.3.3 Transverse Growth

The thickening of the needles (transverse growth) along the prism faces of the faceted needles is much slower than the longitudinal growth; which is consistent with the elongated morphology of the solidified needles. Faceted surfaces typically exhibit growth that is dominated on interface kinetics over diffusion, and it is typically slow and linear. From Equation 4.7, the mass flux of solute flowing to the carbide facet ($\dot{m}''$) can be expressed as:

$$\dot{m}'' = U\rho_s\left(f_s^{Cr} - \frac{f_s^{Fe}}{f_{E,r_0}^{Fe}} f_{E,r_0}^{Cr}\right) \tag{4.15}$$

The composition of the melt along the length of the needle is approximately constant, with the exception of the small region near the tip (for a distance of the order of r_c),

where a composition gradient drives the longitudinal growth. The uniform thickness observed for each needle in this work and others [41] is consistent with the slow growth observed. The initial thickness of the needles seems to be set during the nucleation and early growth stage, and is the focus of studies to be published separately.

4.4 Materials Properties

The material studied is the same as in [5]. The composition was determined using inductively coupled plasma (ICP) mass spectrometry, and is listed in Table 4.1. The corresponding properties necessary for the model are listed in Table 4.2. The temperature considered for thermodynamic calculations is the begining of eutectic precipitation temperature, 1275°C (1548.15 K), obtained from Scheil solidification simulations using Thermo-Calc [51], represented in Figure 4.3. A similar thermodynamic analysis was performed assuming C as a fast diffusing element in the solid, and yielded nearly identical results; this is consistent with the stoichiometric composition of the needles. The concentration of Cr of the needles was analysed using Auger electron spectroscopy (AES) and was found to be of the order of 56.5 wt% [77] which matches closely to the calculated value through thermodynamics. The diffusivity for Cr in liquid Fe was calculated as $D = D_0 \exp\left(-Q/\left(RT\right)\right)$, and it was calculated at the temperatures measured in the experiments: 1499 K for 5CR_01_01, 1430 K for 5CR_01_02, 1430 K for 5CR_01_03, and 1441 K for 5CR_01_04.

Table 4.1: Chemical composition of the material in experiments. [5] (wt%, Fe balance)

Element	**Cr**	**C**	**Mn**	**Mo**	**B**	**P**	**Si**
amount	26.7	3.41	2.39	0.8	0.24	0.02	0.53

Table 4.2: Summary of model parameters corresponding to experiments.

Variable	Value	Units	Reference
$D_{o,Cr-Fe_{(l)}}$	1.85 $\times 10^{-7}$	m^2/s	Esin *et al.* [72]
Q	60.5	kJ/mol	Esin *et al.* [72]
$f_{Cr,0}$	0.267	wt%	ICP Analysis
f_{Cr,M_7C_3}	0.578	wt%	Thermo-Calc [51]
$f_{Cr,E}$	0.222	wt%	Thermo-Calc [51]
f_{Fe,M_7C_3}	0.314	wt%	Thermo-Calc [51]
$f_{Fe,E}$	0.709	wt%	Thermo-Calc [51]
$\rho_{M_7C_3}$	6600	kg/m^3	Thermo-Calc [51]
ρ_l	6900	kg/m^3	Thermo-Calc [51]
$r_{0,5CR\_01\_01}$	12.5	μm	Observation
$r_{0,5CR\_01\_02}$	4	μm	Observation
$r_{0,5CR\_01\_03}$	5	μm	Observation
$r_{0,5CR\_01\_04}$	3	μm	Observation
σ	3.312	J/m^2	Liu *et al.* [78]
$V_{m,s}$	7.2×10^{-6}	mol/m^3	Thermo-Calc [51]

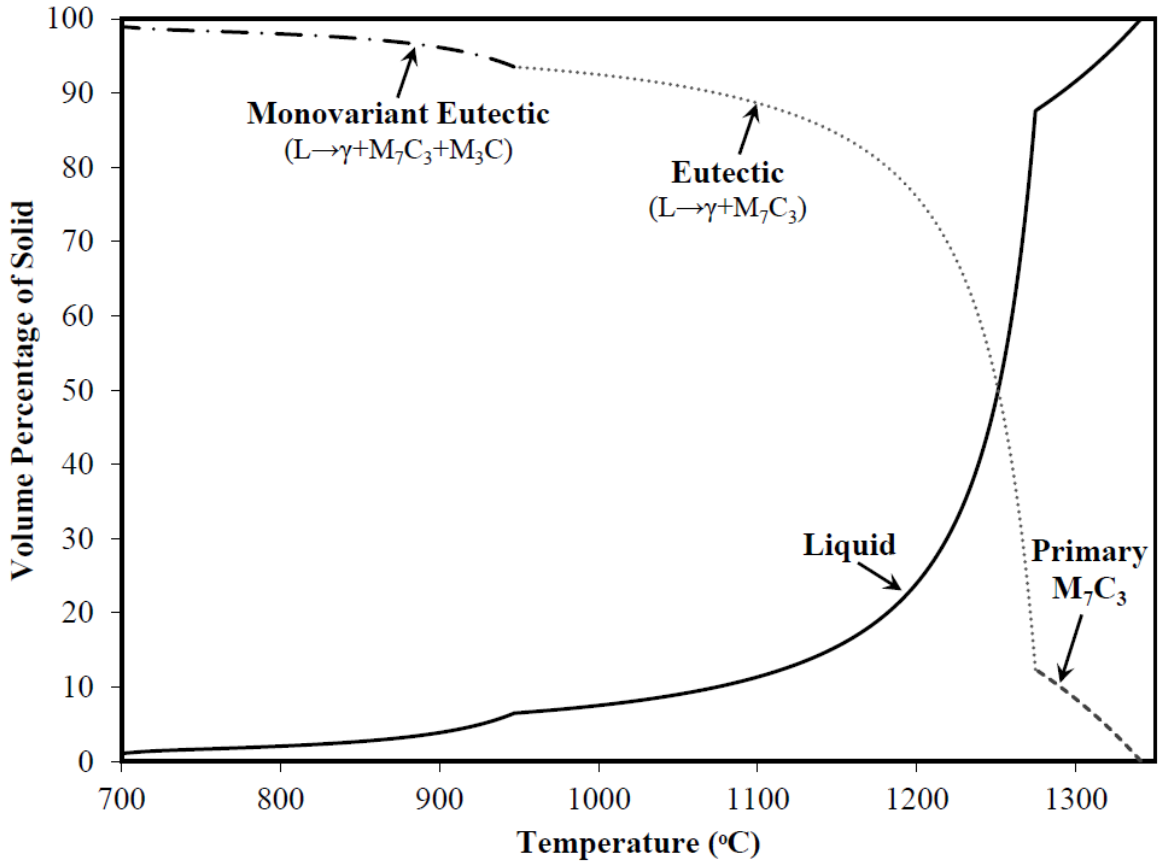

Figure 4.3: Scheil solidification for the material studied (Table 4.1).

4.5 In-situ Observations

The in-situ observations were performed with a Yonekura VL2000DX-SVF17SP CSLM located at University of Warwick. The initial sample consisted of a cube with a side of approximately 2 mm. The peak holding temperature was chosen as 1400°C to achieve complete melting (For the composition tested, Thermocals yields $T_{\text{liquidus}} = 1341$°C). The heating rate was not regulated, as complete melting was the goal of the heating cycle; the cooling rate was controlled at 5°C/s. The cooling rate was chosen to ensure that the solidification could be captured appropriately in terms of temporal resolution. A faster cooling rate of 30°C/s was originally attempted, corresponding to the actual cooling rate observed in SAW-deposited CCOs [5]. At this faster cooling the frame rate of the CSLM (10 frames per second) could not capture enough images during the growth of needles. A slower cooling rate (1°C/s) was also attempted, but no useful images were obtained for longitudinal growth.

The temperature readings shown in the videos were calibrated for higher accuracy. A linear calibration was performed between room temperature (measured accurately as 25°C) and the collapse of the sample into a droplet during heating, assumed to be the liquidus temperature (1341°C), but and reported as 1338°C by the CSLM thermocouple situated at the bottom of the sample). Temperature uniformity within the sample is of the order of 0.29 K, assessed using the gradient estimation of Gibbs *et al.* [79] assuming a sphere of radius 2 mm cooling at 5°C/s with a thermal conductivity approximated as that of white cast iron (37 W/m^{2}K) [80], and a specific heat of 460 J/kgK. During solidification, the appearance and growth of primary carbide needles surrounded by a liquid with limited amount of flow is observed. During the growth stage, the needles did not move with the flow, and seem to be attached under the surface, not merely floating.

A small amount of surface contaminants of unknown origin were observed floating

on the melt in many of the solidification videos. They appear at temperatures above the liquidus temperature and did not seem to affect the behavior of the carbides. There was no observed interaction between the surface contaminants and the carbides in the form of a reaction, or the appearance/disappearance of contaminants. Because of the very rough surface of the solidified sample, it was not possible to find and characterize the contaminants at after the solidification experiments. The peak holding temperature was increased to 1600°C in an attempt to dissolve the contaminants, but did not have an effect. The surface contaminants are likely oxides (potentially aluminium oxides) present in the overlay prior to entering the CLSM. Analysis of the videos assumed that the contaminants are not relevant to the growth of primary carbide needles.

4.6 Results

The in-situ videos showed the growth of the primary carbide needles clearly at the surface of the melt. The relevant videos have been uploaded as supporting online material (SOM). Four carbides were selected from video SOM_1 (cooling rate of 5°C/s) to be representative of all carbides in the melt. The carbides are shown in Figure 4.4 at the frame where the r_0 value was measured. The measured radii of the individual carbides was estimated based on the portions of the carbides that were visible from the liquid, and are summarized in Table 4.2.

The longitudinal growth of the four carbides was manually tracked frame by frame, and the results are shown in Figure 4.5. The model predictions are overlayed onto the experimental measurements and show a good agreement between the model and the observations. The results of the models by Zener (Equation 4.12, assuming α=1) and Zener-Hillert (Equation 4.13) are also shown on the plots for comparison. Both models under predict the growth rate, consistently with the consideration of diffusion

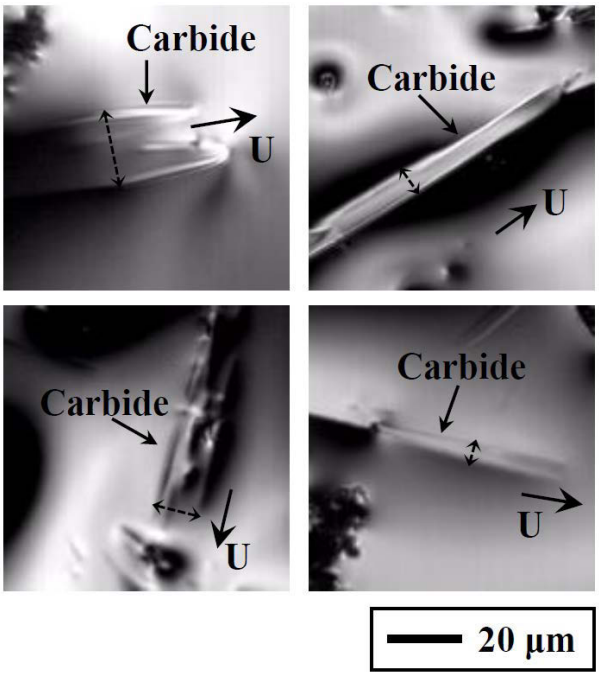

Figure 4.4: Representative images of the four carbides used to measure longitudinal growth, indicating the direction of growth velocity (U) and the needle thickness ($2r_0$). Top left: carbide 5CR_01_01 (r_0=12.5 μm). Top right: carbide 5CR_01_02 (r_0=4 μm). Bottom left: carbide 5CR_01_03 (r_0=5 μm). Bottom right: carbide 5CR_01_04 (r_0=3 μm).

mass transport over the whole length of the needle, instead of the most representative treatment done here of considering diffusion concentrated at the tip.

The undercooling for each of the carbides analysed in this work was taken as the difference between the equilibrium liquidus temperature calculated in Thermo-Calc [51] (1275°C) and the calibrated temperature at which the carbide was first observed, and is noted in Figure 4.5. The variation in melt temperature during the measured growth of carbides was of the order of 10°C to 50°C, increasing the undercooling. For the analytical solution proposed, it was assumed that the thermal undercooling stayed constant at the value where the carbide was first observed.

Figure 4.6 shows the four carbides from video SOM_1 at the point of impingement. Soft impingement here is defined as the moment where the diffusion field of another carbide was first observed to interact with the growing carbide. The black dotted circles in the figure indicate the diffusion field of the carbide (r_d) and the arrows represent the distance between the advancing interface and the impinging carbide.

The final microstructure of the sample from SOM_1 is shown in Figure 4.7, which corresponds to a vertical sectioning plane passing through the center of the sample. This image displays the typical microstructure observed in CCOs, with carbide needles surrounded by eutectic. The microstructure is uniform through the sample and does not show a preferential orientation, both features consistent with the high temperature homogeneity expected.The top of the image shows the surface profile, illustrating the high final roughness expected from the videos, and also showing evidence of solidification shrinkage near the surface.

The video in SOM_2 shows the outward growth of a carbide. This video corresponds to a cooling rate of 1°C/s, and it is the only video capture obtained that shows radial growth in a way that can be quantified. The evolution of thickness as a function of time is shown in Figure 4.8. It can be seen that the growth is approximately linear at an

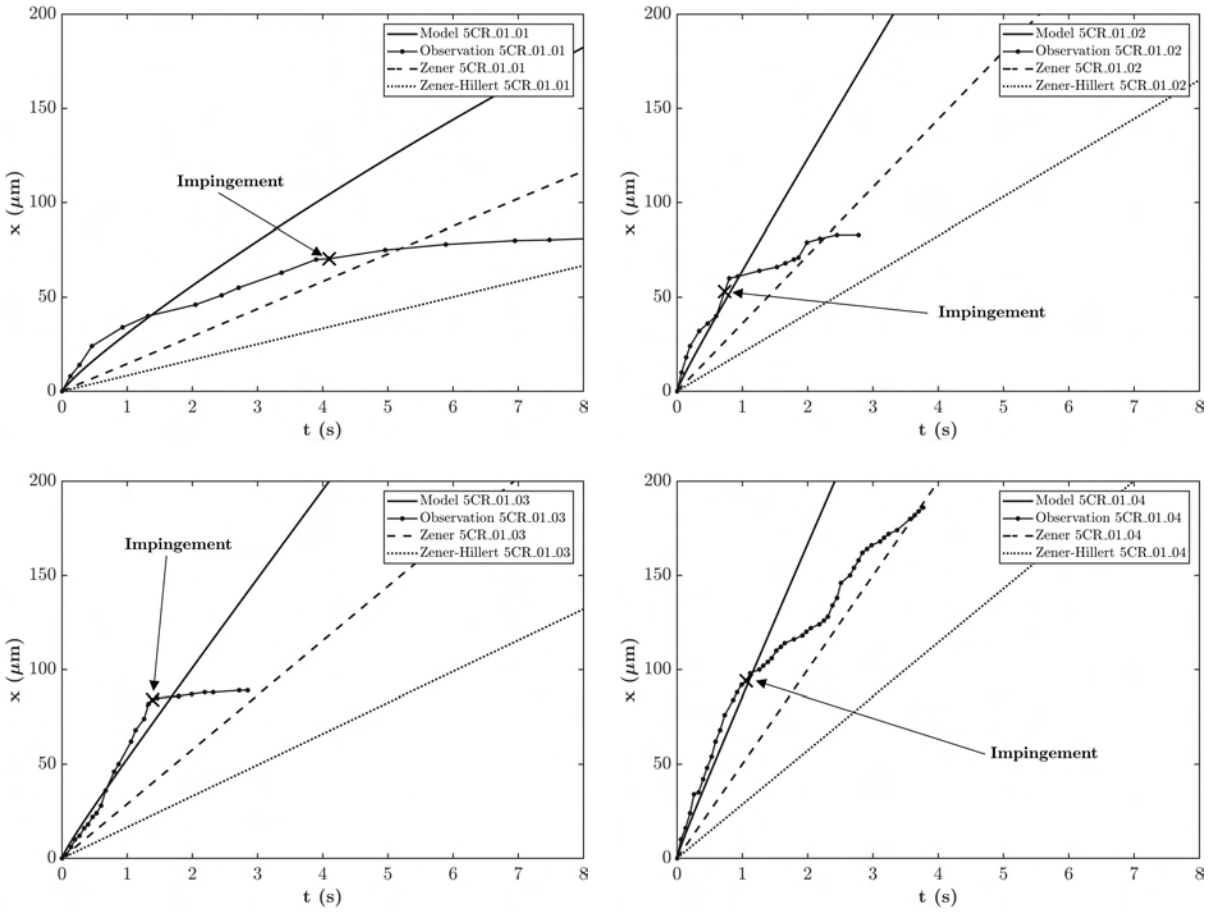

Figure 4.5: Longitudinal growth of carbides from video SOM_1 and the growth model predictions according to this work (Equation 4.9), Zener [62] (Equation 4.12), and Zener-Hillert [63] (Equation 4.13). The first appearance of carbides impinging along the path of growth is marked. Top left: carbide 5CR_01_01 (t=642.62 s, T=1499 K). Top right: carbide 5CR_01_02 (t=655.65 s, T=1430 K). Bottom left: carbide 5CR_01_03 (t=655.65 s, T=1430 K). Bottom right: carbide 5CR_01_04 (t=653.60 s, T=1441 K). Micrographs at the point of impingement are shown in Figure 4.6.

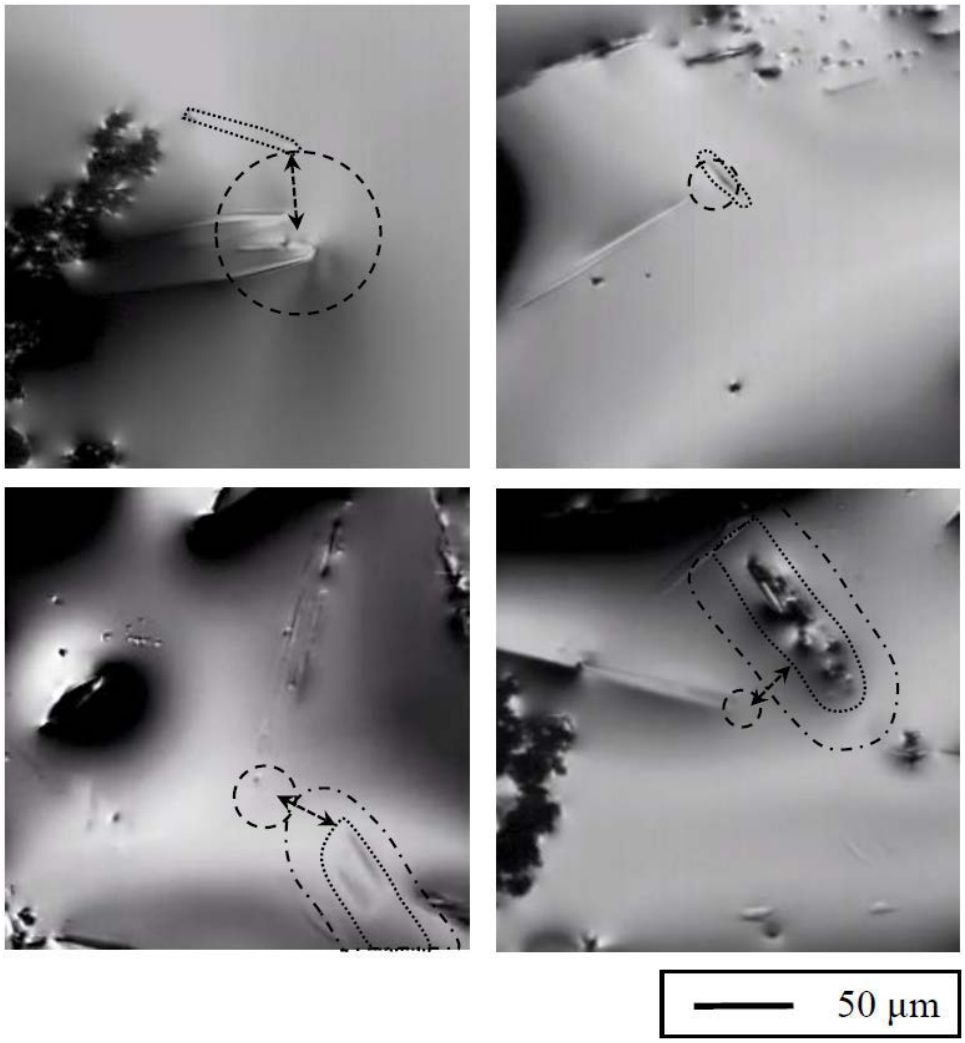

Figure 4.6: Moment of first observed impingement. Impinging carbides are outlined and r_d is represented by the dotted circles. The impingement distance is noted in the figure between the centre of the growing carbide and the impinging carbide. Top left: carbide 5CR_01_01 at t=646.72 s. Top right: carbide 5CR_01_02 at t=656.45 s. Bottom left: carbide 5CR_01_03 at t=657.04 s. Bottom right: carbide 5CR_01_04 at t=655.79 s.

Figure 4.7: Vertical cross-section of the sample from SOM_1. The top of the sample corresponds to the surface visualized in the CSLM.

average velocity of the order of 0.43 μm/s. Applying Equation 4.15, this growth rate corresponds to a mass flow of 270 kg/m^{2}s. The measured transverse growth velocity and mass flux are more than one order of magnitude slower than for the longitudinal growth. This negligible thickening of the needle is not captured adequately in pre-existent models developed for dendritic growth which consider thickening by diffusion.

Figure 4.8: Tracked growth of carbide 1CR_01_01 from SOM_2 exhibiting slow transverse growth direction. Image on the left at t=613.76 s and the image on the left at t=643.27 s.

4.7 Discussion

The diffusion-controlled growth model proposed shows good agreement with the in-situ observations performed, supporting the argument that the the interface-control mass transport mechanism on the side of faceted needles must be taken into account, and models of needle growth considering diffusion control over the whole length of the needle can result in significant error of prediction.

The model proposed addresses only the growth stage of the needles, but not its nucleation and early growth, which could not be captured in the videos. In particular, this model considers that the cross section of the needles is essentially set from the beginning. The size of the cross section of the needle (of the order of 5 μm), is too large to be determined by nucleation alone, and very likely, there is an early growth stage in which the thickness of the needle is established. The time constant postulated empirically in Equation 4.6 is consistent with diffusion-controlled growth in the thickness of the needle in the early stage of growth. Analysis of past experiments also suggests that the cross section of the needles depends strongly on the temperature of nucleation, with lower temperatures yielding thinner carbides. The stages of nucleation and early

growth are the focus of current research, and their understanding would be very useful to overcome the need of an empirical measure of cross section in the current model.

One possible early growth mechanism is that immediately after nucleation the carbide starts to grow as a sheet that curls into itself in one of the dimensions and stops growing in that direction once the curling completes a cycle. This speculated mechanism would have a time constant of the order observed, and would also yield light into the presence of the typical austenite core in the needles. Using Thermocalc to estimate the entropy of solidification of the carbides yields a ratio $\Delta S/R$=1.78 [81], which is intermediate between 1 (typical of rough interfaces) and 2 or 3 (typical of faceted interfaces) [82]. This intermediate value is also consistent with the faceted carbide/austenite interface of the outside of the needle, and the rough interface for the same phases in the core of the needle.

For a given cooling rate, nucleation will happen simultaneously with growth, with slower growth or faster cooling rates resulting in finer carbides. There is evidence about faster cooling rates result in finer carbides [1, 56], but this evidence is not conclusive [5]. Lowering the growth rate of carbides should also result in a higher fraction of finer carbides nucleated at lower temperatures. The work presented here suggests that slowing mass transport to the needle tip should result into finer final microstructures for a given a cooling rate. For example, alloying elements that lower the liquidus temperature would result in slower diffusion and help refine the final microstructure.

As the carbides observed are at the surface of the melt, the contribution of capillary effects must be addressed. Considering the interface energy of liquid iron in an inert gas atmosphere (of the order of 2 J/m^2) [83, 84] as an approximation of the chamber of the CSLM, Equation 4.8 indicates the surface capillarity effect would become relevant for carbides with a thickness of the order of 11 nm, much thinner than what was observed. The effect of surface diffusion and stoichiometry changes by evaporation at the surface

of the melt are assumed to be negligible for the needle thickness considered.

In the model proposed, it is assumed that the rate-limiting factor for mass transfer at the needle tip is the diffusion of Cr in the melt while C diffuses much faster. In multi-component systems, the mobility of C may be lower than considered in this work [85–87]. At the representative temperature of 1275 °C, the diffusivity of Cr in the melt was calculated as $1.682\,10^{-9}$ m^2/s, and the diffusivity of C as $1.13\,10^{-6}$ m^2/s [72]. For the purpose of the proposed growth model, the large difference between the diffusivity of Cr and C in Fe suggests that diffusion of Cr is likely to remain the rate limiting in all cases.

The consideration of impingement accounts for the arrest in growth observed, which is otherwise attributed to the slowing rate typical of parabolic growth in other diffusion-controlled growth mechanisms. The impingements noted in Figure 4.6 corresponds well to the theoretical predictions, but the impingement distance shows variations. For example, for carbides 5CR_01_03 and 5CR_01_04, the arrest in growth occurs at slightly longer distances than expected. A possible reason for this observation is depletion of Cr caused by unseen carbides existing under the surface.

The current model proposed was developed assuming that the needle cross section does not change significantly during the needle growth. This hypothesis is supported by the observations of needle thickening more than order of magnitude slower than the longitudinal growth. The growth model could be improved by considering the slow coarsening of the needles using the measured constant coarsening rate. This improvement would involve numerical analysis or a more complex analytical final expression, which are outside the scope of this work.

4.8 Conclusions

The growth of primary carbide needles in CCOs was quantified by direct observation for the first time. The mode of growth observed is consistent with that recent experiments [57] showing a carbide shell morphology instead of growth of a fully solid needle.

The measurements of growth rate are consistent with diffusion-controlled growth at the carbide tip and interface-controlled growth on the carbide side facets, where the mass flow to the facets is much smaller than to the tip.

A theory of carbide growth based on diffusion at the carbide tip was proposed for Fe-Cr-C alloys for the first time. It predicts a steady state carbide growth velocity given by Equation 4.9, which is consistent with the general approach of Zener [62], but differs in the final expression from Hillert [63] and Ivantsov [58] as they consider diffusion-controlled coarsening of the needles, while this work shows in the experiments and analysis that the rate of faceted needle thickening is very slow. The initial needle thickness of the carbide was assessed empirically from videos and seems to be determined during the nucleation and early growth stage. The lateral growth of the carbide had a velocity of 0.43 μm/s, corresponding to a mass flux of 270 kg/m^{2}s.

The growth of carbides was observed to stall when the carbide tip approached another carbide at distances of the order of a carbide diameter. This is consistent with a diffusion growth mechanism in which growth stalls in the presence of a field depleted of solute by a previous carbide.

The model proposed is the first step towards a quantitative understanding of microstructural development in this important class of alloys, and combined with an understanding of nucleation, it will allow for the prediction of microstructures of CCOs under a variety of practical conditions.

Acknowledgements

The authors would like to thank Samuel Wilkinson Steel, a division of Samuel, Son & Co., for providing funding, samples, and their technical expertise. This research was also funded in part by NSERC (CRDPJ 470231-14) and the AWS Foundation (UA2203790).

4.9 Appendix 4.1: Derivation of Equation 4.7

The mass flowrate defined in Equation 4.7 was defined as the rate at which the solute adsorption onto the cross-section of the faceted needle, resulting in a certain growth velocity. The derivation of this equation relies on defining the mass flowrate as solute needed for growth of the solid and the amount of solute in transformed liquid and accounting for the change in molar volume between the liquid and solid. The system is defined in Figure 4.9, where L is some volume of liquid and the carbide is growing at a velocity (U) with a certain cross-sectional area (A_c) and the alloy base (Fe) and the main alloying element (Cr and C) are adsorbing to A_c.

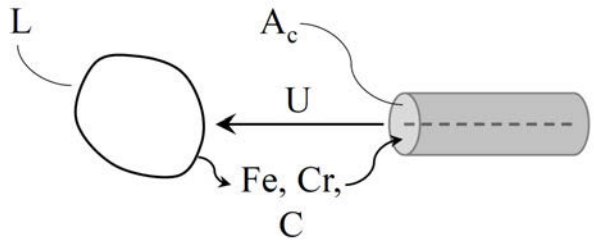

Figure 4.9: Schematic representation of the adsorption process.

The mass flowrate of the elements in the solid can be defined as:

$$Fe \qquad UA_c\rho_{Fe_s} \tag{4.16}$$

$$Cr \qquad UA_c\rho_{Cr_s} \tag{4.17}$$

$$C \qquad UA_c\rho_{C_s} \tag{4.18}$$

The same can be done for the liquid that is transformed to be incorporated into the solid (i.e. liquid in equilibrium with the solid). To account for the change in molar

volume it is necessary to define the alloying elements in terms of the base (Fe) as:

$$Fe \qquad UA_c\rho_{Fe_e} \tag{4.19}$$

$$Cr \qquad UA_c\frac{\rho_{Fe_s}}{\rho_{Fe_e}}\rho_{Cr_e} \tag{4.20}$$

$$C \qquad UA_c\frac{\rho_{Fe_s}}{\rho_{Fe_e}}\rho_{C_e} \tag{4.21}$$

The mass flowrate for the solute (Cr) can then be defined as:

$$\dot{m} = UA_c\rho_s\Bigg(\underbrace{\rho_{Cr,s}}_{\substack{\text{Cr needed}\\ \text{from melt}}} - \underbrace{\frac{\rho_{Fe,s}}{\rho_{Fe,E}}\rho_{Cr,E}}_{\substack{\text{Cr available in}\\ \text{transformed liquid}}}\Bigg)$$

Defining it in terms of mass fractions:

$$\dot{m} = UA_c\rho_s\left(f_{Cr,s} - \frac{f_{Fe,s}}{f_{Fe,E}}f_{Cr,E}\right) \tag{4.22}$$

4.10 Appendix 4.2: Calculation of Dimensionless Entropy of Formation for the Primary Carbides

The dimensionless entropy (α_f) of formation provides an indicator of faceted (α_f=2∼3) or non-faceted (α_f=1) growth [88]. The enthalpy of formation (ΔH_f) can be calculated from Thermo-Clac and is seen in Figure 4.10.

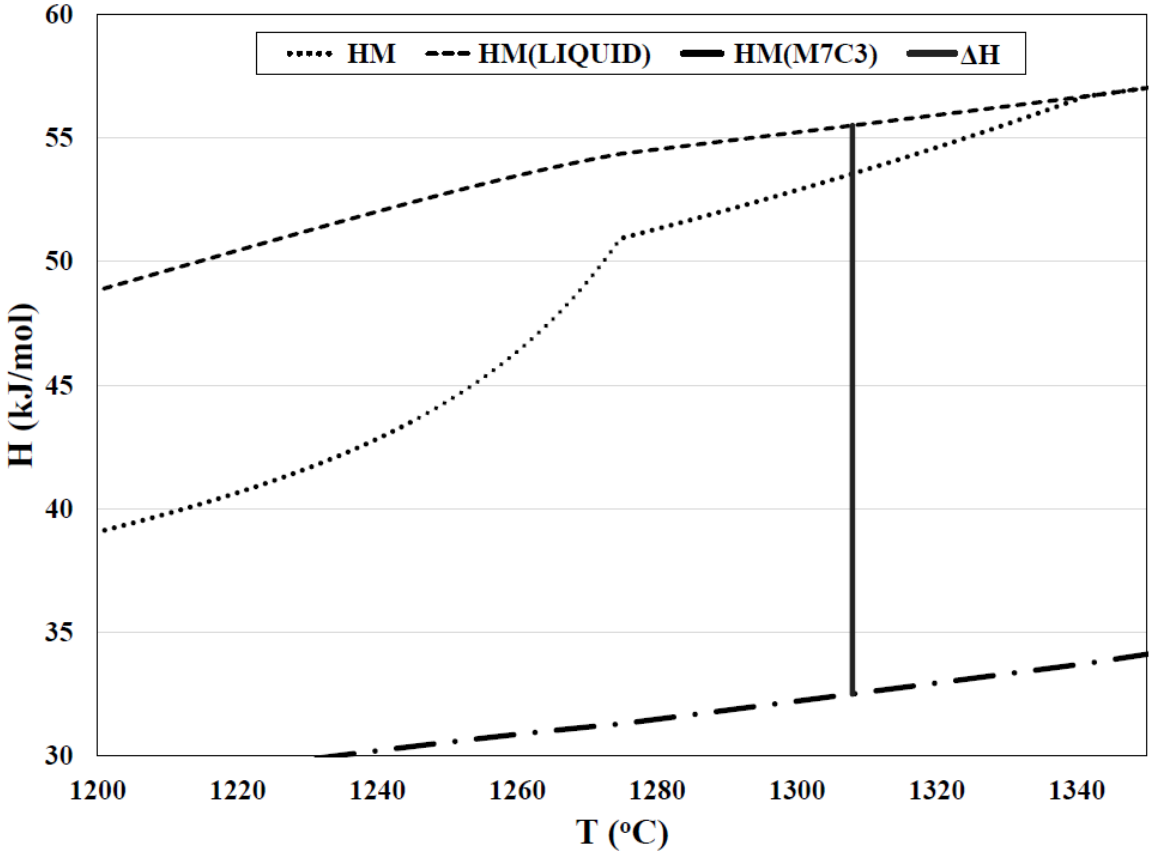

Figure 4.10: Enthalpy of formation for the primary M_7C_3 carbides. [51]

Based on the enthalpy of formation at an average temperature of 1307°C (1581 K),

the dimensionless entropy of formation, defined as:

$$\alpha_f = \frac{\Delta S_f}{R} \tag{4.23}$$

where ΔS_f is the entropy of formation. The value of α_f calculated for the primary carbides is $\sim$1.78 indicating that faceted and non-faceted growth are possible, but faceted is likely.

4.11 Appendix 4.3: Composition Sensitivity Analysis of Growth Model

The model developed to describe the growth of primary chromium carbide needles, considering the half-space assumption associated with carbides at the surface of the melt, is defined by

$$U = \frac{2D\rho_l}{r_o\rho_s} \frac{M_f}{\text{erfc}\left(\frac{r_o}{\sqrt{4D(t+t_o)}}\right)} \tag{4.24}$$

and the M_f term is defined as

$$M_f = \frac{f_{sol,\infty} - f_{sol,E}}{\left(f_{sol,s} - \frac{f_{base,s}}{f_{base,E}} f_{sol,E}\right)} \tag{4.25}$$

The model was found to be sensitive to the nominal composition of the overlay as the factor relating to the amount of solute needed from the melt for growth, M_f, is predicted through thermodynamic calculations in Thermo-Calc. The equilibrium compositions of primary carbide vary with small changes of the nominal composition. Accurate measurement of the composition of the overlay is necessary to apply the model.

A summary of the variation of parameters necessary for the calculation of Equation 4.24 as they vary with the nominal composition of the overlay ($f_{C,0}$ and $f_{Cr,0}$) is shown in Table 4.3.

It can be seen from Table 4.3 that as $f_{C,0}$ increases, $f_{Cr,E}$ and f_{Cr,M_7C_3} are decreased and $f_{Fe,E}$ and f_{Fe,M_7C_3} are both increased. Decreasing $f_{Cr,0}$ has the same effects. The alloy composition alters the Cr:Fe ratio in the liquid in equilibrium with the solid and by consequence the composition of the solid. The altered compositions have a large effect on the growth rate predicted by Equation 4.24. Increases to the C concentration and

Table 4.3: Variation in relevant parameters from Equation 4.24 with composition.

Variable	Alloy 1	Alloy 2	Alloy 4
$f_{C,0}$	0.0341	0.036	0.0341
$f_{Cr,0}$	0.267	0.267	0.25
$f_{Cr,E}$	0.222	0.213	0.21
$f_{Fe,E}$	0.709	0.717	0.721
f_{Cr,M_7C_3}	0.578	0.567	0.562
f_{Fe,M_7C_3}	0.314	0.324	0.33
T (^{o}C)	1275	1272	1272

decreases to the Cr concentration both result in increasing the predicted growth rate. The measured growth rates compared to the model predictions for the Fe-26 wt%Cr-3.41 wt%C are shown in Figure 4.11.

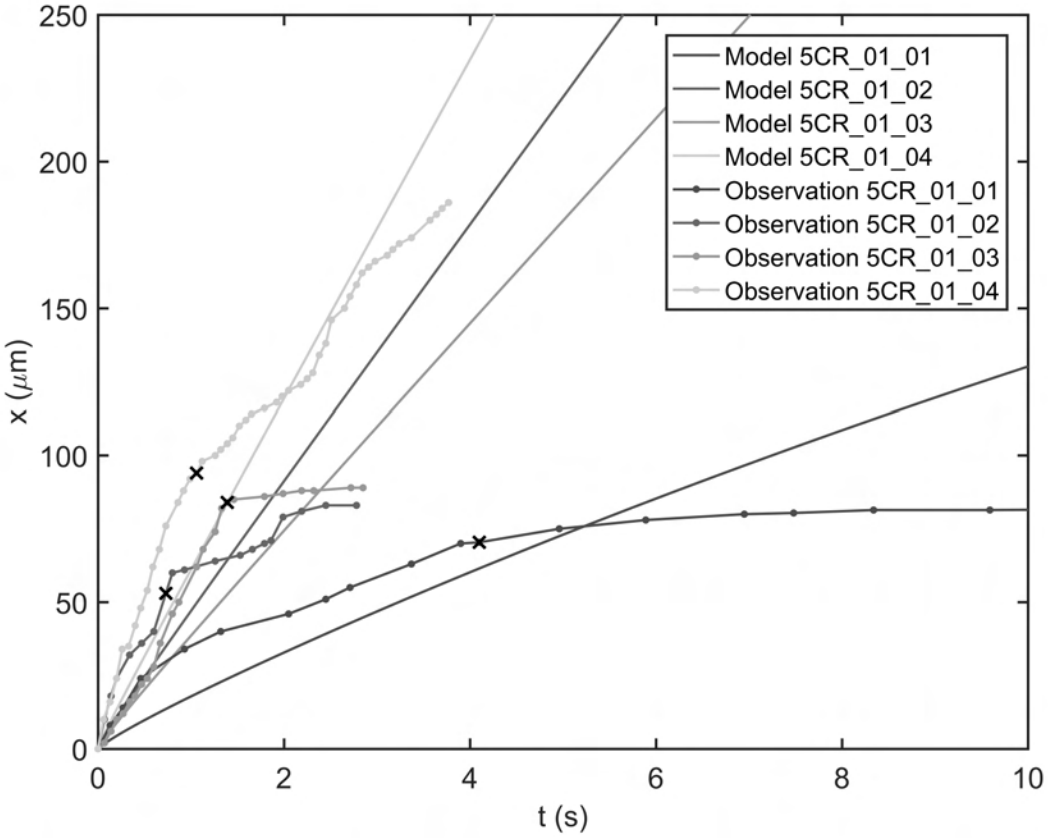

Figure 4.11: Comparison between observed growth for four carbides from video SOM_1 and the growth model predictions for the measured alloy composition of Fe-26 wt%Cr-3.41 wt%C. The first appearance of carbides impinging along the path of growth is marked on the plot by black crosses.

For comparison, the growth model for the Fe-26 wt%Cr-3.7 wt%C is shown in Figure 4.12. The increased predicted growth rate of the carbides is significant and reinforces the importance of composition for the growth model.

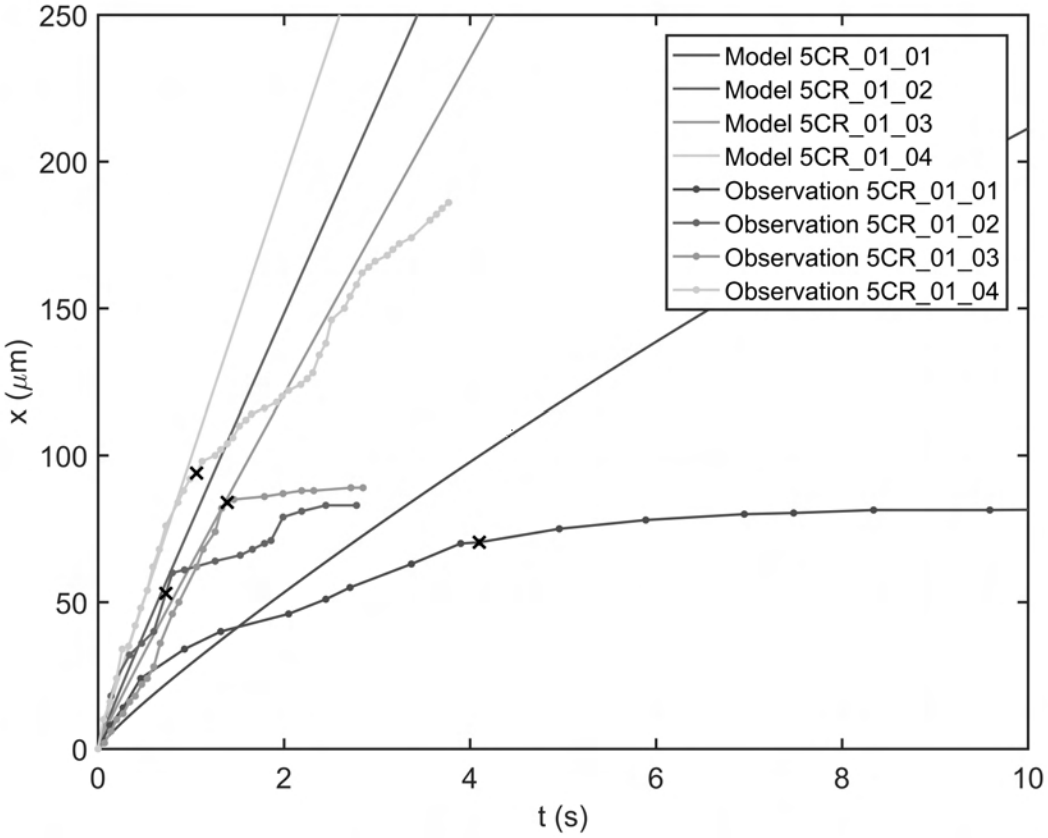

Figure 4.12: Comparison between observed growth for four carbides from video SOM_1 and the growth model predictions for the measured alloy composition of Fe-26 wt%Cr-3.7 wt%C. The first appearance of carbides impinging along the path of growth is marked on the plot by black crosses.

Chapter 5

Effect of Cooling Rate on Chromium Carbide Weld Overlays

5.1 Introduction

Wear and corrosion resistant overlays are used to prolong the lifetime of large scale components. By providing a wear resistant surface for a tough base material, overlays can help achieve an excellent balance of properties. Chromium carbide weld overlays (CCOs) play a major role in oil-sands, mining, agriculture, and processing applications, particularly where production reliability is important. [3,40] CCOs are typically deposited with welding processes such as submerged arc welding (SAW) and flux-cored arc welding (FCAW) due to their high productivity. [1, 3]

CCOs are weld-deposited overlays based on the Fe-Cr-C ternary system, with high overall fractions of chromium (typically 8-35 wt%) and carbon (2-9 wt%). CCOs with a primary M_7C_3 carbide solidification path typically exhibit better wear resistance, due to the high volume fractions of primary carbides with a high hardness as compared to the surrounding matrix. [15, 22, 28] The primary carbides have the nominal stoichiometric composition of M_7C_3, where M is mostly Cr, with smaller amounts of Fe and other alloying elements. The primary M_7C_3 carbides are the first microstructural feature to

solidify, and they have the morphology of a rod with a hexagonal cross section, often with a thin austenite core running along the centre of the rods. [41–43] The primary carbide rods are surrounded by a eutectic combination of austenite and M_7C_3 carbide forming from the remaining liquid. [25]

The effect of cooling rate on the microstructure of chromium carbide overlays (CCOs), particularly how it influences the primary M_7C_3 carbide morphology, is not well understood in literature. Increasing the cooling rate generally has the effect of refining the microstructure in most alloys [89]. It has been hypothesized that fast cooling rates will result in a reduction of carbide rod diameter [1], but a systematic and quantitative study has yet to be published in the scientific literature.

The study by Wang *et al.* [90] provides preliminary evidence of refinement with increasing cooling rate. Their study involved producing welds for four distinct Cr:C ratios on a substrate under three cooling conditions: 1) water cooling in direct contact with the substrate, 2) air cooling, and 3) a 250°C preheat followed by natural air cooling. The results of their study present microstructural images under each cooling condition from which a general trend can be inferred, but no quantitative data of primary carbide size from across the overlay cross section is provided. Given the high variability of CCO microstructure across an overlay cross-section, extrapolating the results to the rest of the microstructure can be inaccurate and warrants further investigation. The conclusions drawn from their work provide the first step towards proving a distinct relationship between cooling rate and primary carbide refinement. Of the Cr:C ratios used in their study, Alloy 2 (Cr:C ratio of 9.12) and Alloy 3 (Cr:C ratio of 6.55) most closely represent relevant CCO chemistries.

Hornung *et al.* [91] performed experiments showing limited evidence of the effect that cooling rate has on the microstructure by measuring the wear rate to find that as cooling rate is increased the wear resistance of the alloy decreased. Their study has a significant

volume fraction of unmelted particles that alter the alloy composition by decreasing the solute available for primary carbide formation [77]. The evidence of microstructural refinement is not the main focus of their study. A study of CCOs using widely different processes and cooling rates [5] suggested that cooling rate would have a significant effect on carbide thickness, contradicting Wang *et al.*These contrary findings increase the need for a quantitative study that isolates the effect of cooling rate on carbide refinement.

The work by Borle [5,45] consisted of three distinct experiments: 1) depositing CCOs with different welding processes with widely varying cooling rates, 2) testing the effect of preheat on the microstructure of CCOs, and 3) varying the AC balance in SAW to determine the effect. In the varied process study by Borle [5], CCOs were deposited with SAW, gas metal arc welding (GMAW), laser beam welding (LBW), and plasma transferred arc welding (PTAW) to measure the variation in primary M_7C_3 carbide size with different heat inputs and cooling rates. The results of these tests are shown in Figure 5.1, but did not prove conclusive, as the wide variation between the processes does not allow for isolation of just the cooling rate effect.

Additional analysis was also performed to study the effect of cooling rate through different preheats by measuring the average primary carbide size. The results of the preheat testing are shown in Table 5.1. These results found no correlation between the cooling rate and primary carbide size. The study was inconclusive as to the effect of cooling rate on primary carbide size as there was low a volume fraction of primary carbides on which to base the size analysis for all samples.

Attempting to vary cooling rate by altering the AC balance in SAW had similar issues to the preheat tests, as the fraction of primary carbide was too low to draw meaningful conclusions. Although the effect of altering the primary carbide side was not the primary purpose of the study, it yielded a average decrease in the carbide size with increasing balance. As balance decreases in AC SAW and there is more time spent in the electrode

negative (EN) polarity cycle, the energy balance of welding shifts from the bead towards the electrode, giving a colder weld pool. The results of the testing are shown in Figure 5.2.

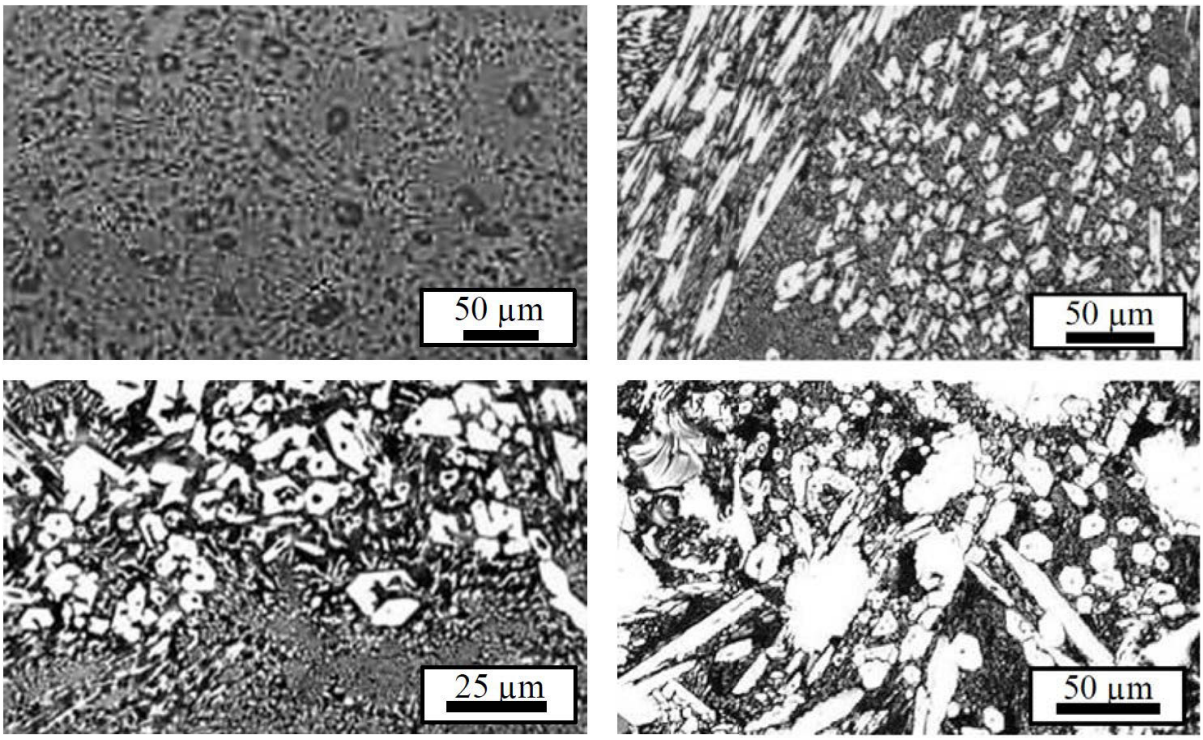

Figure 5.1: CCOs produced using various welding processes. Top left: CCO produced using the SAW process. Top right: Cored CCO welding wire electrode deposited using the GMAW process. Bottom left: LBW deposited CCO. Bottom right: CCO deposited using PTAW. [5]

Table 5.1: Effect of preheat on average primary carbide size. [5]

Preheat °K	**Total VF Carbide %**	**VF Primary %**	**Average Primary Size μm**	**Dilution %**
298	26.99	1.69	389	27
323	23.59	1.84	427	25
373	25.35	5.02	542	26
423	19.89	0.66	252	25

Given the contrary findings of literature studies regarding the refinement of primary carbides through cooling rate, the aim of this work is to provide conclusive quantitative size analysis of microstructure from controlled cooling rate experiments. This work aims

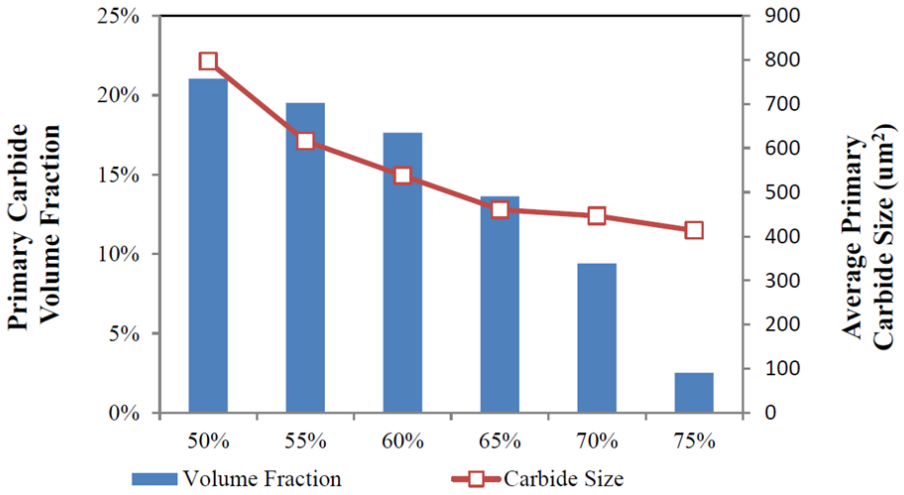

Figure 5.2: Effect of varying balance in AC SAW. [45]

to isolate the cooling rate effect and provide systematic and quantitative measurements representing the average carbide size across a sample.

5.2 Experimental Method

A cooled substrate was developed to enable variation of the cooling cycle of experimental CCOs melts. The substrate consists of a plate affixed to a polymer base through which water is fed into a basin and flows directly in contact with the base of the welding substrate. The design of the substrate allows for an interchangeable plate and for variation of the flowrate of water through the system to alter the cooling rate. The substrate is shown in Figure 5.3. The substrate was designed considering a copper plate where there is no dilution, but for the purpose of altering cooling rate, a steel substrate was chosen. The steel substrate avoids the contact barrier associated with the copper plate, allowing for increased control over cooling rate while maintaining negligible dilution. The use of type K grounded probe thermocouples at the inlet and outlet of the substrate allow the measurement of the total heat removed by the water, which is flowrate dependant. The

inlet thermocouple is not shown in Figure 5.3 as it was placed after the flowmeter to avoid back-heating during welding. Using this cooled substrate, the cooling rate effect can be isolated, and its effect on primary carbide size can be determined.

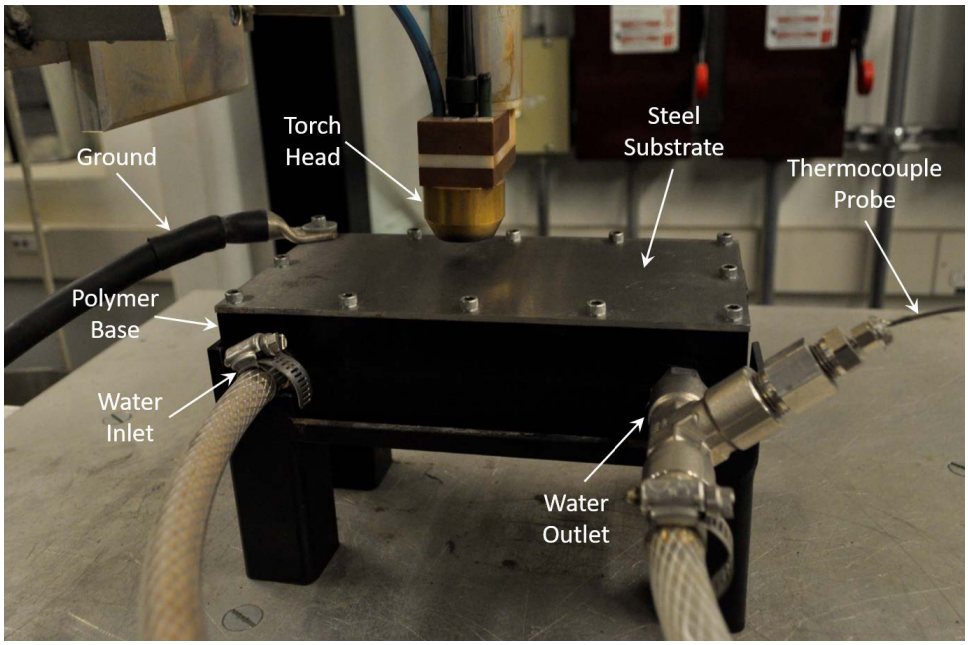

Figure 5.3: Thermally controlled substrate with steel plate.

CCOs are generally produced using high efficiency welding processes to maximize deposition. Typically, these highly efficient processes are susceptible to high levels of dilution. A low level of dilution is desirable for the cooling rate experiments, as high dilution welds significantly alter the chemistry of the weld with the incorporation of the substrate material, which introduces an undesired variable. To minimize dilution, PTAW was selected for deposition of the CCOs. PTAW is specifically designed for overlay production and is known for having very low dilution (<10%) [3]. A schematic of the PTAW process is shown in Figure 5.4. The PTAW setup used in the experiments in this work is a 400A custom Plasmastar PTAW. As PTAW uses a powder feed, the chemistry of all welds can be carefully controlled and maintained.

The experimental cooling rate of the welds was measured using a FLIR A6752sc

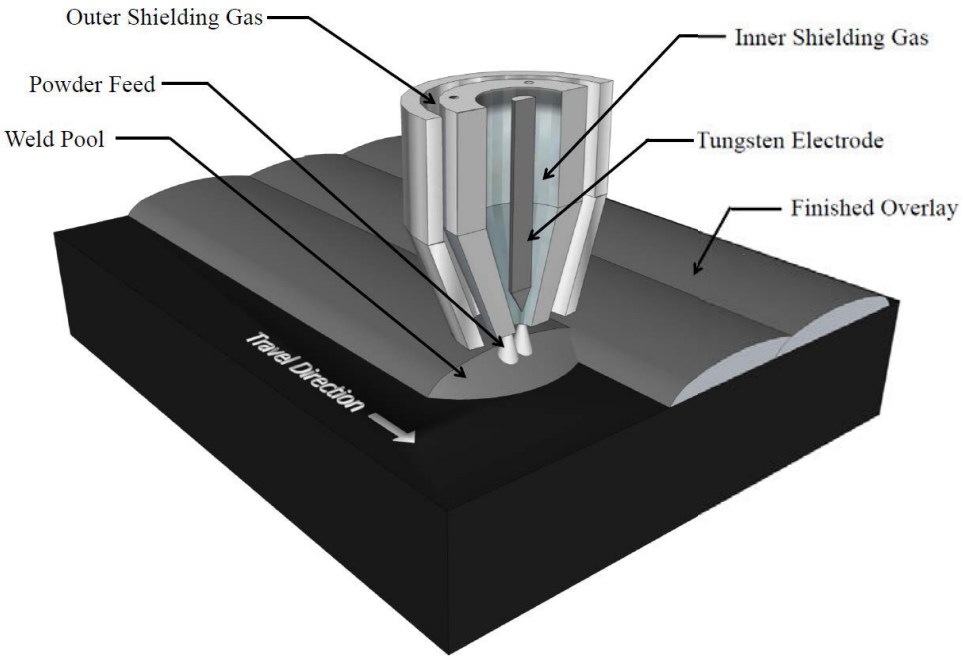

Figure 5.4: Schematic of the PTAW process.

thermal camera with a neutral density (ND2) filter to block out the intensity of the arc. The thermal camera was aligned perpendicular to the weld travel direction to visualize the weld. The PTAW torch is stationary throughout the welding process which allows the thermal camera to focus on the weld pool and solidifying bead. The inlet and outlet thermocouples were used to ensure that a steady steady temperature profile was established. The inlet and outlet thermocouples also allow for calculation of the total heat removed during welding, but do not allow for calculation of the cooling rate of the overlay. Direct measurement of the cooling rate by plunging thermocouple probes into the weld is difficult for a rapid freezing process such as PTAW and unreliable, as melting the end of the probe so that the internal wires no longer contact invalidates the results. Applying a thermocouple to the underside of the welding substrate is equally problematic, as probe thermocouple cannot be spot welded. Although wire thermocouples can be directly welded to the underside of the plate, they are not grounded and the proximity

to the arc causes electromagnetic interference, nullifying the results.

Two sets of welds were completed: one near the minimum flowrate of the system and one at the maximum flowrate. The absolute minimum flowrate of the system is not sufficient to prevent damage to the substrate for the parameters necessary to generate a meaningful overlay. The heat input of both welds was the same and was chosen based on a parametrization study of CCOs produced using PTAW. The parameters for the tests are shown in Table 5.2. All tests were completed with a 6 mm torch head to workpiece distance and with the tip of the electrode recessed 2 mm into the torch vertically. A 3.2 mm tungsten electrode with a 60° tip angle was used for all experiments and was ground between runs. The flowrates of the inner shielding gas (plasma gas), the powder feed gas, and the outer shielding gas were 2.5 L/min, 3.0 L/min, and 10 L/min respectively. The thickness of the substrate was 3.2 mm (1/8").

Table 5.2: Welding parameters for PTAW experiments.

Test Number	**I (A)**	**Powder Feed Rate (g/min)**	**Travel Speed (mm/min)**	**Water Flowrate (L/min)**
1	150	63	250	2.0
2	150	63	250	5.0

The chemistry of the CCO chosen has a Cr:C ratio of 7.64. Compared to the alloys utilized in the study by Wang *et al.* [90], the alloy used in this study represents a chemistry between alloy 2 and alloy 3 designed by Wang *et al.*and is representative of industrially produced CCOs.

5.3 Results

The results of the variation of cooling rate are shown in Table 5.3. There is a large decrease in the average primary carbide size as the flowrate (i.e. the cooling rate) is increased, which corroborates the link between cooling rate and carbide size. Based on the measured average primary carbide size around the samples, the null hypothesis "the thickness of the primary carbides at each cooling rate belong to the same populations" can be rejected with a 99% confidence ($p=1.0\times10^{-7}$). The analysis of the average primary carbide size (diameter) was carried out by averaging the average primary carbide size from ten areas across the sample's cross sectional surface. The pattern of measurement for the samples is illustrated in Figure 5.5. The dilution was found to be $\ll$1% for the 2 L/min water flowrate and <5% for the 5 L/min water flowrate. The small region on the left hand side of the 2 L/min water flowrate cross-section has a significant number of unmelted powders due to a powder feeding issue. As there is a distinct boundary between the area with unmelted powders and the rest of the overlay, there should be very little effect on overlay composition from this isolated portion.

Table 5.3: Average primary carbide rod diameter results for the welding trials as well as the time to cool from 800^{o}C to 500^{o}C ($t_{8/5}$).

Test Number	**Average Primary Carbide Diameter** (μm)	**Water Flowrate** (L/min)	$\mathbf{t_{8/5}}$ (s)
1	44.92±3.84	2.0	21
2	30.89±1.82	5.0	12

Example microstructural images from the samples at each of the cooling rates along with the processed versions used for measuring carbide size are presented in Figure 5.6. The processing software is the same as used by Barnes *et al.* [41] and isolates the carbides from the matrix by a series of steps. First the images are flattened into a grayscale format,

Figure 5.5: Placement of microstructural analysis for carbide size measurement across the cross-sectional surface of the overlays shown by white dashed rectangles. Left: Water flowrate of 2 L/min. Right: Water flowrate of 5 L/min.

wherein a sub-range of pixels is selected and the rest are discarded. A Gaussian blur operation is used to blend any artifacts in the image which then undergoes opening and erosion operations that ensure that the eutectic is distinct from the primary phase. Area thresholding is then used to remove the eutectic, and each carbide is assigned a distinct colour as a check to ensure the opening and erosion operations functioned correctly. The area of the carbides in pixels is then outputted in a histogram with a recorded average area. The shape of the carbide cross-section was assumed to be hexagonal and the carbide diameter was calculated from the average area. The images shown in Figure 5.6 represent one of ten areas analysed for each of the cooling rates. It is important to note that only carbide rods approximately aligned perpendicular to the cross-sectioning plane were considered for diameter calculation.

For CCOs the solidification range is approximately from 1350^{o}C to 1250^o and the cooling rate within this range is that of interest for primary carbide solidification. Due to the fluidity of the weld pool and the intensity of the welding arc, the temperature gradient from the thermal camera in the solidification range was invalidated. The measurement of cooling rate in this study has been quantified by the $t_{8/5}$ ($CR_{8/5}$) . The $t_{8/5}$ was selected as a representative range as it is an important welding value and all variables are identical

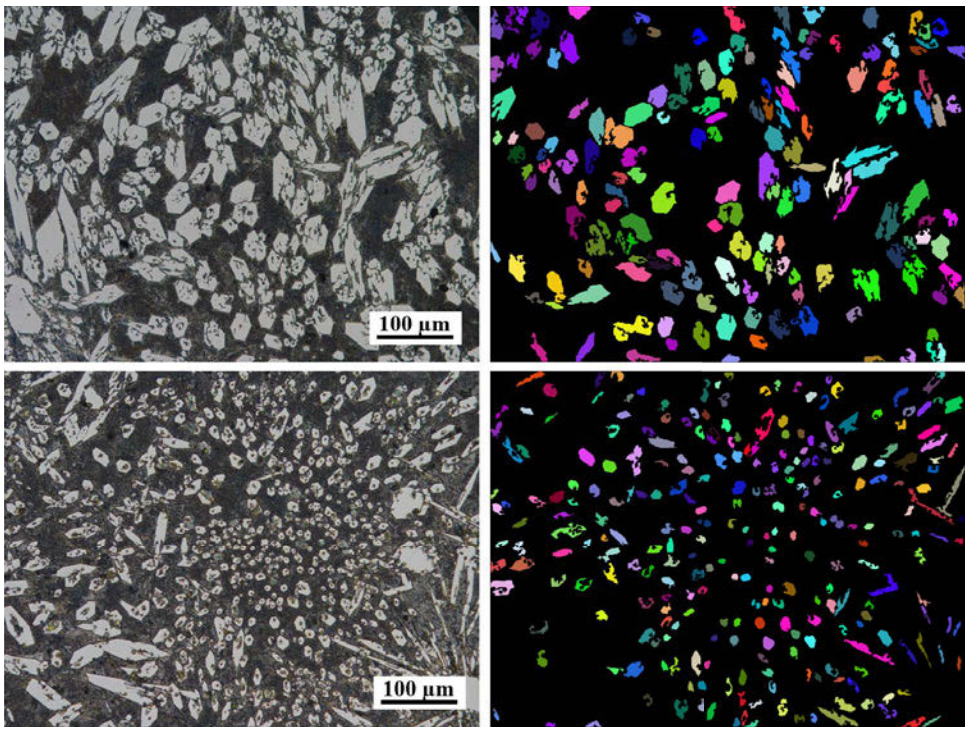

Figure 5.6: Microstructural images of overlay cross-sections. Top Left: Optical microscope image of low cooling rate (2.0 L/min flowrate) weld. Top Right: Processed image of low cooling rate weld isolating primary carbide needles oriented perpendicularly to the sectioning plane for carbide size measurement. Bottom Left: Optical microscope image of high cooling rate (5.0 L/min flowrate) weld. Bottom Right: Processed image of high cooling rate weld for carbide size measurement.

outside of the water flowrate through the substrate. Assuming a fast moving heat source on a thin plate, the cooling rate during the solidification range (CR_s) could be estimated by:

$$\frac{CR_s}{CR_{8/5}} \approx \left(\frac{T_m - T_0}{T_{t_{8/5}} - T_0} \right)^3 \tag{5.1}$$

where T_m is the melting temperature of the alloy, T_0 is the preheat temperature, and $T_{t_{8/5}}$ is the approximate temperature of the $t_{8/5}$ measurement($\sim$750°C).

The $t_{8/5}$ for each of the flowrates was determined by applying a line scan to the thermal camera videos once they had reached steady state. Images from the videos are shown in Figure 5.7 and show the steady state temperature profile. The inlet and outlet thermocouples of the substrate confirmed that steady state had been achieved. By measuring the temperature profile across a line scan placed at the approximate longitudinal centreline of the bead, the $t_{8/5}$ was determined.

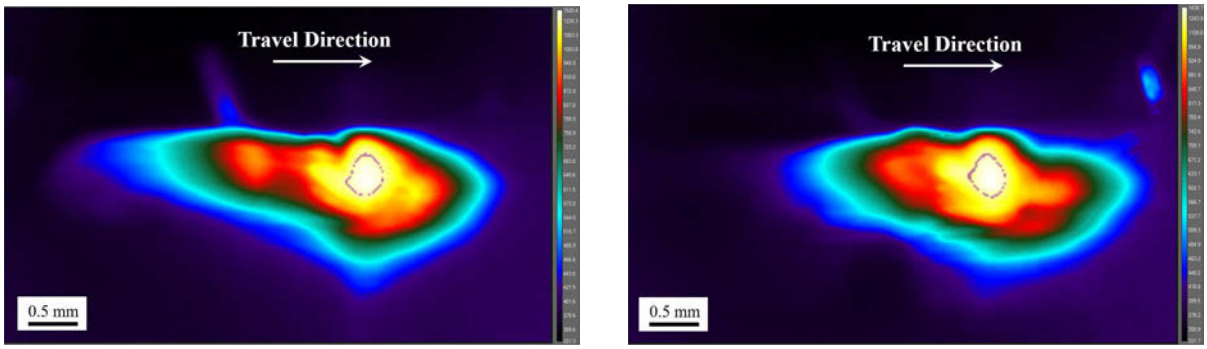

Figure 5.7: Images from thermal camera videos during the steady state portion of the experiments taken at the same camera position and the same magnification. Left: Water flowrate of 2.0 L/min. Right: Water flowrate of 5.0 L/min.

A relationship was observed between the liquidus temperature (determined by composition) and the primary carbide size based on the results presented by Wang *et al.* [90] and Borle [45]. In both studies, the composition of the samples is varied and there was an observed variation in the primary carbide diameter associated to specific compositions. In the study of Wang *et al.*the composition was directly varied between Alloy 1-4 and in

the study by Borle, the composition varied through altering levels of dilution with polarity. The resulting relationship between carbide size and liquidus temperature (calculated in Thermo-Calc [51]) is shown in Figure 5.8. The results from the in-situ visualization experiments of Barnes *et al.* [81] are also shown on the plot. The composition of the samples from Wang *et al.*is assumed to be given from the pure Fe-Cr-C ternary and the composition of the samples from Borle is assumed to be given by accounting for the centreline dilution of the CCO.

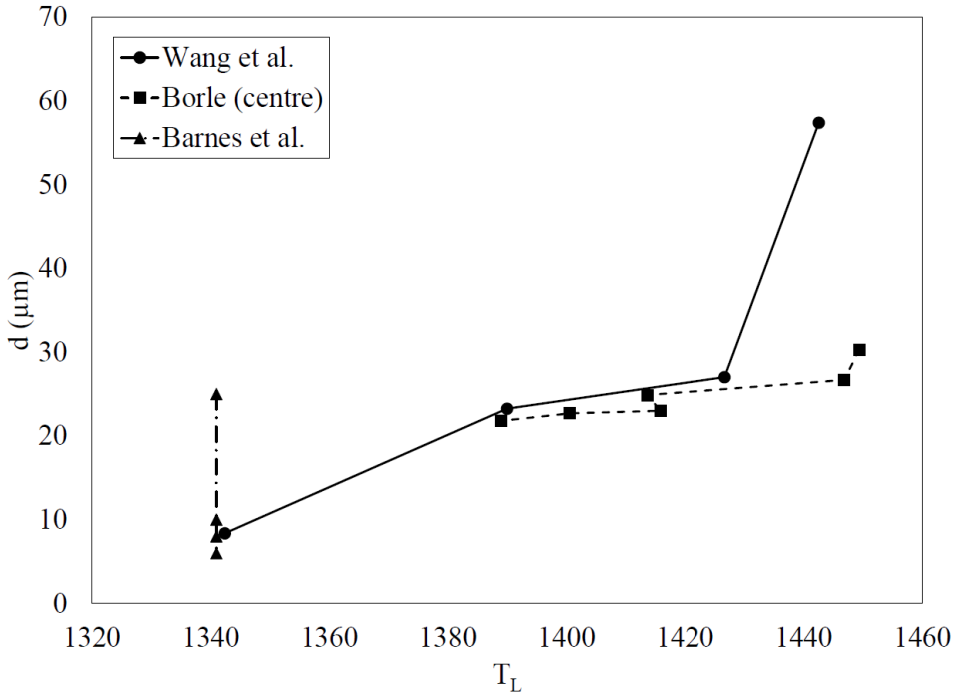

Figure 5.8: Plot illustrating the primary carbide diameter measured from the work of Wang *et al.* [90], Borle [45], and Barnes *et al.* [81] against the liquidus temperature predicted by Thermo-Calc [51].

5.4 Discussion

The results of the study show primary carbide thickness refinement with increased cooling rates. The quantitative evidence presented here represents a conclusive study building on

the hypothesis shown by the qualitative study by Wang *et al.* [90]. Applying the image analysis software to the microstructural images of the water cooled tests for alloy 2 and 3 presented in the study of Wang *et al.*and comparing the results to those in this work, it can be seen that the primary carbides presented in both works are on a similar size scale (41.24 μm for alloy 2 and 23.56 μm for alloy 3). This indicates that the cooling rate is similar between the tests and additionally implies that composition has a large effect on primary carbide size, which is hypothesized by Wang *et al.*and corroborated by the results presented in Figure 5.8.

Analysis of the thermal camera images at steady state shows the temperature profile is clearly altered by the varied flowrate of water. Paired with the results of this study, $t_{8/5}$ effectively represents the large differences in the cooling rate with flowrate.

The volume fraction of primary carbides of both cooling rates was measured at five random areas spread out across the cross section of the welds by taking a pixel count of the primary carbides as compared to the total pixels of the microstructural image. The average volume fractions of the high cooling rate and low cooling rate samples were found to be 27.52±0.33% and 25.82±0.47% respectively. The volume fractions are not statistically the same, but are close enough to suggest that the composition of both samples is not a factor in the primary carbide morphology in this case. It is important to note that unlike the size measurements, all carbides were considered, not just those aligned perpendicular to the cross-sectioning plane.

It has been hypothesized that the cooling rate of the material can alter the orientation [90] of the hexagonal primary carbide rods. It is preferable to have the carbide rods aligned perpendicularly to the direction of wear [26] as the prism faces of the rod are susceptible to fracture under impact. Impacts resulting in fractures along the long axis of the carbide could result in complete loss of carbides. For the experiments described in this study, no evidence of directional solidification parallel to the temperature gradient

was observed. Experiments involving remelting of CCO plates using laser beam welding showed that directional cooling of primary carbides is possible at high cooling rates. The high cooling rates necessary to produce directional cooling would likely result in high volume fraction of unmelted carbides and would be undesirable [77].

Based on the growth model developed by Barnes *et al.* [81] describing the growth of primary M_7C_3 carbide needles, an implication of cooling rate affecting the carbide width is that the carbide thickness alters the longitudinal growth velocity of the advancing carbide needle. The model predicts more rapid growth velocities for thinner carbides, as the same amount of solute is available for growth. The observation of a relationship between the liquidus temperature (composition) and the primary carbide thickness in combination with the observed negligible thickening of the carbides during solidification [81] implies that carbide thickness is given following nucleation and the very initial portion of growth. For the study presented in this work, the increased cooling rate would increase the undercooling and thereby depress the liquidus temperature which corroborates this hypothesis. The combination of the diffusion-controlled growth model and understanding the role of cooing rate allows for prediction of general carbide morphology.

5.5 Conclusions

Analysis on the effect of cooling rate on primary M_7C_3 carbide needles was completed systematically for the first time through the use of a cooled substrate, thermal camera imaging, optical microscopy, and image analysis software for size analysis. This work represents the first time that the effect of cooling rate on the M_7C_3 carbide needles is measured with a quantitative analysis of the primary carbide size and volume fraction. Based on the results of this study, the primary carbide size decreases with increased cooling rates.

5.6 Acknowledgements

The authors would like to thank Samuel Wilkinson Steel, a division of Samuel, Son & Co., for providing funding, samples, and their technical expertise. This research was also funded in part by NSERC (CRDPJ 470231-14) and the AWS Foundation (UA2203790).

5.7 Appendix A

The substrate was initially designed for a copper substrate to allow for welds where dilution would be completely eliminated. The thickness of the substrate was determined as the maximum to overcome the large contact resistance associated with initiating an arc on a copper substrate [92]. Heat conduction through a plane wall has the form of

$$q" = k\frac{\Delta T}{\Delta x} \tag{5.2}$$

where Δx is the plate thickness, $q"$ is the heat flux, k is the thermal conductivity (W/mK), and the temperature gradient across the plate is ΔT. The temperature gradient across the plane wall can be estimated by

$$\Delta T = T_{Cu,b} - T_{deposit} \tag{5.3}$$

where $T_{Cu,b}$ here is the temperature at the base of the plate and $T_{deposit}$ is the temperature at the top of the plate and base of the overlay. The temperature at the base of the deposit was chosen as 1100^{o}C, which is above the melting point of copper (1084^{o}C). The temperature at the base of the copper plate was chosen as the lowest temperature of the water flowing underneath the plate, which was 20^{o}C. These temperature choices allowed for an estimation of the plate thickness at the maximum temperature gradient.

Based on the thermal properties of copper [93] and the chosen temperature values, the maximum plate thickness of 4.33 mm was determined by:

$$\Delta x = k\,\frac{T_{Cu,b} - T_{deposit}}{q"} \tag{5.4}$$

The design relies on the constant flow of water in direct contact with the base of the

copper plate to ensure that the heat conducted through the thickness of the copper plate. To prevent the boiling transformation from occurring in the cooling water, a maximum temperature of the water was fixed at 50^{o}C. Using an initial ambient water temperature of 20^{o}C, the flow rate of the water can be described by

$$\begin{aligned} \dot{q} = \dot{m}\, C_p\, (T_{out} - T_{in}) &= \eta\, I\, V \\ [Heat\ into\ Water] &= [Heat\ from\ PTAW] \\ \dot{m} &= \frac{\eta\ I\ V}{C_p\ \Delta T} \end{aligned} \tag{5.5}$$

where $\dot{m}$ is the mass flowrate, C_p is the heat capacity of the water, ΔT is the temperature increase in the water, I is the welding current, V is the welding voltage, and η is the process efficiency of PTAW. The calculated water flowrate of 0.0209 kg/s is equivalent to 1.25 L/min.

The next step in the design was to determine the depth of the depression into the polymer base given for water flow. The depth of the (D_f) can be described by

$$\begin{aligned} V_w &= \frac{20\,\mu\, x_{fd,h}}{\rho\, D_f^2} = \frac{\dot{m}}{D\, W\, \rho} \\ D_f &= \frac{20\,\mu\, x_{fd,h}\, W}{\dot{m}} \end{aligned} \tag{5.6}$$

where μ is the viscosity of the water, W is the width of the channel, ρ is the density of the water, and $x_{fd,h}$ is the hydrodynamic entry length (assumed to be 25.4 mm as the minimum distance from the point of water entry that welding would occur). D_f was found to be approximately 1 mm from Equation 5.6.

The assumption of an entry length value was verified by the value of the ratio [93]

described by

$$10 \lesssim \left(\frac{x_{fd,h}}{D}\right)_{turb} \lesssim 60 \tag{5.7}$$

The bounds shown for this ratio are the boundaries of the fully developed turbulent flow region. The calculated value for th ratio was ∼28. The main objective was to maintain a fully developed flow across the welding region, which is achieved.

To ensure that the heat from welding will not penetrate through the water and into the polymer base causing melting, the amount of heat penetration must be calculated. The heat penetration into the water can be represented by

$$\begin{aligned} L &= 2\sqrt{\alpha\, t} \\ t &= \frac{d_{arc}}{V_w} \\ \alpha &= \frac{k}{\rho\, C_p} \\ V_w &= \frac{\dot{m}}{D\, W\, \rho} \\ L &= \sqrt{\frac{k\, d_{arc}}{\rho\, C_p\, V_w}} \end{aligned} \tag{5.8}$$

where d_{arc} is the diameter of the arc, α is the thermal diffusivity of the water, L is the heat penetration distance, and C_p is the specific heat capacity of the water. The calculated heat penetration distance, $L = 9 \times 10^{-5}$ m, was much less than necessary condition for fully developed flow, $D \approx 1$ mm, and therefore the heat will not affect the polymer.

Chapter 6

Conclusions and Future Work

6.1 Conclusions

For the first time, a growth model quantifying the diffusion-controlled lengthening of primary M_7C_3 carbides during solidification of CCOs in proposed. The model predicts a rapid initial transient period of growth followed by steady state growth. When compared to in-situ visualization experiments completed on a high temperature confocal microscope, the model was found to match closely to experiment for all carbides whose growth was tracked. The model predicts diffusion-controlled growth along the longitudinal axis of the faceted primary carbide needles and slow interface-controlled transverse thickening along the prism faces of the hexagonal prism shaped needles. The mode of growth observed is consistent with that recent models [57] showing a carbide shell morphology. The model analyses the carbide tip as a mass point sink in the melt and focuses solely on the diffusion of chromium as carbon, the other main alloying element, has a far higher diffusivity and is therefore not rate limiting. The mass flux along the outer prism faces (270.3 kg/m^2s) was found to be negligible ($\sim$2 orders of magnitude) compared to the flux onto the cross-section of the needle and justifies the constant carbide thickness assumed in the growth model. Due to the nature of the in-situ experiments, only carbides at the surface were analysed and therefore a half-space assumption was made as well as an assumption

to neglect the initial stages of carbide growth, as nothing can be inferred accurately from the experiments below the surface of the melt regarding nucleation and the very initial stages of growth. Research into the nucleation occurring in CCOs is outside the scope of this project and the subject of future research. The growth of primary carbides was observed to stall when the diffusion field of the carbide tip impinged on other carbides solidifying in the melt. This observation is consistent with a diffusion growth mechanism in which growth stalls as the diffusion field is depleted of solute by a another carbide.

An analysis of the effect of cooling rate on the microstructure of CCOs through the use of a thermal control substrate has yielded strong preliminary evidence that there is a strong correlation between the cooling rate and the primary carbide size. The role of cooling rate on the microstructure of CCOs was previously unclear. The cooling rate in the thermal control substrate was altered by varying the water flowrate through the system. By testing at the maximum and minimum flowrates of the substrate with identical heat input, it was shown that increasing cooling rate decreases the primary carbide cross-sectional radius. A thermal camera was employed in addition to inlet and outlet thermocouples in th waterlines to ensure that the cooling rate was being altered. The ability to control carbide size through cooling rate in conjunction with the growth model gives the ability to design carbide morphology based on process parameters during welding while maintaining a constant composition. An additional conclusion from the study of cooling rate, was that there was a observed link between the liquidus temperature of the alloy (given by composition) and the thickness of the primary carbides, indicating that the carbide radius (thickness) is likely given upon nucleation and the initial stages of growth. This conclusion aligns with the negligible thickening of the primary carbide needles, as well as the increased cooling rate decreasing the carbide radius, as increasing the cooling rate would increase the undercooling and depress the liquidus temperature.

The morphology of primary M_7C_3 carbides was analysed through 3D reconstruction

of CCO microstructure using serial sectioning, detailed etching, and a specially designed image analysis software. This software is capable of reconstructing the individual 2D layers into a 3D model and was created specifically to enable isolation of the primary carbides form the surrounding eutectic matrix. The primary M_7C_3 carbides were shown to be long needle-shaped hexagonal prismatic rods that appear as different morphologies based on the sectioning plane, settling a long standing debate in literature.

An investigation into large anomalous features observed in the microstructure of CCOs revealed the features to be unmelted powder granules. The investigation consisted of micro-hardness testing, AES analysis, EDX analysis, and EBSD analysis. EBSD characterization of the unmelted powder granules showed that they are a distinct composition of the same orthorhombic M_7C_3 phase as the primary carbides. The relevance of the presence of unmelted powder granules, described as large anomalous features, is that they contain high concentrations of Cr and C which are necessary to form primary carbides. It has been shown that increasing the cooling rate (lower the heat input) of CCOs can lead to lower dilution and therefore maintain the chemistry of the weld by decreasing the mixing with the low carbon steel base material. A consequence of lowering the heat input is that there is an increased volume fraction of unmelted powder granules which decreases the volume fraction of primary carbides. A careful balance must be maintained between decreasing the heat input and having a low volume fraction of unmelted powder granules to achieve the best wear properties.

The investigation of various features of CCOs, the development of a novel growth model to describe the diffusion-controlled longitudinal growth of primary M_7C_3 carbides, and the analysis of the effect of cooling rate on CCO microstructure all serve to improve understanding regarding the solidification and microstructure of CCOs. Improved understanding enables tailoring of specific properties of CCOs such as primary carbide size and distribution and allows for overlay optimization.

6.2 Future Work

To extend the work presented here, the following aspects of future work are proposed:

- Perform additional in-situ visualization experiments and Find faceted carbide needles exhibiting similar features to primary M_7C_3 carbides to test the versatility of the proposed growth model.
- Combine proposed carbide needle growth model with quantitative effect of cooling rate analysis to predict carbide morphology.
- Extend conclusions drawn from this work to establish a nucleation mechanism for the primary carbides.

Bibliography

[1] WTIA Welding Technology Institute of Australia. The Industry Guide to Hardfacing for the Control of Wear.

[2] NRC. A Strategy for Tribology in Canada: Enhancing Reliability and Efficiency Through the Reduction of Wear and Friction. Technical report, National Research Council of Canada Associate Committee on Tribology (Wear Friction and Lubrication), 1987.

[3] Patricio F. Mendez, Nairn Barnes, Kurtis Bell, Steven D. Borle, Satya S. Gajapathi, Stuart D. Guest, Hossein Izadi, Ata Kamyabi Gol, and Gentry Wood. Welding processes for wear resistant overlays. *Journal of Manufacturing Processes*, 16(1):4–25, 2014.

[4] Doug Schindel. Personal Communication -Weldco Companies, 2015.

[5] S. Borle. *Microstrcutural Characterization of Chromium Carbide Overlays and a Study of Alternative Welding Processes for Industrial Wear Applications*. Master of science, University of Alberta, 2014.

[6] G. Azimi and M. Shamanian. Effects of silicon content on the microstructure and corrosion behavior of Fe-Cr-C hardfacing alloys. *Journal of Alloys and Compounds*, 505(2):598–603, 2010.

[7] Chia Ming Chang, Yen Chun Chen, and Weite Wu. Microstructural and abrasive characteristics of high carbon Fe-Cr-C hardfacing alloy. *Tribology International*, 43(5-6):929–934, 2010.

[8] B. Hinckley, K. F. Dolman, R. Wuhrer, W. Yeung, and a. Ray. Sem investigation of heat treated high-chromium cast irons. *Materials Forum*, 32:55–71, 2007.

[9] B G Mellor. *Surface Coatings for Protection against Wear*. Woodhead Publishing (Maney Publishing), 2006.

[10] Madeleine Durand-Charre. The basic phase diagrams. *The microstructure of steels and cast iron*, pages 47–89, 2004.

[11] J.T.H. Pearce. Structure and wear performance of abrasion resistant chromium white cast irons. *American Foundry Society Transaction*, pages 599–622, 1984.

[12] Amilton Schon, Claudio Geraldo and Sinatora. Simulation of solidification paths in high chromium white cast irons for wear applications. *Calphad*, 22(4):437–448, 1999.

[13] Graham L.F. Powell, Ian H. Brown, and Grant D. Nelson. Tough Hypereutectic High Chromium White Iron – A Double In Situ Fibrous Composite. *Advanced Materials Research*, 32:111–114, 2008.

[14] D.R.F. West and N. Suanders. *Ternary Phase Diagrams in Materials Science*. Maney, London, 3rd edition, 2002.

[15] Chi Ming Lin, Hsuan Han Lai, Jui Chao Kuo, and Weite Wu. Effect of carbon content on solidification behaviors and morphological characteristics of the constituent phases in Cr-Fe-C alloys. *Materials Characterization*, 62(12):1124–1133, 2011.

[16] Ö. N. Doğan, J. a. Hawk, and G. Laird. Solidification structure and abrasion resistance of high chromium white irons. *Metallurgical and Materials Transactions A*, 28(6):1315–1328, 1997.

[17] Marc Lassus, Raymond Riviere, and Gilbert Monnier. Sur la structure et l'evolution des parametres cristallins de la solution solide (Cr, Fe)7C3. *Comptes Rendus des Seances Academie des Sciences Paris*, 264(Serie C):1057–1060, 1967.

[18] Robert Fruchart and Alain Rouault. Sur L'Existence de Macles dans les Carbures Orthorhombiques Isomorphes Cr7C3, Mn7C3, Fe7C3. *Annales des Chimies*, 3(4):143–145, 1969.

[19] E. Bauer-Grosse, J P Morniroli, M Khachfi, M Gantois, T. Lundstrom, and A Courtois. Crystallography of M7C3 carbides and M7B3 borides: The difference in the local order in carbides and borides to explain the nature and density of defects in these compounds. *Journal of the Less-Common Metals*, 117:231–236, 1986.

[20] C. M. Fang, M. a. van Huis, and H. W. Zandbergen. Structural, electronic, and magnetic properties of iron carbide Fe7C3 phases from first-principles theory. *Physical Review B*, 80(22):1–9, 2009.

[21] Bartek Kaplan, Andreas Blomqvist, Cecilia Århammar, Malin Selleby, and Susanne Norgren. Structural Determination of (Cr,Co)7C3. *18th Plansee Seminar, 3 – 7 June, 2013 in Reutte, Austria*, 3:HM104/1–HM104/12, 2013.

[22] S. Atamert and H.K.D.H. Bhadeshia. Microstructure and stability of Fe-Cr-C hardfacing alloys. *Materials Science and Engineering: A*, 130(1):101–111, 1990.

[23] Gary Fisher, Tonya Wolfe, Matthew Yarmuch, Adrian Gerlich, and Patricio Mendez. The Use of Protective Weld Overlays in Oil Sands Mining. page 9, 2012.

[24] H. Wolfe, T.B., Henein. Predicting Homogeneity of WC-Based Metal Matrix Composites Deposited by Plasma Transferred Arc Welding. In *12th International Conference on Modeling of Casting, Welding, and Advanced Solidification Processes*, pages 585–599, 2009.

[25] International Institute of Welding. ISO/TR 13393 - Welding Consumables - Hardfacing Classification, 2009.

[26] Shouren Wang, Linghui Song, Yang Qiao, and Min Wang. Effect of Carbide Orientation on Impact-Abrasive Wear Resistance of High-Cr Iron Used in Shot Blast Machine. *Tribology Letters*, 50(3):439–448, 2013.

[27] Chia Ming Chang, Li Hsien Chen, Chi Ming Lin, Jie Hao Chen, Chih Ming Fan, and Weite Wu. Microstructure and wear characteristics of hypereutectic Fe-Cr-C cladding with various carbon contents. *Surface and Coatings Technology*, 205(2):245–250, 2010.

[28] Zheng Jun Liu, Yun Hai Su, and J.G. Sun. Effects of Shape and Distribution of M7C3 on Wear Resistance of Iron Based Composite. *Key Engineering Materials*, 373-374:560–563, 2008.

[29] G Laird, J C Rawers, and a Adams. Fractal Analysis of Carbide Morphology in High-Cr White Cast Irons. *Metallurgical Transactions A-Physical Metallurgy and Materials Science*, 23(10):2941–2945, 1992.

[30] G. L F Powell and P. G. Lloyd. A deep etching technique for the examination of the carbide of high chromium cast iron in a scanning electron microscope. *Metallography*, 14(3):271–274, 1981.

[31] Y. F. Zhou, Y. L. Yang, Y. W. Jiang, J. Yang, X. J. Ren, and Q. X. Yang. Fe-24 wt.%Cr-4.1 wt.%C hardfacing alloy: Microstructure and carbide refinement mechanisms with ceria additive. *Materials Characterization*, 72:77–86, 2012.

[32] Triten. A Guide to the Evaluation & Selection of Hardfaced Plate.

[33] W. Ludwig, a. King, P. Reischig, M. Herbig, E. M. Lauridsen, S. Schmidt, H. Proudhon, S. Forest, P. Cloetens, S. Rolland Du Roscoat, J. Y. Buffière, T. J. Marrow, and H. F. Poulsen. New opportunities for 3D materials science of polycrystalline materials at the micrometre lengthscale by combined use of X-ray diffraction and X-ray imaging. *Materials Science and Engineering A*, 524(1-2):69–76, 2009.

[34] Michael D. Uchic. Serial sectioning methods for generating 3D characterization data of grain- and precipitate-scale microstructures. *Computational Methods for Microstructure-Property Relationships*, pages 31–52, 2011.

[35] D. Kammer and P. W. Voorhees. Analysis of Complex Microstructures: Serial Sectioning and Phase-Field Simulations. *MRS Bulletin*, 33(06):603–610, 2008.

[36] J. Alkemper and P. W. Voorhees. Quantitative serial sectioning analysis. *Journal of Microscopy*, 201(3):388–394, 2001.

[37] N Chawla and V V Ganesh. Three-dimensional (3D) Microstructure Visualization and Finite Element Modeling of the Mechanical Behavior of Heterogeneous Materials. *Proceedings of the 11th Annual Conference on Fracture*, 2005.

[38] Zhu Yan and Jiang Hua. Digital Image Forensic Approach for Photoshop Gaussian Blur. *Video Engineering*, 37, 2013.

[39] John Serra. *Image Analysis and Mathematical Morphology*. Academic Press, 1983.

[40] N. Barnes, T. Joseph, and P. F. Mendez. Issues associated with welding and surfacing of large mobile mining equipment for use in oil sands applications. *Science and Technology of Welding and Joining*, 20(6):483–493, 2015.

[41] N. Barnes, S. Borle, M. Dewar, J. Andreiuk, and P. F. Mendez. 3D microstructure reconstruction of chrome carbide weld overlays. *Science and Technology of Welding and Joining*, 19(8):696–702, 2014.

[42] V. E. Buchanan, P. H. Shipway, and D. G. McCartney. Microstructure and abrasive wear behaviour of shielded metal arc welding hardfacings used in the sugarcane industry. *Wear*, 263(1-6 SPEC. ISS.):99–110, 2007.

[43] Soner Buytoz. Microstructural properties of M7C3 eutectic carbides in a Fe-Cr-C alloy. *Materials Letters*, 60(5):605–608, 2006.

[44] D J Kotecki and J S Ogborn. Abrasion Resistance of Iron-Based Hardfacing Alloys. *Welding Journal*, 74(8):S269–S278, 1995.

[45] Steven D. Borle, Ivan Le Gall, and Patricio F. Mendez. Primary Chromium Carbide Fraction Control with Variable Polarity SAW. *Welding Journal*, 94(January), 2015.

[46] Pierre Rolland, Vincent Carlino, and Ronald Vane. Improved Carbon Analysis with Evactron Plasma Cleaning. *Microscopy and Microanalysis*, 10(S02):1–4, 2004.

[47] University of Cape Town. EDX: Precision and Accuracy in EDX Analysis, 2015.

[48] C. P. Tabrett, I. R. Sare, and M. R. Ghomashchi. Microstructure-property relationships in high chromium white iron alloys. *International Materials Reviews*, 41(2):59–82, 1996.

[49] J Plessis. Neglected and Hidden Errors in the Quantification of Auger Electron Spectroscopy. *Surface and Interface Analysis*, 20(September 1992):228–232, 1993.

[50] M P Seah. Quantitative Auger Electron Spectroscopy : Modulating the Spectrometer. *Surface and Interface Analysis*, 1(3):91–93, 1979.

[51] Thermo-Calc Software AB. Thermo-Calc, 2017.

[52] Shihong Xu. JEOL JAMP 9500 F – Information for Publications, 2016.

[53] T. Ohide and G. Ohira. Solidification of high chromium alloyed cast irons. *Institute of the British Foundryman*, 76(1):7–14, 1983.

[54] J. T. H. Pearce. Examination of M7C3 carbides in high chromium cast irons using thin foil transmission electron microscopy. *Journal of Materials Science Letters*, 2(8):428–432, 1983.

[55] Vinod Kumar. Formation and morphology of M7C3 in low Cr white iron alloyed with Mn and Cu. *ASM International*, 12:14–18, 2003.

[56] Zhou Jiyang. Colour Metallography of Cast Iron - Grey Iron III. *China Foundry*, 6(4):366–374, 2009.

[57] Sha Liu, Yefei Zhou, Xiaolei Xing, Jibo Wang, Yulin Yang, and Qingxiang Yang. Agglomeration model of (Fe,Cr)7C3 carbide in hypereutectic Fe-Cr-C alloy. *Materials Letters*, 183(September):272–276, 2016.

[58] G.P. Ivantsov. No Title. *Doklady Akademii Nauk SSSR*, 58:567–569, 1947.

[59] G Horvay and J.W Cahn. Dendritic and spheroidal growth. *Acta Metallurgica*, 9(7):695–705, 1961.

[60] R. Trivedi. The Role of Interfacial Free Energy and Interface Kinetics During the Growth of Precipitate Plates and Needles. *Metallurgical Transactions*, 1:921–927, 1970.

[61] P.E.J. Rivera-Díaz-Del-Castillo and H.K.D.H. Bhadeshia. Theory for growth of needle-shaped particles in multicomponent systems. *Metallurgical and Materials Transactions A: Physical Metallurgy and Materials Science*, 33(4):1075–1081, 2002.

[62] Clarence Zener. Kinetics of the decomposition of austensite. *Trans Aime*, 167:550, 1946.

[63] Mats Hillert. The Role of Interfacial Energy during Solid State Phase Transformations. *JERNKONTORETS ANNALER*, 141(11):757–789, 1957.

[64] R. Trivedi and G.M. Pound. Growth Kinetics of Plate-Like Precipitates. *Journal of Applied Physics*, 40(11):4293–4300, 1969.

[65] J.W. Christian. *The Theory of Transformations in Metals and Alloys*. Pergamon, 2002.

[66] Mats Hillert. Diffusion and interface control of reactions in alloys. *Metallurgical Transactions A*, 6(1):5–19, 1975.

[67] M. Hillert, L. Höglund, and J. Ågren. Diffusion-controlled lengthening of Widmanstätten plates. *Acta Materialia*, 51(7):2089–2095, 2003.

[68] M. Ben Amar and Y Pomeau. Growth of Faceted Needle Crystals: Theory. *Europhysics Letters (EPL)*, 6(7):609–614, 1988.

[69] Roger West and Hasse Fredriksson. On the Mechanism of Faceted Growth. *Journal of Materials Science*, 20:1061–1068, 1985.

[70] Jean Marc Debierre, Alain Karma, Franck Celestini, and Rahma Guérin. Phase-field approach for faceted solidification. *Physical Review E - Statistical, Nonlinear, and Soft Matter Physics*, 68(4 1):416041–4160413, 2003.

[71] C Atkinson. Concentration Dependance of D in the Growth or Dissolution of Precipitates. *Acta Metallurgica*, 15:1207–1211, 1967.

[72] O.A. Esin and P.V. Gel'd. *Physical Chemistry of Pyrometallurgical Processes - Part 2 - The interactions of liquids with gases and solid phases*. Moscow, 1966.

[73] J. Crank. The mathematics of diffusion. *Oxford University Press*, page 414, 1975.

[74] H S Carslaw and J C Jaeger. *Conduction of Heat in Solids*. Oxford University Press, second edi edition, 1959.

[75] Mohsen Akbari, David Sinton, and Majid Bahrami. Moving Heat Sources in a Half Space: Effect of Source Geometry. In *Proceedings of the ASME 2009 Heat Transfer Summer Conference HT2009*, pages 1–10, San Francisco, 2009.

[76] Frank S. Ham. Theory of diffusion-limited precipitation. *Journal of Physics and Chemistry of Solids*, 6(4):335–351, 1958.

[77] Nairn Barnes, Steven Borle, and Patricio F. Mendez. Large anomalous features in the microstructure of chromium carbide weld overlays. *Science and Technology of Welding and Joining*, 1718(January):1–6, 2017.

[78] Sha Liu, Zhijie Wang, Zhijun Shi, Yefei Zhou, and Qingxiang Yang. Experiments and calculations on refining mechanism of NbC on primary M7C3 carbide in hypereutectic Fe-Cr-C alloy. *Journal of Alloys and Compounds*, 713:108–118, 2017.

[79] John W. Gibbs, Christian Schlacher, Ata Kamyabi-Gol, Peter Mayr, and Patricio F. Mendez. Cooling Curve Analysis as an Alternative to Dilatometry in Continuous Cooling Transformations. *Metallurgical and Materials Transactions A: Physical Metallurgy and Materials Science*, 46(1):148–155, 2015.

[80] Kazue Yasue, Mineo Kosaka, Mitsuo Isotani, and Yasuhiko Kondo. Thermal Diffusivity of Cast Irons. *Journal of the Japan Institute of Metals and Materials*, 42(3):225–231, 1977.

[81] Nairn Barnes. *Solidification Theory and Optimization of Chromium Carbide Overlays*. Phd thesis, University of Alberta, 2017.

[82] W. Kurz and D.J. Fisher. *Fundamentals of Solidification, Fourth revised edition*. Trans Tech Publications, 1998.

[83] B. J. Keene. Review of data for the surface tension of pure metals. *International Materials Reviews*, 38(4):157–192, 1993.

[84] Ram (McMaster University) Murarka. *Surface Tension Measurements on Iron and Iron-Oxygen Alloys*. Master of engineering, McMaster University, 1971.

[85] Lars Onsager. Theories and Problems of Liquid Diffusion. *Annals of the New York Academy of Sciences*, 46(5):241–265, 1945.

[86] H K D H Bhadeshia. Diffusional Formation of Ferrite in Iron and its Alloys. *Progress in Materials Science*, 29:321–386, 1985.

[87] H K D H Bhadeshia. Advances in the Kinetic Theory of Carbide Precipitation. *Materials Science Forum*, 426-432:35–42, 2003.

[88] W. Kurz and D. J. Fisher. Dendrite growth at the limit of stability: tip radius and spacing. *Acta Metallurgica*, 29(1):11–20, 1981.

[89] M. Alavarez-Vera, A. Hernandez-Rodriguez, M. A. L. Hernandez-Rodriguez, A. Juarez Hernandez, J. R. Benavides-Trevino, and J. H. Garcia-Duarte. Effect of Cooling Rate During Solidification on the Hard PHASES of M23C6-Type of Cast CoCrMo Alloy. *METALURGIJA*, 55(3):382–384, 2016.

[90] Z. H. Wang, Q. B. Wang, L. Cui, a. D. Yang, and D. Y. He. Influence of cooling rate and composition on orientation of primary carbides of Fe–Cr–C hardfacing alloys. *Science and Technology of Welding and Joining*, 13(7):656–662, 2008.

[91] J. Hornung, A. Zikin, K. Pichelbauer, M. Kalin, and M. Kirchgasner. Influence of cooling speed on the microstructure and wear behaviour of hypereutectic Fe-Cr-C hardfacings. *Materials Science and Engineering A*, 576:243–251, 2013.

[92] Kevin M. Scott, Satya S. Gajapathi, Julien Chapuis, and Patricio F. Mendez. Calorimetry of Droplets in Free-Flight Metal Transfer GMAW.

[93] Frank P. Incropera, David P. Dewitt, Theodore L. Bergman, and Adrienne S. Lavine. *Intorduction to Heat Transfer*. John Wiley & Sons, Inc., 2011.

[94] MathWorks. MATLAB, 2017.

Appendix A. MATLAB Code for Chapter 4

Included in this appendix are the MATLAB [94] code files used to output the comparison plots between the in-situ visualization experiments and the diffusion-controlled growth model.

7.1 Main code for plotting all experimental data and model curves for all four carbides.

```
% List all experimental data points from carbide tracking in the videos.
z_01 = [0 145.796];
z_02 = [0 360.469];
z_03 = [0 288.375];
z_04 = [0 499.662];
tz = [0 10];
zh_01 = [0 83.446];
zh_02 = [0 206.313];
zh_03 = [0 165.051];
zh_04 = [0 285.980];

```

```
12 xexp_01 = [0 8 14 24 34 40 46 51 55 63 70 70.4 75 78 80 80.4 81.4 81.4 ...
       81.8 87.8 91.8];
13 texp_01 = [0 0.13 0.27 0.46 0.93 1.32 2.05 2.45 2.71 3.37 3.9 4.1 4.96 ...
       5.89 6.95 7.48 8.34 9.59 11.58 12.11 12.44];
14 xexp_02 = [0 10 18 24 32 36 40 60 61 64 66 68 70 71 79 81 83 83];
15 texp_02 = [0 0.07 0.14 0.2 0.34 0.47 0.6 0.8 0.93 1.26 1.53 1.66 1.79 ...
       1.86 1.99 2.19 2.45 2.78];
16 xexp_03 = [0 2 6 10 12 16 18 22 24 28 36 46 50 62 68 74 82 84 85 86 87 ...
       88 88 89 89];
17 texp_03 = [0 0.07 0.14 0.2 0.27 0.34 0.4 0.47 0.53 0.6 0.67 0.8 0.87 ...
       1.06 1.13 1.26 1.33 1.39 1.46 1.79 1.99 2.19 2.32 2.72 2.85];
18 xexp_04 = [0 10 16 24 34 35 42 48 54 62 68 76 84 88 92 94 98 100 102 ...
       104 106 110 112 114 116 118 120 122 124 126 128 134 138 146 150 154 ...
       158 162 164 166 168 170 172 174 180 182 184 186];
19 texp_04 = [0 0.06 0.13 0.2 0.26 0.33 0.4 0.46 0.53 0.59 0.66 0.73 0.86 ...
       0.92 0.99 1.06 1.12 1.26 1.32 1.39 1.45 1.52 1.59 1.65 1.79 1.92 ...
       1.98 2.05 2.18 2.25 2.31 2.38 2.45 2.51 2.65 2.71 2.78 2.84 2.91 ...
       2.98 3.11 3.17 3.24 3.37 3.57 3.64 3.7 3.77];
20
21
22 % Define step size and size of for loop.
23 t = linspace(0,15,1000);
24 for i = 1:size(t,2)
25     x(i) = yfunction_5CR_01_01(t(i));
26     y(i) = yfunction_5CR_01_02(t(i));
27     z(i) = yfunction_5CR_01_03(t(i));
28     w(i) = yfunction_5CR_01_04(t(i));
29 end
30
31 % Plot Figure for carbide 5CR_01_01.
32 figure1 = figure('Color',[1 1 1]);
```

```
33 set(groot, 'defaultAxesTickLabelInterpreter','latex'); set(groot, ...
       'defaultLegendInterpreter','latex');
34 axes1 = axes('Parent',figure1,'LineWidth',1.25,'FontSize',18);
35 box(axes1,'on');
36 hold(axes1,'all');
37 h1 = plot(t,x,'color',[0.1 0.1 0.1],'linewidth',2);
38 hold on
39 h5 = plot(texp_01,xexp_01,'-k.','color',[0.1 0.1 ...
       0.1],'linewidth',1.5,'MarkerSize',16);
40 hold on
41 plot(4.1,70.4,'kx','MarkerSize',18,'linewidth',2);
42 hold on
43 h9 = plot(tz,z_01,'--k','color',[0.1 0.1 0.1],'linewidth',2);
44 hold on
45 h10 = plot(tz,zh_01,':k','color',[0.1 0.1 0.1],'linewidth',2);
46 set(gcf, 'Units', 'Inches', 'Position', [0, 0, 8, 6], 'PaperUnits', ...
       'Inches', 'PaperSize', [7.25, 9.125])
47 xlabel('\bf{t (s)}','FontSize',18,'Interpreter', ...
       'latex','FontWeight','bold')
48 ylabel('\bf{x} (\boldmath$\mu$\bf{m})','FontSize',18,'Interpreter', ...
       'latex')
49 legend([h1 h5 h9 h10],'Model 5CR\_01\_01','Observation ...
       5CR\_01\_01','Zener 5CR\_01\_01','Zener-Hillert 5CR\_01\_01')
50 set(legend,'Interpreter', 'latex','FontSize',14)
51 axis([0 8 0 200]);
52 ax = gca;
53 outerpos = ax.OuterPosition;
54 ti = ax.TightInset;
55 left = outerpos(1) + ti(1);
56 bottom = outerpos(2) + ti(2);
57 ax_width = outerpos(3) - ti(1) - ti(3);
```

```
ax_height = outerpos(4) - ti(2) - ti(4);
ax.Position = [left bottom ax_width ax_height];
p = pbaspect;
pos = get(gca,'Position');
ax1=axes('position',pos,'visible','off');
axis([0 1 0 p(2)]); axis('equal'); axis('manual'); hold on;
darr([0.3 0.5],[0.38 0.26],'k',0.02,0.02); hold on;
text(0.22,0.4,'\bf{Impingement}','Interpreter','latex','FontSize',16);

% Plot Figure for carbide 5CR_01_02.
figure2 = figure('Color',[1 1 1]);
set(groot, 'defaultAxesTickLabelInterpreter','latex'); set(groot, ...
    'defaultLegendInterpreter','latex');
axes1 = axes('Parent',figure2,'LineWidth',1.25,'FontSize',18);
box(axes1,'on');
hold(axes1,'all');
h2 = plot(t,y,'color',[0.1 0.1 0.1],'linewidth',2);
hold on
h6 = plot(texp_02,xexp_02,'-k.','color',[0.1 0.1 ...
    0.1],'linewidth',1.5,'MarkerSize',16);
hold on
plot(0.73,53,'kx','MarkerSize',18,'linewidth',2)
hold on
h11 = plot(tz,z_02,'--k','color',[0.1 0.1 0.1],'linewidth',2);
hold on
h12 = plot(tz,zh_02,':k','color',[0.1 0.1 0.1],'linewidth',2);
set(gcf, 'Units', 'Inches', 'Position', [0, 0, 8, 6], 'PaperUnits', ...
    'Inches', 'PaperSize', [7.25, 9.125])
xlabel('\bf{t (s)}','FontSize',18,'Interpreter', ...
    'latex','FontWeight','bold')
```

```
84 ylabel('\bf{x} (\boldmath$\mu$\bf{m})','FontSize',18,'Interpreter', ...
       'latex')
85 legend([h2 h6 h11 h12],'Model 5CR\_01\_02','Observation ...
       5CR\_01\_02','Zener 5CR\_01\_02','Zener-Hillert 5CR\_01\_02')
86 set(legend,'Interpreter', 'latex','FontSize',14)
87 axis([0 8 0 200]);
88 ax = gca;
89 outerpos = ax.OuterPosition;
90 ti = ax.TightInset;
91 left = outerpos(1) + ti(1);
92 bottom = outerpos(2) + ti(2);
93 ax_width = outerpos(3) - ti(1) - ti(3);
94 ax_height = outerpos(4) - ti(2) - ti(4);
95 ax.Position = [left bottom ax_width ax_height];
96 p = pbaspect;
97 pos = get(gca,'Position');
98 ax1=axes('position',pos,'visible','off');
99 axis([0 1 0 p(2)]); axis('equal'); axis('manual'); hold on;
100 darr([0.48 0.105],[0.15 0.19],'k',0.02,0.02); hold on;
101 text(0.5,0.15,'\bf{Impingement}','Interpreter','latex','FontSize',16);
102
103
104 % Plot Figure for carbide 5CR_01_03.
105 figure3 = figure('Color',[1 1 1]);
106 set(groot, 'defaultAxesTickLabelInterpreter','latex'); set(groot, ...
       'defaultLegendInterpreter','latex');
107 axes1 = axes('Parent',figure3,'LineWidth',1.25,'FontSize',18);
108 box(axes1,'on');
109 hold(axes1,'all');
110 h3 = plot(t,z,'color',[0.1 0.1 0.1],'linewidth',2);
111 hold on
```

```
112 h7 = plot(texp_03,xexp_03,'-k.','color',[0.1 0.1 ...
        0.1],'linewidth',1.5,'MarkerSize',16);
113 hold on
114 plot(1.39,84,'kx','MarkerSize',18,'linewidth',2)
115 hold on
116 h13 = plot(tz,z_03,'--k','color',[0.1 0.1 0.1],'linewidth',2);
117 hold on
118 h14 = plot(tz,zh_03,':k','color',[0.1 0.1 0.1],'linewidth',2);
119 set(gcf, 'Units', 'Inches', 'Position', [0, 0, 8, 6], 'PaperUnits', ...
        'Inches', 'PaperSize', [7.25, 9.125])
120 xlabel('\bf{t (s)}','FontSize',18,'Interpreter', ...
        'latex','FontWeight','bold')
121 ylabel('\bf{x} (\boldmath$\mu$\bf{m})','FontSize',18,'Interpreter', ...
        'latex')
122 legend([h3 h7 h13 h14],'Model 5CR\_01\_03','Observation ...
        5CR\_01\_03','Zener 5CR\_01\_03','Zener-Hillert 5CR\_01\_03')
123 set(legend,'Interpreter', 'latex','FontSize',14)
124 axis([0 8 0 200]);
125 ax = gca;
126 outerpos = ax.OuterPosition;
127 ti = ax.TightInset;
128 left = outerpos(1) + ti(1);
129 bottom = outerpos(2) + ti(2);
130 ax_width = outerpos(3) - ti(1) - ti(3);
131 ax_height = outerpos(4) - ti(2) - ti(4);
132 ax.Position = [left bottom ax_width ax_height];
133 p = pbaspect;
134 pos = get(gca,'Position');
135 ax1=axes('position',pos,'visible','off');
136 axis([0 1 0 p(2)]); axis('equal'); axis('manual'); hold on;
137 darr([0.2 0.175],[0.58 0.32],'k',0.02,0.02); hold on;
```

```
138 text(0.12,0.6,'\bf{Impingement}','Interpreter','latex','FontSize',16);
139
140 % Plot Figure for carbide 5CR_01_04.
141 figure4 = figure('Color',[1 1 1]);
142 set(groot, 'defaultAxesTickLabelInterpreter','latex'); set(groot, ...
        'defaultLegendInterpreter','latex');
143 axes1 = axes('Parent',figure4,'LineWidth',1.25,'FontSize',18);
144 box(axes1,'on');
145 hold(axes1,'all');
146 h4 = plot(t,w,'color',[0.1 0.1 0.1],'linewidth',2);
147 hold on
148 h8 = plot(texp_04,xexp_04,'-k.','color',[0.1 0.1 ...
        0.1],'linewidth',1.5,'MarkerSize',16);
149 hold on
150 plot(1.06,94,'kx','MarkerSize',18,'linewidth',2)
151 hold on
152 h15 = plot(tz,z_04,'--k','color',[0.1 0.1 0.1],'linewidth',2);
153 hold on
154 h16 = plot(tz,zh_04,':k','color',[0.1 0.1 0.1],'linewidth',2);
155 set(gcf, 'Units', 'Inches', 'Position', [0, 0, 8, 6], 'PaperUnits', ...
        'Inches', 'PaperSize', [7.25, 9.125])
156 xlabel('\bf{t (s)}','FontSize',18,'Interpreter', ...
        'latex','FontWeight','bold')
157 ylabel('\bf{x} (\boldmath$\mu$\bf{m})','FontSize',18,'Interpreter', ...
        'latex')
158 legend([h4 h8 h15 h16],'Model 5CR\_01\_04','Observation ...
        5CR\_01\_04','Zener 5CR\_01\_04','Zener-Hillert 5CR\_01\_04')
159 set(legend,'Interpreter', 'latex','FontSize',14)
160 axis([0 8 0 200]);
161 ax = gca;
162 outerpos = ax.OuterPosition;
```

```
ti = ax.TightInset;
left = outerpos(1) + ti(1);
bottom = outerpos(2) + ti(2);
ax_width = outerpos(3) - ti(1) - ti(3);
ax_height = outerpos(4) - ti(2) - ti(4);
ax.Position = [left bottom ax_width ax_height];
p = pbaspect;
pos = get(gca,'Position');
ax1=axes('position',pos,'visible','off');
axis([0 1 0 p(2)]); axis('equal'); axis('manual'); hold on;
darr([0.59 0.15],[0.2 0.34],'k',0.02,0.02); hold on;
text(0.6,0.2,'\bf{Impingement}','Interpreter','latex','FontSize',16);

% Save figures to file.
print(figure1,'xvst5CR_01_01.jpg','-djpeg','-r1000');
print(figure2,'xvst5CR_01_02.jpg','-djpeg','-r1000');
print(figure3,'xvst5CR_01_03.jpg','-djpeg','-r1000');
print(figure4,'xvst5CR_01_04.jpg','-djpeg','-r1000');

end
```

7.2 Root code for carbide 5CR_01_01

```
function y = yfunction_5CR_01_01(t)

% Define all variables.
Do = 1.85e-07;
Q = 60500;
ro = 1.25e-05;
```

```
% ri = 0.3e-05;
% A = pi*((ro^2)-(ri^2));
R = 8.314;
fcrinft = 0.267;
fcre = 0.222;
fcrs = 0.578;
ffes = 0.314;
ffee = 0.709;
T0 = 1225.88;
TC = T0 - (t*5);
TK = TC + 273.15;
D = Do*exp(-Q./(R*TK));
Di = Do*exp(-Q/(R*(T0+273.15)));
const1 = (2.*D)./(ro);
const2 = (6900/6600)*(fcrinft - fcre);
const3 = (fcrs - (ffes/ffee)*fcre);

% Calculate initial time boundary condition.
t0 = (ro^2)/Di;

% Define velocity.
U = @(t) ...
    1e06.*(const1.*const2.*(1./const3).*(1./(erfc(ro./sqrt(4.*D.*(t+t0))))));

$Calculate velocity.
y = quad(U,0,t);

end
```

7.3 Root code for carbide 5CR_01_02

```
function y = yfunction_5CR_01_01(t)

% Define all variables.
Do = 1.85e-07;
Q = 60500;
ro = 1.25e-05;
% ri = 0.3e-05;
% A = pi*((ro^2)-(ri^2));
R = 8.314;
fcrinft = 0.267;
fcre = 0.222;
fcrs = 0.578;
ffes = 0.314;
ffee = 0.709;
T0 = 1156.72;
TC = T0 - (t*5);
TK = TC + 273.15;
D = Do*exp(-Q./(R*TK));
Di = Do*exp(-Q/(R*(T0+273.15)));
const1 = (2.*D)./(ro);
const2 = (6900/6600)*(fcrinft - fcre);
const3 = (fcrs - (ffes/ffee)*fcre);

% Calculate initial time boundary condition.
t0 = (ro^2)/Di;

% Define velocity.
U = @(t) ...
    1e06.*(const1.*const2.*(1./const3).*(1./(erfc(ro./sqrt(4.*D.*(t+t0))))));

$Calculate velocity.
```

```
y = quad(U,0,t);

end
```

7.4 Root code for carbide 5CR_01_03

```
function y = yfunction_5CR_01_03(t)

% Define all variables.
Do = 1.85e-07;
Q = 60500;
ro = 0.5e-05;
% ri = 0.3e-05;
% A = pi*((ro^2)-(ri^2));
R = 8.314;
fcrinft = 0.267;
fcre = 0.222;
fcrs = 0.578;
ffes = 0.314;
ffee = 0.709;
T0 = 1156.72;
TC = T0 - (t*5);
TK = TC + 273.15;
D = Do*exp(-Q./(R*TK));
Di = Do*exp(-Q/(R*(T0+273.15)));
const1 = (2.*Di)./(ro);
const2 = (6900/6600)*(fcrinft - fcre);
const3 = (fcrs - (ffes/ffee)*fcre);

```

```
% Calculate initial time boundary condition.
t0 = (ro^2)/Di;

% Define velocity.
U = @(t) ...
    1e06.*(const1.*const2.*(1./const3).*(1./(erfc(ro./sqrt(4.*D.*(t+t0))))));

$Calculate velocity.
y = quad(U,0,t);


end
```

7.5 Root code for carbide 5CR_01_04

```
function y = yfunction_5CR_01_04(t)

% Define all variables.
Do = 1.85e-07;
Q = 60500;
ro = 0.3e-05;
% ri = 0.3e-05;
% A = pi*((ro^2)-(ri^2));
R = 8.314;
fcrinft = 0.267;
fcre = 0.222;
fcrs = 0.578;
ffes = 0.314;
ffee = 0.709;
```

```
15 T0 = 1167.74;
16 TC = T0 - (t*5);
17 TK = TC + 273.15;
18 D = Do*exp(-Q./(R*TK));
19 Di = Do*exp(-Q/(R*(T0+273.15)));
20 const1 = (2.*Di)./(ro);
21 const2 = (6900/6600)*(fcrinft - fcre);
22 const3 = (fcrs - (ffes/ffee)*fcre);
23
24 % Calculate initial time boundary condition.
25 t0 = (ro^2)/Di;
26
27 % Define velocity.
28 U = @(t) ...
       1e06.*(const1.*const2.*(1./const3).*(1./(erfc(ro./sqrt(4.*D.*(t+t0))))));
29
30 $Calculate velocity.
31 y = quad(U,0,t);
32
33 end
```

Appendix B. Thermo-Calc Code for Chapter 4

Included in this appendix is the Thermo-Calc [51] code file used to output the Scheil solidification prediction of the CCO alloy tested in the in-situ visualization experiments detailed in Chapter 4.

8.1 Thermo-Calc Code for Scheil Solidification

```
go scheil
1
tcfe6
fe
y
cr
26.7
c
3.41
mn
2.39
```

```
mo
0.8
b
0.24
p
0.02
si
0.53

1500
 *
fcc liq cem m7c3

y
n
1
y

D:\Scheil_ICP_nofd y
y
6
y
9
0.4

D:\Scheil_ICP_nofd.ps
```

```
y
D:\Scheil_ICP_nofd.txt
y
t
w(*,*)
n
y
6
yes
9
0.4

Scheilcomp_ICP_nofd
y
Scheilcomp_ICP_nofd.txt
y
t
ns(cem)
n
y
6
yes
9
0.4

Scheil_ICP_nofd_mf(cem)
```

```
y
Scheil_ICP_nofd_mf(cem).txt
y
t
ns(m7c3)
n
y
6
yes
9
0.4

Scheil_ICP_nofd_mf(m7c3)
y
Scheil_ICP_nofd_mf(m7c3).txt
y
t
ns(fcc)
n
y
6
yes
9
0.4

Scheil_ICP_nofd_mf(fcc)
```

```
y
Scheil_ICP_nofd_mf(fcc).txt
y
t
nv(cem)
n
y
6
yes
9
0.4

Scheil_ICP_nofd_mv(cem)
y
Scheil_ICP_nofd_mv(cem).txt
y
t
nv(m7c3)
n
y
6
yes
9
0.4

Scheil_ICP_nofd_mv(m7c3)
```

```
y
Scheil_ICP_nofd_mv(m7c3).txt
y
t
nv(fcc)
n
y
6
yes
9
0.4

Scheil_ICP_nofd_mv(fcc)
y
Scheil_ICP_nofd_mv(fcc).txt
n
exit
```